Ion Intercalation in Layered MoO_3 and WO_3 Nanostructure

Hu Zhibin

NATIONAL UNIVERSITY OF SINGAPORE

2013

Ion Intercalation in Layered MoO_3 and WO_3 Nanostructure

Hu Zhibin

(B. Sc.)

A THESIS SUBMITTED

FOR THE DEGREE OF DOCTOR OF PHILOSOPHY IN SCIENCE

DEPARTMENT OF PHYSICS

NATIONAL UNIVERSITY OF SINGAPORE

2013

DECLARATION

I hereby declare that this thesis is my original work and it has been written by me in its entirety. I have duly acknowledged all the sources of information which have been used in the thesis.

This thesis has also not been submitted for any degree in any university previously.

Hu Zhibin April. 23. 2013

Hu Zhibin

23 April 2013

Acknowledgements

I would like to express my sincere gratitude to my supervisor *Assoc. Prof. Sow Chorng Haur*. I am greatly indebted to his inspirational motivation, selfless guidance and immense support during the course of my Ph.D. I am extremely thankful to him for providing thoughtful suggestions and continuous hard work on papers.

I would like to thank *Assoc. Prof. Cheng Hansong* for his guidance and support. I am grateful to him for providing theoretical calculations which are important to my project. I would like to thank *Assoc. Prof. Tok Eng Soon* for helping with theory explanation of photoelectrical response effect.

I would like to express my sincere thanks to *Dr. Varghese Binni, Dr. Lim Zhihan, Dr. Hoi Siew Kit, Dr. Wei Dacheng, Dr. Zhou Chenggang* for successful collaboration.

I owe a deep sense of gratitude to all my group members *Zheng Minrui, Mukherjee Bablu, Yun Tao, Tamang Rajesh, Lim Xiaodai Sharon, Lu Junpeng, Ramanujam Prabhakar Rajiv* for their support and I would also like to thank *Wang Yinhui, Ji Zhuang* for their collaboration. I would like to thank *Ms. Foo Eng Tin* for assisting with lab suppliers as well.

I acknowledge National University of Singapore (NUS) for research scholarship.

I feel a deep sense of gratitude to my parent for their inspiration and affection shown to me. I am equally thankful to my fiancée *Tang Wei* for her understanding and tolerance and for her simple presence by my side.

Table of Contents

Summary

MoO_3 and WO_3 have been widely studied for their broad applications in many industry fields, including photochromic devices, electrochromic devices, ion batteries, gas sensors and catalysts. The properties of these two materials can be significantly improved by either intercalation or nano-configuration. It is thus reasonable to intercalate ions into nanostructured MoO_3 and WO_3 to achieve better properties for the two materials. However, existing methods, which combine intercalation and nano-configuration, have various limitations, such as structure deformation upon ion intercalation, multi-step process and ion size limitation.

This dissertation describes a simple one-step method to synthesize MoO_3 and WO_3 single crystalline nanostructure with a great amount of K ion intercalation. These two materials (K_xMoO_3, K_xWO_3 nanobundles) are fabricated by thermal evaporation on mica substrate. Despite the large amount of K ion intercalated (K:Mo/W>0.2), the layered and orthorhombic structure of MoO_3 and pseudo-orthorhombic structure of WO_3 are preserved. The method is simple and straightforward. It utilizes the open ended furnace only and is carried out in ambient and moderate temperature. The simpleness makes the method repeatable in other environment.

Upon significant amount of ion insertion, many new properties are observed in MoO_3 and WO_3 nanostructures, including high conductivity, photoelectrical response and electromigration behaviour. Firstly, the electronic conductivity of MoO_3 or WO_3 is enhanced by 7 orders in the case of MoO_3 and 5 orders in the case of WO_3 after ion insertion. The magnitude is also three orders higher than that of the lithiated MoO_3 bulk and five orders higher than that of lithiated MoO_3 nanobelt. The conductivity is further increased hundreds of times, when the material is heated from room temperature to 200 degree. Secondly, high photon induced voltage (36.5 mV) or photon induced current (9 nA) is produced in single nanobundle under laser irradiation at low laser

power (2.2 mW) without external bias voltage. Remarkably, the amplitude and polarity of the voltage can be controlled by the location of focused laser spot. Finally, due to the large current density and the preserved layered structure, when an electric current is applied to a K_xMoO_3 nanobundle, the K ions migrate readily and rapidly in the flowing direction of electrons within the nanobundle.

The simple preparation method provides a new direction to insert great amount of large ions into nanostructured materials without changing the structure of the materials. The charge transferred from inserted ions results in extremely high conductivity, modifies the band structure of the material, and induces photon-electron response. Moreover, the high current density, the single crystalline structure and the great amount of inserted ions will bring many unexpected phenomena into semiconductor nanostructures, such as electromigration behaviour. It is noted that K_xMoO_3 nanobundle and K_xWO_3 nanobundle are quite different with other materials which has the similar stoichiometry (such as potassium molybdenum bronze). Our materials are quite new and not reported before. Besides the excellent properties described in the thesis, lots of properties are not systematically studied. Future work are required to explore the materials and get further insight about the synthesis method.

List of Publications

1. **Zhibin Hu**, B Rajini Kanth, Rajesh Tamang, Binni Varghese, Chorng-Haur Sow and P K Mukhopadhyay, Visible microactuation of a ferromagnetic shape memory alloy by focused laser beam, *Smart Mater. Struct.* **21**, 032003 (2012).

2. **Zhibin Hu**, Chenggang Zhou, Minrui Zheng, Junpeng Lu, Binni Varghese, Hansong Cheng and Chorng-Haur Sow, K-enriched MoO_3 nanobundles: a layered structure with high electric conductivity, *J. phys. Chem. C*, 116, 3962-2967 (2012).

3. **Zhibin Hu**, Zhuan Ji, Wilson Weicheng Lim, Bablu Mukherjee, Chenggang Zhou, Eng Soon Tok and Chorng-Haur Sow, K-enriched WO_3 Nanobundles: High Electric Conductivity and Significant Photocurrent with Controlled Polarity, *ACS Appl. Mater. Interfaces,* 5, 4731–4738 (2013).

4. **Zhibin Hu**, Eng Soon Tok and Chorng Haur Sow, Localized Photon Induced Voltage with Controlled Polarity in Single K Enriched MoO_3 Nanobundle *Nanotechnology*, 23, 475204 (2012)

5. **Zhibin Hu**, Chenggang Zhou, Rajiv Ramanujam Prabhakar, Sharon Xiaodai Lim, Yinghui Wang, Jeroen A. van Kan, Hansong Cheng, Subodh G. Mhaisalkar, Chorng-Haur Sow, Rapid Reversible Electromigration of Intercalated K Ions within Individual MoO_3 Nanobundle, *J. Appl. Phys.* 113, 024311 (2013)

6. Bablu Mukherjee, **Zhibin Hu**, Minrui Zheng, Yongqing Cai, Yuan Ping Feng, Eng Soon Tok, and Chorng Haur Sow, Stepped-surfaced $GeSe_2$ Nanobelts with High-gain Photoconductivity, *J. Mater. Chem.* 22, 24882 (2012)

7. Siew-Kit Hoi, **Zhibin Hu** , Yuan-Jun Yan, Chorng-Haur Sow and Andrew A. Bettiol A microfluidic device with integrated optics for microparticle switching, *Appl. Phys. Lett.* **97**, 183501 (2010)

8. Dacheng Wei, Lanfei Xie, Kian Keat Lee, **Zhibin Hu**, Wei Chen, Chorng Haur Sow, Yunqi Liu, Hongjie Dai, Andrew Thye Shen Wee, Controllable unzipping for Intramolecular Junctions of Graphene Nanoribbons and Single Walled Carbon Nanotubes, *Nature Communications* 4, 1374 (2013)

List of Tables

List of Figures

List of Symbols

e	Electronic charge
λ	Wavelength
V	Voltage
σ	Conductivity
μ	Carrier mobility
n	Carrier density
T	Absolute temperature
K	Boltzmann constant
I	Current
C	Capacitance
ε	Dielectric constant
D	Diffusion coefficient
τ	Life time of charge carrier
L	Charge carrier diffusion length

Chapter 1 Introduction

1.1 Wide applications of MoO_3 and WO_3

In daily life, transition metal oxides are widely used, such as natural magnets (Fe_3O_4), pigments in all colors used in plastics, glass, ink, ceramics, paints and coating (CuO, Ti-Ni-O, ZnO), sunscreen and UV light absorber in cosmetics and skin care products (TiO_2). With such a great variety of applications, transition metal oxides constitute one of the most interesting classes of solids[1]. Transition metal oxides are materials containing transition metals and oxygen, while transition metals are metallic elements that serve as a transition between two sides in periodic table as shown in Figure 1.1. Among these transition metal oxides, MoO_3 and WO_3 have been widely studied due to their interesting layered structures. Because of their unique structures and properties, MoO_3 and WO_3 have a wide range of applications in many different industry fields, including photochromic devices[2], electrochromic devices[3], ion batteries[4] , gas sensors[5] and catalysts[6].

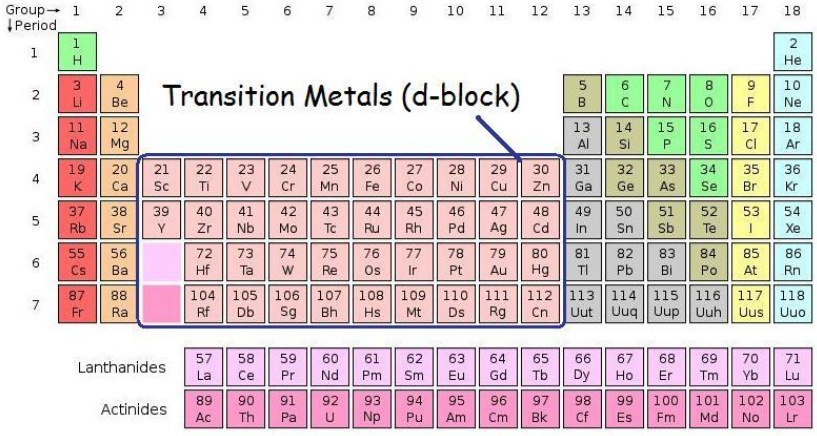

Figure 1.1 Periodic Table with blue rectangle denoting the transition metals.[7]

MoO_3 and WO_3 have a variety of structures including orthorhombic structure, monoclinic structure, hexagonal structure and tetragonal structure. Among these various MoO_3 and WO_3 structures, orthorhombic MoO_3 and monoclinic WO_3 are two of the most common structures in MoO_3 and WO_3 family. Both materials are built up by MoO_6/WO_6 octahedra. Each octahedra (Figure 1.2(a)) contains a central Mo/W atom surrounded by six oxygen atoms with almost the same distance from the central atom. In the orthorhombic MoO_3 structure, corner-sharing MoO_6 octahedra are linked as a chain, and two similar chains are connected together by edge-sharing to form layers of MoO_3 (Figure 1.2(b))[2]. These layers are stacked in a staggered configuration and held together by weak van de Waal´s forces. In the monoclinic WO_3 structure, infinite array of corner-sharing WO_6 octahedra forms a layer of WO_3, and these layers are stacked in arrangement and held together by weak van de Waal´s forces (Figure 1.2(c)).[8]

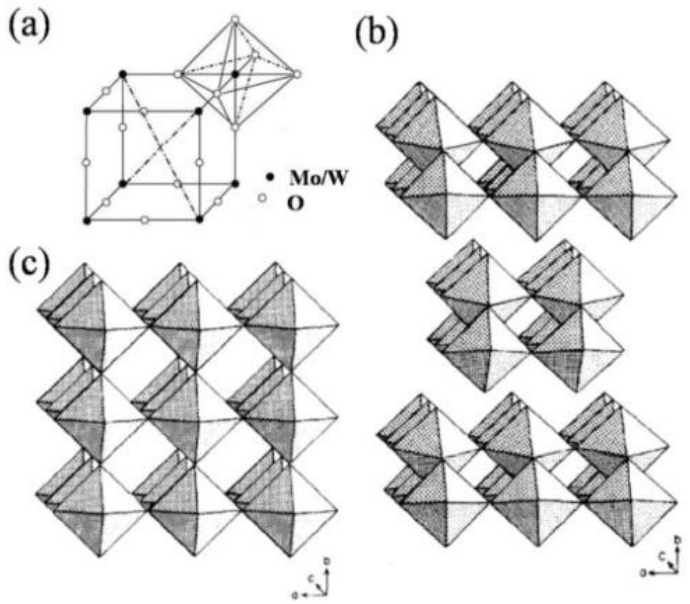

Figure 1.2 (a) unit cell of MoO_6/WO_6 octahedra (b) structure of orthorhombic MoO_3 (c) structure of monoclinic WO_3.

In both structures, tunnels (continuous vacancies) are formed between layers in which small ions could stay or move in the event of the presence of an exterior force. The ability to accommodate ion insertion in this kind of structure makes it an excellent candidate to be applied in photochromic devices, electrochromic devices

and ion batteries. Moreover, both materials are easily reduced, a property which enables it to be applied as catalyst. Besides, the MoO_3 and WO_3 are n-type semiconductors, the electric property of which is sensitive to the exposed environment, making them good candidates for gas sensors.[5] The detailed behaviours and mechanisms of these applications will be discussed below.

Application 1: Photochromic devices

Photochromism is the reversible transformation of a species between two forms with different colors upon the absorption of photo radiation. The reversible photochromism effect is observed in the MoO_3 films. Specifically, the films are almost transparent in the visible region which turns blue under UV-light irradiation. The colored film can be bleached by electrochemical polarization, and be colored again by UV irradiation.[2, 9] In particular, the change of colors corresponds to the difference in light absorption. The transparent MoO_3 films exhibit strong absorption of light with wavelength below 400 nm, and the absorption arises from electron excitation from valence band to conduction band. For the colored film, significant absorption appears in the visible light range with the maximum absorption wavelength between 780 nm and 900 nm, which results from a superposition of electron excitation to many discrete bands.[10]

Many theoretical models try to explain the photochromism effect, including color center model, double insertion/extraction of ions and electrons model and small polaron model[2]. Double insertion/extraction of ions and electrons model is mostly accepted. The model indicates that when irradiated with UV light, electrons and holes are formed in MoO_3 film, while holes react with adsorbed water (the prepared film always contain water on the surface or inside the structure) to generate protons (H^+).[2, 10] These protons diffuse into the MoO_3 lattice and react with photon generated electrons and MoO_3 to form hydrogen molybdenum bronze (H_xMoO_3). In the bronze, part of Mo atoms are reduced to Mo^{5+}, and due to the injected photon energy from

light, intervalence charge transfer occurs from the newly formed Mo^{5+} to adjacent Mo^{6+} . The absorption of light in certain wavelength makes the film turn blue.

The photon induced color change phenomenon has made MoO_3 and WO_3 as promising candidates for many technological applications, such as large scale display, erasable optical storage media, radiation intensity controller, self-developing photography and so on.[2]

Application 2: Electrochromism

The electrochromic effect describes the reversible transformation of a material between two forms with different colors upon electrochemical ion intercalation[3]. The WO_3 thin film is transparent, which turns blue upon ion insertion and electron insertion. The colored film can be bleached by ion extraction and colored again by ion insertion, illustrating the reversible and reproducible electrochromism effect.

In the simplified model,[3, 11] upon ion and electron insertion diffused from electrolyte, the following reaction takes place

$$WO_3 + xM^+ + xe^- \leftrightarrow M_xWO_3$$

with M^+ = H^+, Li^+, Na^+ or K^+ . In tungsten bronze M_xWO_3, part of W^{6+} ions are reduced to W^{5+}. The inserted electrons are localized in these W^{5+} sites and polarize their surrounding lattice to form small polarons. These small polarons absorb the energy from incident photons and hop from one site to another, as in

$$h\nu + W^{5+}(A) + W^{6+}(B) \rightarrow W^{6+}(A) + W^{5+}(B)$$

where hν is the energy of absorbed photon energy and polaron hops from A to B. Due to absorption of photons with certain wavelength, the film turns to dark blue.

The electrochromic effect has rendered MoO_3 and WO_3 as promising candidates for many technological applications[12] such as “smart” window,[13, 14] Electrochromic photonic crystals[15] and Electrochromic imaging[16].

Application 3: Ion battery

Lithium-ion batteries are quite popular these days. In lithium ion battery, the positive electrode is mostly made of Lithium cobalt oxide, contributing Li ions. The negative electrode is made of materials with layered structure, where Li ions could be inserted and extracted. When the battery charges, Li^+ moves through the electrolyte from the positive electrode to the negative electrode and inserts between layers in electrode. During discharge, the lithium ions move back to the $LiCoO_2$ from the cathode.[4, 17]

As described above, in MoO_3 and WO_3, continuous vacancies are formed between layers in which small ions could stay or move in the presence of exterior force. For the ability of reversible incorporation of Li ions into MoO_3 or WO_3 layered structure, they are used as the cathodes in lithium batteries.[4, 18]

Application 4: Gas sensor

A reducing molecule (e.g., CO, H_2) adsorbed on the sensor surface injects electrons into it. While oxidizing gases like NO, extract electrons from sensor surface. Consequently, in the case of n-type semiconductors, the resistance of the sensor decreases when contacts with reducing gas due to high electron population, while the resistance increases when contacts with an oxidizing gas.[5] The changed resistance upon appearance of gases contributes to the sensitivity of MoO_3 and WO_3 to these gases.

Nitrogen oxides, NO and NO_2, produced from combustion facilities and automobiles are main pollutants which damage human respiratory organs and nerves. WO_3 have outstanding sensitive properties toward NO_x at low and elevated temperature. Tong *et al.*[19] reported that WO_3 thin film sensors exhibit high sensitivity to NO_2, and the lowest detection concentration of NO_2 is 1 ppm. Meanwhile, the sensitivity to 10 ppm NO_2 gas is five times larger than the response to 500 ppm CO,

H_2S, CH_4 gases. Compared with other materials, the low cross sensitivity makes WO_3 better candidate for detection of these two gases.

Ammonia is a reducing agent for nitrogen oxides converting them into nitrogen and water vapor. An ammonia sensor is required to selectively detect small quantities of ammonia fed into the inlet stream in the presence of interfering gases such as NO_x, CO and hydrocarbons.[20] MoO_3 is sensitive to NH_3 and NO_2 gases in the temperature range from 200 to 450 ^oC, particularly the lowest detection concentration of NH_3 is 3 ppm. No cross sensitivity was recorded for other gaseous species.[20, 21] The particular selectivity makes MoO_3 a better candidate for NH_3 based integrated sensors.

Application 5: Catalyst

One quarter of all organic products produced worldwide are synthesized via selective partial oxidation. MoO_3 is widely used in selective partial oxidation process on the fact that it is easily being reduced.[6, 22] In the process, alkenes are absorbed to the (100) surface of MoO_3 on coordinatively unsaturated Mo sites under the formation of an allylic intermediate, and a bond between the lattice oxygen and the allylic intermediate forms on the (010) surface. The attached oxygen is then inserted into the hydrocarbon to give the oxygenated product, leaving an oxygen vacancy at the catalyst surfaces.[6] The MoO_3 surface oxygen defects could be replenished by surface oxygen diffusion in the same layer or other layers. Thus, the alkenes could continuously be partially oxidized.

1.2 Intercalation induced new properties and intercalation method

As described above, in the layered structure of MoO_3 and WO_3, tunnels form between layers, where ions can move in by exterior force. Such ion insertion process between layers is called intercalation. Intercalating ions into MoO_3 and WO_3 boosts

their applications as photochromic devices, electrochromic devices and ion batteries. In addition, intercalating ions into the structure of MoO_3 and WO_3 improves the performance of these devices, such as displaying higher coloration efficiency, faster response, stronger absorption, higher stability and so on.

Photochromic devices: Yao *et al.*[23] reported that upon Li intercalation into MoO_3, the sample showed a new photosensitive response in the region between 500 and 800 nm, while the pure MoO_3 was sensitive only to the UV light (wavelength below 400 nm). This is attributed to the fact that upon Li^+ incorporation, the shortest Mo–Mo separation distance increases and results in the formation of a new energy state. Therefore, electrons can be excited into a new state after irradiation with visible light, and then to the conduction band of molybdenum oxide. The process reduces Mo^{6+} to Mo^{5+}, resulting in the formation of blue-colored molybdenum bronze.

Electrochromic device: Zhang *et al.*[24] reported that Li intercalation into MoO_3 film dramatically improved the electrochemical reversibility of the film. In the Li-doped MoO_3 films, some degradation was observed between the third and the tenth cycle but a pronounced improvement in durability was achieved. In contrast, pure MoO_3 film showed significant irreversible insertion in the first cycle with subsequent degradation in the second cycle.

Batteries: Leroux *et al.*[25] reported that upon sodium (Na) intercalation, MoO_3 film exhibited high specific capacity of 940 mA/g in the voltage window of 3.0~0.005V, and the charge capacity efficiency (the ratio of the charge capacity at n^{th} circle over the value at first circle) was 88% after the 20^{th} cycle and 75% at the 50^{th} cycle, while in pure MoO_3, the capacity at first cycle was around 700 mA/g and the capacity efficiency decreased to 67% at the 10^{th} cycle. The comparison indicates that upon Na intercalation, higher charge capacity and more stable charge capacity retention is achieved.

Gas sensor: Wang *et al.*[19] intercalated Polyaniline (PANI, a kind of polymer) into the MoO_3 layered structure. The resulting $(PANI)_xMoO_3$ thin film displayed an increase in electrical resistivity in response to volatile organic compounds. The intercalated film was especially sensitive to formaldehyde and acetaldehyde, while pure MoO_3 was not sensitive to either of the gases. These two volatile gases are poisonous to humans. Formaldehyde is highly toxic to all animals, regardless of method of intake. Ingestion of as little as 30 mL of a solution containing 37% formaldehyde has been reported to cause death in an adult human. Acetaldehyde, air pollutant resulting from combustion like automotive exhaust and tobacco smoke, is toxic when applied externally for prolonged periods, which possibly induce cancer.

Besides the reports mentioned above, many species could be intercalated, thus improving the performance of MoO_3. These species include ions like H^+, Li^+, Na^+, K^+, Rb^+, Cs^+, Ce^{3+}[26] and many kinds of polymers like PANI, SP, pyridines[27]. There are many methods to intercalate these species into MoO_3/WO_3 structure. These methods could be divided into two groups, electrochemical method and self diffusion method.

Electrochemical method: Spahr *et al.*[28] and Sian *et al.*[29] carried out insertion experiments in galvanostatic mode using a standard three-electrode arrangement, in which the working and counter electrodes were soaked with an electrolyte solution. Poly-MoO_3 films were used as a working electrode, platinum strip as a counter electrode, Ag/AgCl as a reference electrode, and an appropriate quantity of $HClO_4$, $LiClO_4$, $NaClO_4$, $KClO_4$, $Mg(ClO_4)_2$ dissolved in propylene carbonate (PC) as electrolyte solution for insertion of H^+, Li^+, Na^+, K^+ and Mg^{2+} ions separately. Driven by external electric field, these ions were intercalated between MoO_3 layers.

Self diffusion method: Tagaya *et al.*[27] intercalated organic compound into MoO_3 by two steps. Firstly, MoO_3 was suspended in an aqueous solution of Na_2SO_4 to form Na_xMoO_3. Then, the solvent was decanted and the residual solid was treated with an

ethanolic solution containing guest organic compound. Zhang *et al.*[30] dissolved metallic molybdenum powder in H_2O_2 solution and then added $LiOH \cdot H_2O$. By drying the solution at 40℃ in an oven, Li-doped MoO_3 xerogel powder can be produced. Mahajan *et al.*[31] fused niobium pentoxide (Nb_2O_5) powder with potassium pyrosulphate ($K_2S_2O_7$) in silica crucible. The solution was dissolved in tartaric acid and mixed with MoO_3 powder dissolved ammonia solution. The final solution was pneumatically pulverized on the glass, and the Nb-doped MoO_3 film was achieved after spraying. During these processes, compounds were intercalated by self diffusion method driven by concentration gradient force.

It is noted that these methods are applied to MoO_3 films or powders, and these materials turn into an amorphous structure after a great amount of ion intercalation or large size ion intercalation.

1.3 Nanostructure induced new properties and nanomaterial synthesis method

The materials in nano-scale are widely studied these days and they exhibit various advantages, such as the high surface to volume ratio of the nanostructures provides large contact surface areas for reaction, the short diffusion path in the crystalline structure improves ion reaction efficiency, and the high flexibility and adequate toughness accommodate strains induced by ion insertion, etc. The performance of MoO_3 and WO_3 in all application fields are greatly enhanced when both materials in nano-scale are utilized.

Electrochromic device: The diffusion coefficient and the length of diffusion path determine the electrochromic efficiency. The former depends on the crystal structure, and the latter is determined by the material's microstructure.[32] With same crystal structure, the materials in nanoscale display short diffusion length for its small size

and thus exhibit excellent electrochromic efficiency. Se-Hee Lee *et al.*[33] reported that by fabricating Electrochromic films from crystalline WO_3 nanoparticles, the cycling stability and electrochromic efficiency of EC device were dramatically increased. In nanoparticle films, the current response increases slightly during the course of 3000 cycles without a significant change in the shape of the CVs, while the amorphousWO_3 film degrades significantly after only 500 cycles. It indicates the excellent cycling stability of the nanoparticle films. Moreover, the total cathodic charge for the WO_3 nanoparticles is ~32 $mCcm^{-2}mg^{-1}$, compared to ~3 $mCcm^{-2}mg^{-1}$ for crystalline films and ~9 $mCcm^{-2}mg^{-1}$ for amorphous films. The high charge insertion density over the same time period indicates great electrochromic efficiency of the nanoparticle films.

Batteries: There are several advantages associated with the utilization of nanomaterial as electrode for lithium batteries, including (a) better accommodation of the strain induced by Li^+ insertion/extraction, improving cycle life (b) new reactions not available with bulk materials (c) larger electrode/electrolyte contact area, leading to higher charge/discharge rates (d) short electron transport path lengths, permitting operation under low electronic conductivity or at higher power (e) short Li^+ transport path lengths, allowing operation under low Li^+ conductivity or higher power.[34] Molybdenum oxide microrods with diameters of ~2–6 μm were investigated as a cathode and compared with ball-milled MoO_3 particles.[18, 35] The microrods maintained a reversible capacity of 199 mAh/g which was 88.4% of the highest capacity, while the particle electrode exhibited a capacity of 85 mAh/g after 100 cycles corresponding to 47.2% of the initial capacity. It indicates that the nanostructures could more easily accommodate the structural strain occurred upon Li ion insertion. Liang Zhou *et al.*[36] reported that the α-MoO_3 nanobelts exhibited a high discharge capacity of 264 mAh/g at 30 mA/g and 176 mAh/g at 5000 mA/g. The capacity was still up to 114 mAh/g after 50 cycles at the high current density of 5000 mA/g, while the bulk α-MoO_3 cracked during the same process. The excellent high rate performance is related to the nanobelt morphology of the α-MoO_3 due to its short diffusion path length.

Sensor: For the large surface to volume ratio of nanomaterials, their conductivity is strongly influenced by surface reactions, which significantly improves their sensitivity to gases.[37] E. Comini *et al.*[38] reported that on the response to CO, MoO_3 nanorods showed the response to 30 ppm of CO was more than 100% while the thin film showed the response of 30% only. Moreover, the pure single crystalline of nanorod guaranteed long term stability of the sensor, which was not always satisfied in bulk due to grain coalescence.

Large scale synthesis of MoO_3 and WO_3 nanostructure is achievable using various techniques ranging from direct thermal heating of foil in a furnace, hot wire chemical vapour deposition, hydrothermal, sol-gel methods, and etc. Chu *et al.*[39] and Xie *et al.*[40] reported that by heating the Molybdenum foil to ~500-600°C in a tube furnace or on hot plate, the oxidized vapour nucleated and nanostructure formed on the substrate covered on or nearby the foil. Zhou *et al.*[36] synthesized MoO_3 nanobelts by hydrothermal treatment of a peroxomolybdic acid solution, which was prepared by mixing H_2O_2 aqueous solution with Mo metal powder. Dillon *et al.*[32] employed hot-wire chemical vapor deposition (HWCVD) to produce MoO_3/WO_3 nanostructure. A single W/Mo filament, was resistively heated to ~1400 °C in a static gas atmosphere consisting of Ar and O_2 gases, and the metal oxide powder collected on the walls of the quartz tube as the filament was slowly oxidized.

1.4 Challenge of intercalating large ions into nanostructure

Considering that MoO_3 and WO_3 can achieve better performance through intercalation and nano-configuration, it is reasonable to intercalate ions into nanostructure so that better properties of MoO_3 and WO_3 are obtained. However, existing methods, which combine intercalation and nano-configuration, have various limitations.

One of the methods which intercalate ions into a MoO_3 thin film is the electrochemical method. Intercalated species invariably take the interstitial positions between layers of the MoO_3 structure. With the uptake of these ions, the interlayer spacing of the MoO_3 increases. The over expansion induced from large size ion intercalation or from a great amount of small size ion intercalation destroys the layered structure of MoO_3. The phenomenon has been observed in experiments carried out by many groups. Sian *et al.*[41] reported that upon intercalation of 20% K ions (large size ion, atomic percentage ratio of K over Mo is 0.2), the layered structure of MoO_3 is destroyed due to the over expansion between layers. The structural change phenomenon is illustrated by the disappearance of (020) peak in XRD measurement after intercalation, in which the (020) peak denotes the layered structure of MoO_3. Joseph *et al.*[42] reported that upon immersing MoO_3 film into dilute (~10^{-9} M) $LiClO_4$ solution for a long time (60 min, intercalation of small ions Li^+ with a great amount), the layered structure of MoO_3 deforms step by step over the course: firstly cracks associated with the formation of Li_xMoO_3 become prominent at the (010) surface of MoO_3, then the cracks extend along other directions, and finally, the structural integrity of the (010) surface is diminished, the film disintegrates and flakes off.

In addition to the limitation of structural deformation, the electrochemical method is also constrained in the application into nano-configuration. During the process of intercalation into nanostructures by the electrochemical method, a metallic substrate is required as electrode in the electrochemical process to hold the MoO_3 nanostructures (nanobelts, nanowires, nanoparticles). Zhou *et al.*[36] pressed the powder mixture of MoO_3 nanobelts, acetylene black and PTFE into thin film, and the film was placed onto Ni grid for the electrochemical process. Meduri *et al.*[35] directly synthesized MoO_3 nanowires onto stainless steel substrate. The conducting substrates, together with as synthesized nanowires, were used as electrodes for the electrochemical process. In these processes, multi-steps are required to achieve ion

intercalation in nanostructure; moreover, structural deformation in nanostructure still exists after ion intercalation.

Self diffusion method is also a widely used method to intercalate ions into nanostructures. For small ions (such as Li^+), lithiated MoO_3 nanobelts were prepared by immersing MoO_3 nanobelts into LiCl solution[43]. However, the efforts to intercalate large ions such as K^+ into the MoO_3 nanostructure by self diffusion method has never been successful due to the large size of these ions compared to the size of the gap between layers.

Besides physical ion insertion, there are some synthesis methods to intercalate ions by chemical reaction. However, the structure of MoO_3 and WO_3 deforms greatly by these methods. Insertion of K^+ ions in the synthesis of bulk potassium molybdenum bronze ($K_{0.3}MoO_3$) by electrolytic reduction of potassium molybdate and molybdenum oxide mixtures gives rise to a substantial structural distortion. The compound becomes infinite sheets consisting of clusters of ten edge-sharing molybdenum octahedral linked by corners in the [010] and [102] directions with the adjacent sheets held together by potassium ions.[12] Zheng *et al.* synthesized potassium tungsten bronze nanowires by thermal heating potassium hydroxide solution treated tungsten foils.[44] In the compound, WO_6 octahedra are formed into a six member ring and K ion occupies the vacancy in the center of the ring.

To date, intercalating large cationic species into MoO_3/WO_3 nanostructures without giving rise to severe structural deformation of the layered orthorhombic MoO_3 structure or monoclinic WO_3 structure has remained a great technical challenge.

1.5 Research Aims

In this study, we synthesize MoO_3 and WO_3 single crystalline nanostructure with a great amount of K ion (large size ion) intercalation. These two materials are fabricated by a simple method - thermal evaporation on mica substrate. The muscovite mica acts as K source and substrate for growth. With the simple one step method, we achieve single crystalline, nano-configuration and ion intercalation and preserved crystal structure at the same time, while in other reports, a multi-step method was used or structure became deformed. Despite the large amount of K ion intercalated (atomic ratio of K over Mo/W is larger than 0.2), the layered and orthorhombic structure of MoO_3 and pseudo-orthorhombic structure of WO_3 are preserved. The simple preparation method solves the problem that large size ion intercalation deforms the structure of MoO_3 and WO_3, and thus provides a new direction to develop nano-structured materials of large-ion intercalated metal oxides.

A significant amount of ion insertion in the nanostructure induces many new properties, including in particular, high conductivity, photocurrent response and electromigration behaviour are observed in our materials. Firstly, the electronic conductivity of MoO_3 and WO_3 is enhanced several orders upon K insertion, and the value is further increased hundreds of times, when the material is heated from room temperature to 200 degree. The substantial high electric conductivity attributed to ion intercalation has not been observed in other reports. Secondly, the significant photoelectrical response of individual nanomaterial (K_xMoO_3, K_xWO_3 nanobundle) is observed. Before ion intercalation, both materials do not display such photocurrent response due to the large band gap of the materials. The comparison suggests that the method presented in the thesis provides an excellent way to introduce photoelectrical response property to the material. Finally, the rapid and reversible electromigration of intercalated K ions within a layered single crystalline K_xMoO_3 nanobundle is observed, which results from the facility of structure and high current density in the material.

The electromigration is always observed in the metal and induces cracks or piles in the material, but the phenomenon has not been observed in semiconductors before. The observation in our material opens a new route for the study of electromigration effect and provides new insight about such effect.

1.6 Outline of the thesis

The structure of the thesis will be as follows. In the Chapter one, we have introduced the properties and applications of MoO_3 and WO_3 and the enhanced performance induced by ion intercalation and nanostructure configuration. The synthesis methods to intercalate ions and to produce nanostructure are introduced as well. The challenge of intercalating large ions into nanostructure is discussed and the aim of the thesis is proposed. In Chapter two, we will introduce the experimental techniques used in the project including synthesis method, characterization techniques, individual nanostructure electrode device fabrication method and focused laser system. In Chapter three, the synthesis method to intercalate K ions into the single crystalline MoO_3 nanostructure and the characterization of the material will be discussed in detail. Chapter four introduces the electrical properties of K enriched MoO_3 nanobundle and the observation of photocurrent. In Chapter five, we look into the amazing phenomenon of electromigration of intercalated K ions between MoO_3 layers. In Chapter six, we apply similar method to successfully synthesis K enriched WO_3 nanobundle, further characterization and applications are introduced. Finally, we conclude our work and discuss the future works in Chapter seven.

Chapter 2 Experimental Techniques

In this chapter, we describe the thermal evaporation method to synthesize K ion intercalated MoO_3 and WO_3 nanostructure, and the various experimental characterization techniques utilized to identify the structure of the material. The preparation process of individual nanostructure electrode device for electrical property measurement is provided. The alignment of focused laser system for individual nanostructure photo-electrical response measurement is discussed as well.

2.1 Fabrication of Mo and W oxide nanostructures

Our group has successfully fabricated MoO_3 nanobelt and WO_3 nanowire using thermal evaporation method on glass and silicon substrate.[40] Similar thermal evaporation method is utilized to fabricate K enriched MoO_3 nanostructure. A horizontal tube furnace (Carbolite MTF 12/25/250) is used for the controlled growth of nanostructure by thermal evaporation method. The tube furnace contains a ceramic tube of diameter ~ 6 cm with both ends open in the ambient. We utilize a Mo/W foil (5 mm×5 mm×0.05 mm in size, from Aldrich Chemical Co., Inc.) as Mo/W source. The foil is polished by sand paper to remove the surface oxidized layer. Then, these foils are cleaned by sonicating in deionized water and isopropanol for 15 mins respectively, air dried in ambient and placed in the middle of ceramic boat. A muscovite mica sheet ($K_2O•3Al_2O_3•6SiO_2•2H_2O$, 8 mm×8 mm in size, from Alfa Aesar Co., Inc.) is prepared as substrate and K source. The mica sheet is placed on top of the Mo/W foil at certain height in the ceramic boat. The ceramic boat is inserted into the tube furnace and placed in the middle, the hottest region of the tube furnace. The temperature of the furnace is then raised at a rate of 30 ℃/minute. After reaching a required temperature, the system is maintained at this temperature for certain period.

After growth, the system is cooled down to room temperature in ambient. During the synthesis, air flow is controlled by fan to provide adequate oxygen continuously. The synthetic scheme described above is shown in Figure 2.1(a). Figure 2.1(b) displays a photograph of the tube furnace used to fabricate nanomaterial.

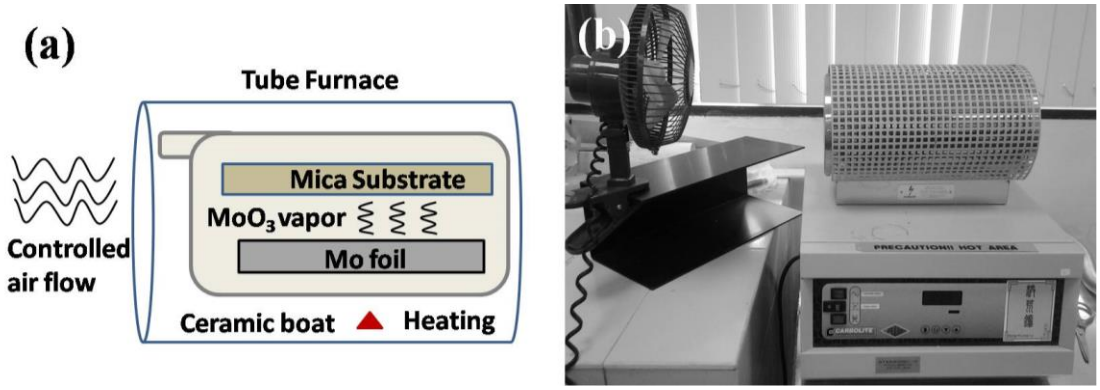

Figure 2.1 (a) Schematic representation of the synthesis system (b) Photograph of the tube furnace used to fabricate nanomaterial.

2.2 Characterization Methods and Techniques

As-synthesized products are characterized using various characterization tools. These characterization methods include morphology characterization by SEM, elemental composition and chemical state detection by EDX and XPS, lattice structure determination by TEM, XRD and Raman Spectroscopy.

Scanning Electron Microscope (SEM)

Scanning Electron Microscope (SEM) is the most widely used equipment to study surface features of materials in micro- and nano-scale. A focused electron beam scans on the samples and reacts with the surface atoms. The scattering interaction between beam electrons and surface atoms results in the ejection of secondary electrons. These secondary electrons are originated within a few nanometers from the sample, used for imaging.[45] The morphological characterization of the grown substrate and the structures created in this work is carried out using the field emission SEM JEOL JSM-6700F with the spatial resolution of ~10 nm.

Transmission Electron Microscopy (TEM)

Transmission Electron Microscopy (TEM) is the technique with advantage of large magnification range. In TEM microscopy, a low magnification image of the nanostructures and a high resolution image of the alignment of atoms can be achieved. The low resolution TEM images provide the information about the size, shape and morphology of the nanostructures. The high resolution TEM images provide information about lattice structure, crystalline quality and details of the defect structures. In TEM, images are formed by a beam of electrons transmitting through the specimen. Because the wavelength of high-energy electrons is a few thousandths of a nanometer while the spacing between atoms in the solid is hundreds times larger, the atoms act as a diffraction grating to the electrons. When electrons transmit through the sample, some of these electrons are scattered to particular angles, determined by the crystal structure of the sample. The image on the screen will be a series of spots, named **Selected Area Electron Diffraction pattern** (SAED), telling the crystal structure of the material.[46] The TEM analysis is carried out using JEOL JEM-2010F with 200 kV electron beam.

Energy-dispersive X-ray spectroscopy (EDX)

Energy-dispersive X-ray spectroscopy (EDX) is an analytical technique used for the elemental analysis. A high energy beam of electrons is focused on the sample, excites an inner shell electron in sample atoms, ejecting it from shell and creating a hole. An electron in the outer shell fills the hole, and releases the energy equalling to the difference between the higher-energy shell and the lower energy shell in the form of X-ray. The detected energy of the X-rays is characteristic of the atomic structure of the element, allowing the elemental composition of the specimen to be determined.[47] The EDX measurement system is equipped in SEM or TEM.

X-ray photoelectron spectroscopy (XPS)

X-ray photoelectron spectroscopy (XPS) is an analytical technique that measures the elemental composition and chemical state of the elements in the material. A X-ray beam is irradiated towards the material, and the top 1 to 10 nm of the sample absorb the X-ray energy, ejecting outer shell electrons. The kinetic energy of these electrons are measured and the elements in the material are determined.[48] The XPS spectrum is sensitive to the chemical environment of an atom. It enables the application of XPS in the identification of valance state of a particular element. The XPS spectrum is recorded under ultra-high vacuum condition using Omicron EA125 analyzer; monochromatic Mg Kα source (1253.6 eV), system.

X-ray Diffraction (XRD)

The regular aligned atoms in the lattice structure scatter the incident wave and result in the diffraction. The significant diffraction appears when the wavelength of the incident wave is comparable with the distance between atoms. For the wavelength of X-ray is the same order of the magnitude as the spacing between planes in the crystal, X-ray Diffraction (XRD) spectrum is utilized to reveal the information about the crystal structure of materials by detecting the scattered intensity of an X-ray beam. The X-ray beam is originated from the source, and directed onto the sample. The scattered X-ray beam is recorded by the detector as a function of incident and scattered angle. We record the XRD spectrum using Philips X'PERT MPD (Cu Kα (1.5418 Å) radiation) machine.

Raman Spectroscopy

Raman Spectroscopy characterizes the material by analysing vibrational, rotational and other low frequency modes in a sample. A focused laser beam is directed onto the sample and a spectrometer is utilized to detect the intensity of inelastic scattering of photons after photon-phonon interaction within the material. Results are recorded in terms of the difference in wavenumbers between the incident and scattered

photon, known as the Raman shift. The Raman spectra reported in this works are taken using Renishaw Ramascope 2000 system with an Olympus microscope attachment and a 514.5 nm laser used as the excitation source.

2.3 Individual Nanostructure Electrode Device Fabrication

To investigate the electrical properties of individual nanostructure, the micro-electrode device is fabricated. Individual nanostructure is transferred from the growth substrate to SiO_2/Si substrate and photolithography method is utilized to achieve designed metal (Au(400 nm)/Cr(10 nm)) finger electrodes (of gap ~15 μm) that make contact with the nanostructure. Photolithography is a process used in micro-fabrication to make patterns on the thin film. Focused laser beam is used to transfer a pattern onto a light sensitive photoresist on the substrate. A series of chemical treatments are then applied to engrave the exposure pattern and enable deposition of other materials upon the pattern. The remaining photoresist is then removed and leaving the patterned materials on the substrate.

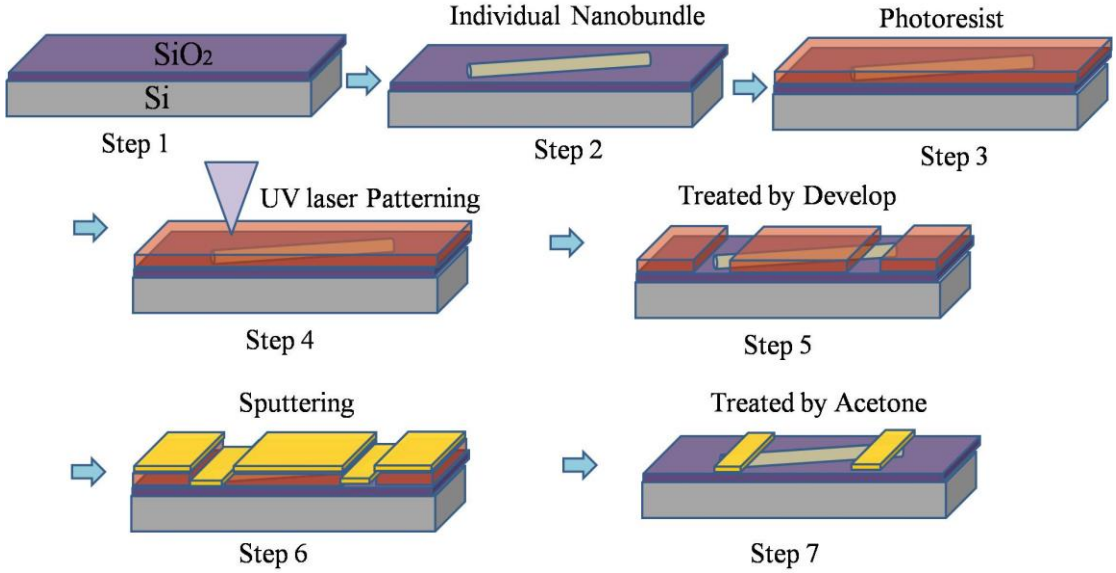

Figure 2.2 Schematic images display the fabrication process of individual nanobundle electrode.

UV lithography method is utilized to fabricate individual nanobundle electrode device. 7 schematic images in Figure 2.2 illustrate the preparation process. The Si wafer with 100 nm SiO_2 layer is properly cut into 1 cm x 1 cm size. These SiO_2/Si substrates are cleaned by sonicating in deionized water and isopropanol for 15 mins respectively, and dried by nitrogen gas flow (step 1). Individual K_xMoO_3 nanobundle is then transferred to the centre of clean substrate by the needle of micro-probe-station under microscope (step 2). The positive photoresist AZ1518 is spin coated onto the substrate with the thickness of 2 μm (step 3). The thickness of photoresist is optimized, while thinner one could not properly cover the nanobundle and thicker one will result in inconvenience of removing polymer. We design electrode patterns by the help of AutoCAD software, and load the design into the computer that controls the laser writing system. The laser writing system we use is uPG101 from Heidelberg Instrument Co. as shown in Figure 2.3(a). The substrate is placed in the centre of platform. There are holes on the platform and air pumping is performed, which tightly suck substrate on the platform by air pressure. UV laser is focused onto the substrate and moving around controlled by computer (step 4). The laser power is optimized according to the thickness of photoresist. The written substrate is then immersed into a developer, removing the part exposed to UV laser (step 5). The patterned substrates are collected and placed inside the sputtering chamber. The sputtering system is displayed in Figure 2.3(b). In the system, plasma hit the metal target, driving atoms ejected from target. Most of the metal atoms diffuse to nearby substrates, and finally, a layer of material is covered on the patterned substrate. In our case, 20 nm Cr layer is first sputtered on the substrate to firmly adhere the Au layer with SiO_2 substrate. 500 nm Au layer is then deposited on the Cr layer (step 6). The sputtered substrate is treated by acetone solution, removing the remaining photoresist and the metal layer covering on it (step 7). In the end, the device with Au finger electrodes covering on individual nanobundle is fabricated.

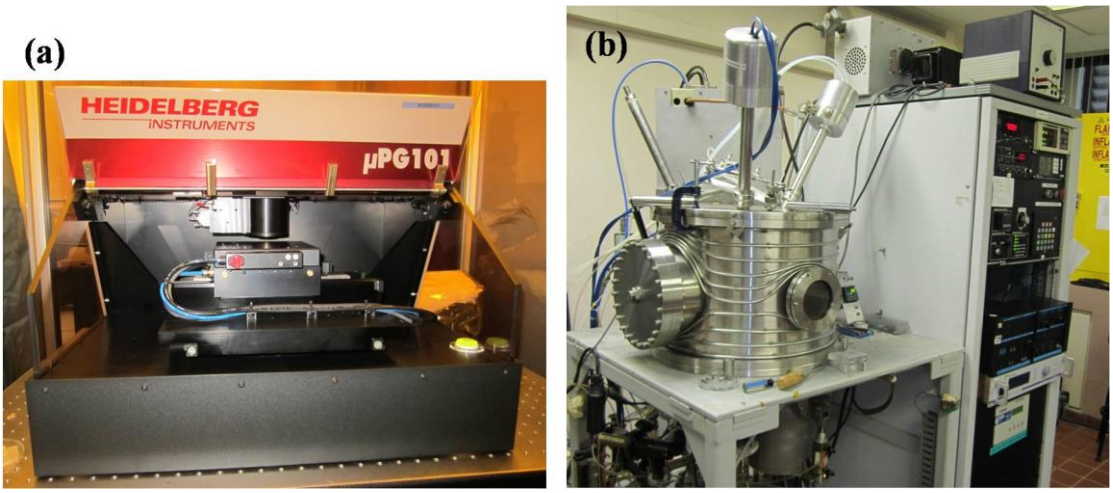

Figure 2.3 Optical image of (a) Laser Writing system (b) Sputtering system.

After the fabrication of electrode device, copper wires are used to connect the device with sourcemeter to form a circuit. One end of copper wires are connected to the electrode by soldering and the other end of wires are connected to crocodile clips. The electrical measurements are carried out using Keithley 6430 Sub-fA Remote SourceMeter.

2.4 Focused Laser System

To investigate the photo-electrical response of individual nanostructure, laser beam should be focused and directed onto nanostructure. Thus, the focused laser system is set up to couple laser beam into microscope. Here we will describe in detail the components of the focused laser system.

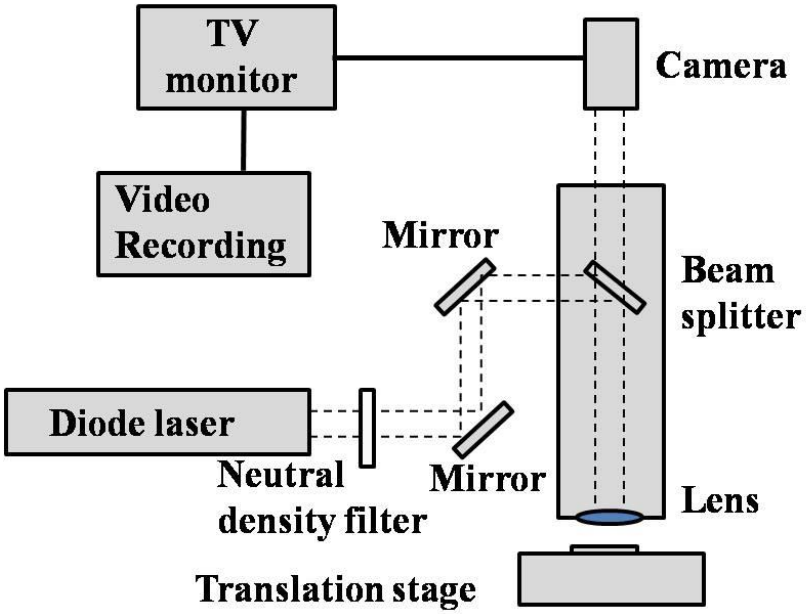

Figure 2.4 Schematic of photon response measurement set-up with focused laser beam radiation on nanostructure.

Figure 2.4 shows the schematic of the photon response measurement set-up with focused laser beam irradiation on nanostructure. The single mode, linearly polarized diode red laser beam (Intellite RS655-70, λ=660 nm) is directed into the microscope via two mirrors as shown. The mirrors are utilized to align the beam in right angle, which provide convenience for laser alignment. The optical microscope is custom made including an additional hole on one side to allow the laser beam to enter. Inside the microscope, the laser beam is reflected by a beam splitter towards the objective lens. We use Nikon 50× lens with a numerical aperture of 0.55 and a long working distance of 8.7 mm. The objective lens focuses the laser beam onto the individual nanostructure device positioned on the translation stage. A CCD camera is mounted on the top of microscope, and connected to a television monitor and a computer. The computer with recording software captures the laser illumination process in real time. The power of the laser beam after passing through the setup is measured around 30% of the original laser output, ranged from 1~20 mW. The diameter of focused laser spot is ~6 μm. Illumination of the sample is provided by the optical microscope light source.

Chapter 3 Intercalate K ions into MoO_3 layered nanostructure

In this chapter, we describe the simple one-step method to synthesize K ion intercalated MoO_3 nanostructure, the various experimental characterization techniques and density functional theory calculation utilized to identify the structure of the material, and the growth mechanism of intercalated nanostructure.

3.1 Synthesis of K ion intercalated MoO_3 nanobundle

We begin with a Mo foil (5 mm×5 mm×0.05 mm, from Aldrich Chemical Co., Inc.) as Mo source. The foil is treated in the process described in Chapter 2 and placed in the middle of ceramic boat. A muscovite mica sheet ($K_2O•3Al_2O_3•6SiO_2•2H_2O$, 8 mm×8 mm, from Alfa Aesar Co., Inc.) is prepared as substrate and K source. The mica sheet is placed 1mm on top of the Mo foil supported by Si substrate in the ceramic boat. The system is inserted into the tube furnace (Carbolite MTF 12/25/250) and heated for 6 hrs in ambient at 600 ℃. At one end, air flow is controlled by fan to provide adequate oxygen continuously. The synthetic scheme of the K-intercalated MoO_3 nanostructure described above is shown in Figure 3.1(a). Figure 3.1(b) displays the photograph of the tube furnace used to fabricate the nanomaterial.

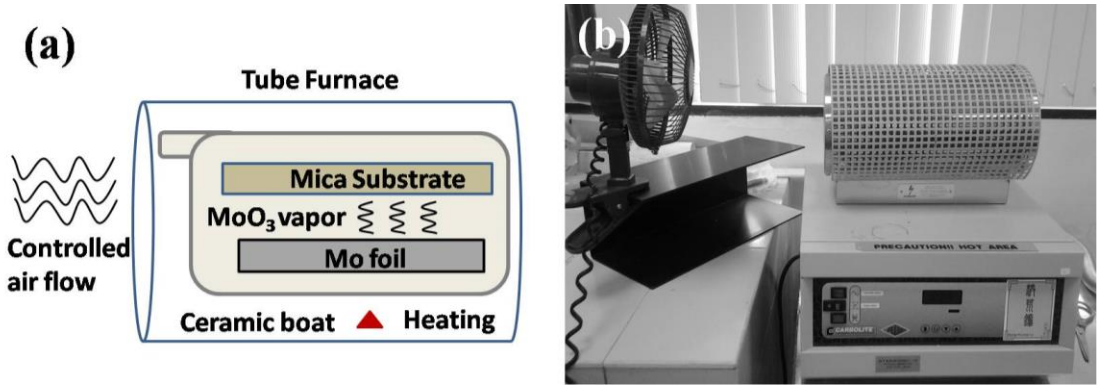

Figure 3.1 (a) Schematic representation of the synthesis system (b) Photograph of the tube furnace used to fabricate nanomaterial.

During the growth, adequate oxygen is required to successfully synthesize K_xMoO_3 nanostructure. We have tried two systems with insufficient oxygen. In one system, the prepared ceramic boat is loaded into sealed tube furnace by supplying 10% O_2. For the insufficient oxygen, nothing is produced on the substrate. In the other system, the prepared ceramic boat is loaded into unsealed tube furnace without fan. Upon heating in ambient, little fresh air flows into the tube. With the continuously usage of O_2 in the middle of the tube furnace, oxygen is not adequate for nanomaterial growth. Consequently, a fan near the tube furnace is utilized to provide fresh air continuously. Meanwhile, mica substrate is elevated 1 mm above the Mo foil supported by small pieces of Si substrate to accommodate sufficient oxygen for reaction. Temperature for nanostructure synthesis is optimized as well. K_xMoO_3 nanostructures are produced in the temperature window ranged from 580 ℃ to 650 ℃, while only MoO_3 microbelts are observed when temperature is out of the range.

3.2 Characterization of K ion intercalated MoO_3 nanobundle

After the synthesis process described above, the ceramic boat is cooled down to room temperature, and mica substrates are moved for further characterization. These characterization methods include morphology characterization by SEM, elemental

composition and chemical state detection by EDX and XPS, lattice structure determination by TEM, XRD and Raman Spectroscopy.

Characterization 1: Morphology

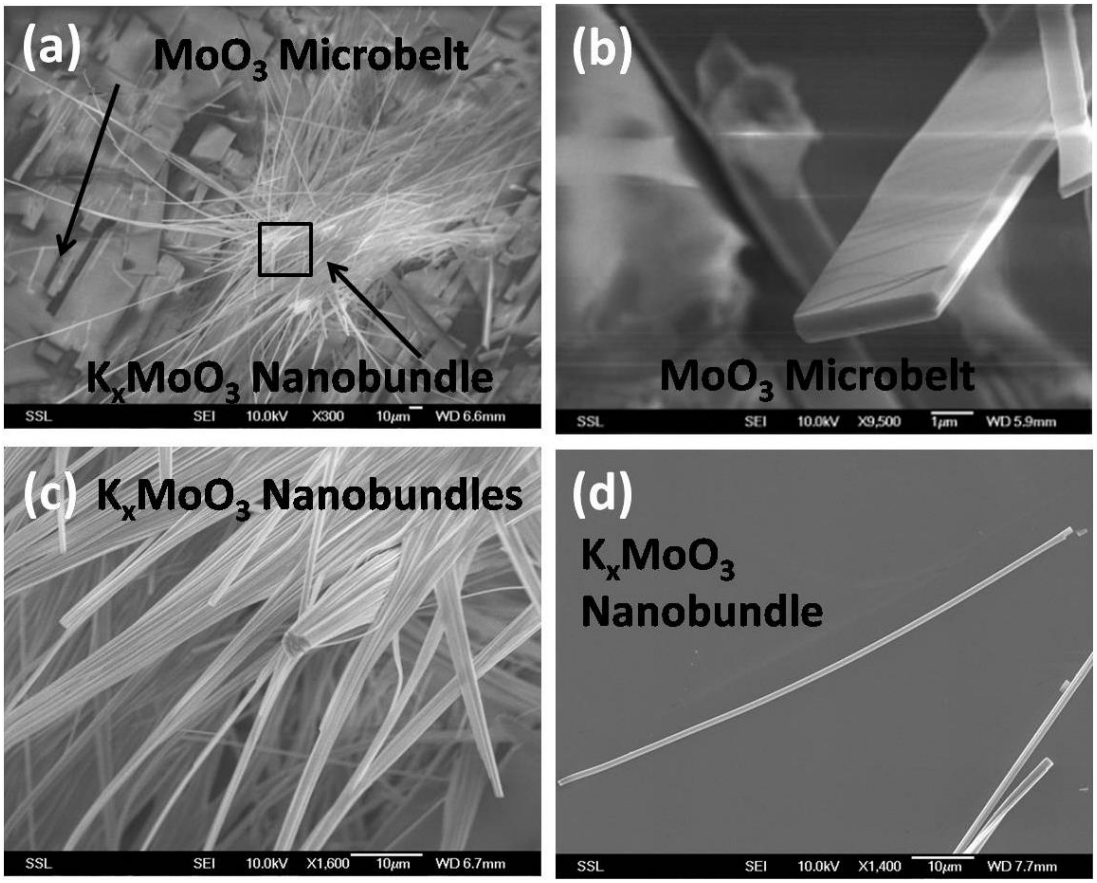

Figure 3.2 (a) SEM image of grown muscovite mica substrate with K_xMoO_3 nanobundles extending out of substrate and MoO_3 microbelts lying down on substrate (b) Typical morphology of individual MoO_3 microbelt (c) Zoom in image in the middle where nanobundles grow highlighted by black square in (a). (d) Typical morphology of a single K_xMoO_3 nanobundle.

In the synthesis process, Mo atoms evaporate from the foil and are oxidized in the air flow. The deposition of the oxidized Mo vapor on the mica substrate produces two different types of products as shown in Figure 3.2(a). The first type of the materials are MoO_3 microbelts lying down on mica substrate with a width of 3~5 μm, a length of 10~15 μm and a thickness of 1μm. These microbelts are dominating products. Figure 3.2(b) displays the typical morphology of individual MoO_3 microbelt with the

length, width and thickness of 11 μm, 1.0 μm and 3.5 μm respectively. Another type of the materials are K_xMoO_3 nanobundles extending out of the substrate, with the length about 200~300 μm. Figure 3.2(c) is the zoom in image in the middle where nanobundles grow highlighted by black square in Figure 3.2(a). Significant number of nanobundles are packed in bundles and extend out. Single nanobundle is transferred to Si substrate for further observation. Since the end of the nanobundle is firmly attached to the mica substrate, only segment of nanobundle is transferred. Figure 3.2(d) shows morphology of a typical nanobundle with the length, width and thickness of 100 μm, 0.9 μm and 0.5 μm respectively.

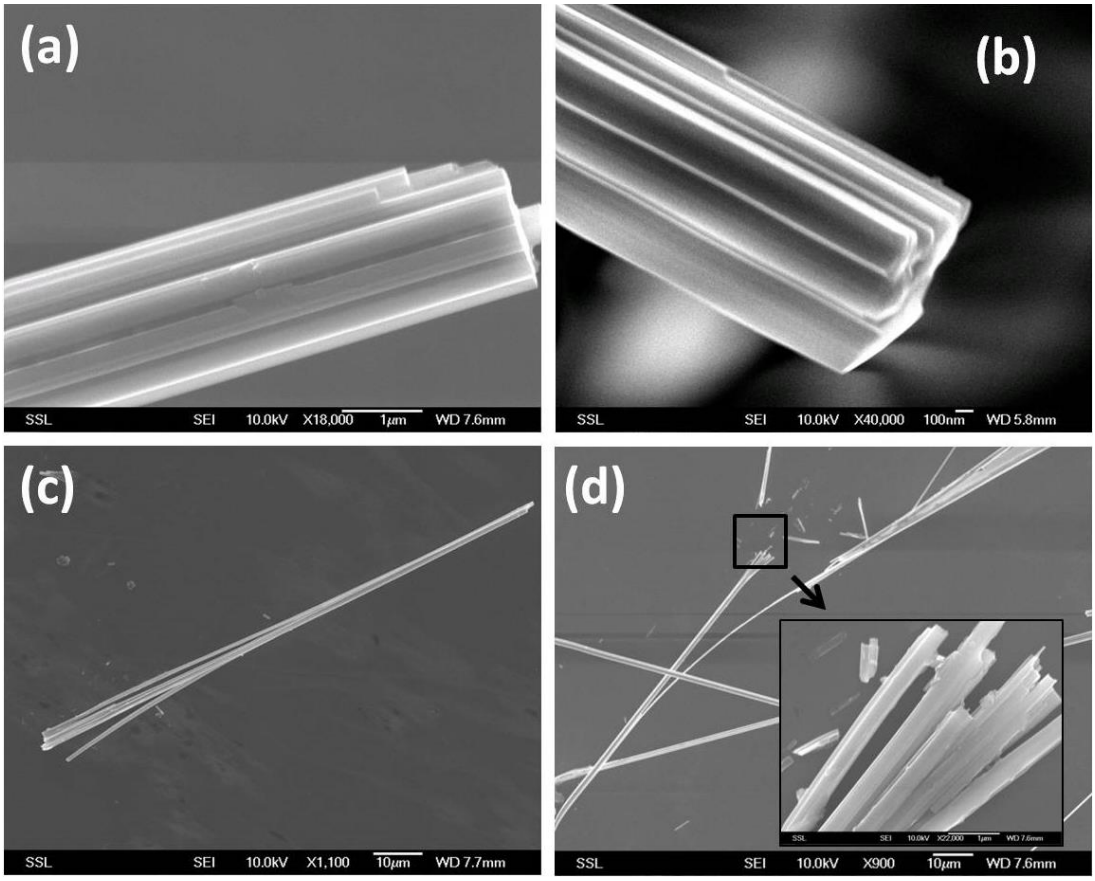

Figure 3.3 (a~b) zoom in image of the end of K_xMoO_3 nanobundle (c) Nanobelts split from each other in the left end of K_xMoO_3 nanobundle (d) K_xMoO_3 nanobundle broke in the middle, inset image is the enlarged broken edge of nanobundle highlighted by black square.

Figure 3.3(a) displays the enlarged image of the right end of the nanobundle. Clearly, the nanobundle is constructed by several parallel nanobelts. These nanobelts are of the same length as the nanobundle but much thinner with a width and a

thickness of approximately 300 nm and 150 nm, respectively. In nanobundles, nanobelts are packed in different patterns. In Figure 3.3(a), three nanobelts align in one line and four lines of nanobelts stack regularly forming a rectangle side view. In Figure 3.3(b), each nanobelts possesses different orientations, and all nanobelts are packed into a triangle shape. Although the morphology of nanobundles are not exactly the same, the phenomena that nanobundle is packed by several nanobelts is always observed.

During transferring process, due to the stress applied by the needle of micro-probe-station, nanobelts in individual nanobundle split or nanobundle breaks in the middle. Figure 3.3(c) displays nanobelts split in the left end of nanobundle after transferring while right end of nanobundle is still packed. Clearly that the nanobundle is constructed by nanobelts and these nanobelts are not tightly packed as a unit, which can be peeled by stress. Figure 3.3(d) shows one long nanobundle broke in the middle during the transferring process, the inset image displays the enlarged broken edge highlighted by black square in Figure 3.3(d). In the enlarged image, nanobelts split from each other under stress, but every nanobelts keeps its morphology without being destroyed, suggesting that inner part of nanobundle is also constructed by these small nanobelts and they can split from each other with the intact of nanobelt morphology.

By morphology characterization, two types of products with distinct morphology are observed after synthesis, one with microbelt morphology and the other one with nanobundle configuration. Elemental composition and chemical state detection is carried out next to identify these two materials.

Characterization 2: Elemental composition and chemical state

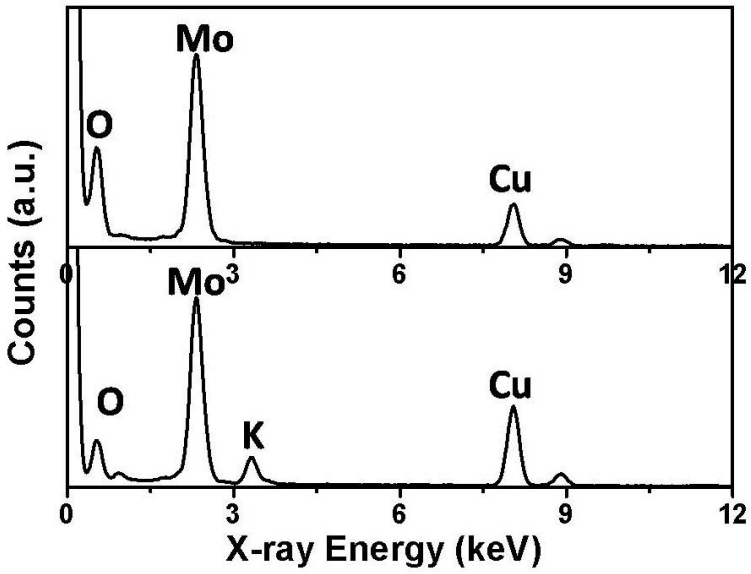

Figure 3.4 EDX spectrum of MoO_3 microbelt (upper curve) and K_xMoO_3 nanobundle (lower curve).

EDX spectrum elemental analysis in TEM on the two types of products (microbelt and nanobundle) is carried out to identify the material. The upper curve in Figure 3.4 shows EDX spectrum of individual microbelt, it reveals that the microbelt contains Mo and O as constituents, while Cu peaks come from TEM grid, denoting the microbelt is MoO_3. The EDX spectrum of single nanobundle is shown in the lower curve of Figure 3.4. Beside the Mo, O and Cu peaks, a significant K peak is observed, denoting a high percentage of potassium atoms in the nanobundle. The atomic percentage ratio of K over Mo is fixed in the same nanobundle but differs slightly between different nanobundles. We can denote the nanobundle as K_xMoO_3 with x ranging from 0.20 to 0.25. Compared with result of MoO_3 microbelts, the atomic ratio of O over Mo in the nanobundles is roughly 2.6±0.2, which is lower than the value in stoichiometric MoO_3 compound, implying that O vacancies may exist. Revealed by stoichiometry of nanobundle, valences of Mo is speculated from 4.6 to 5.4. Additional investigation on the valencies of the Mo was carried out via XPS study.

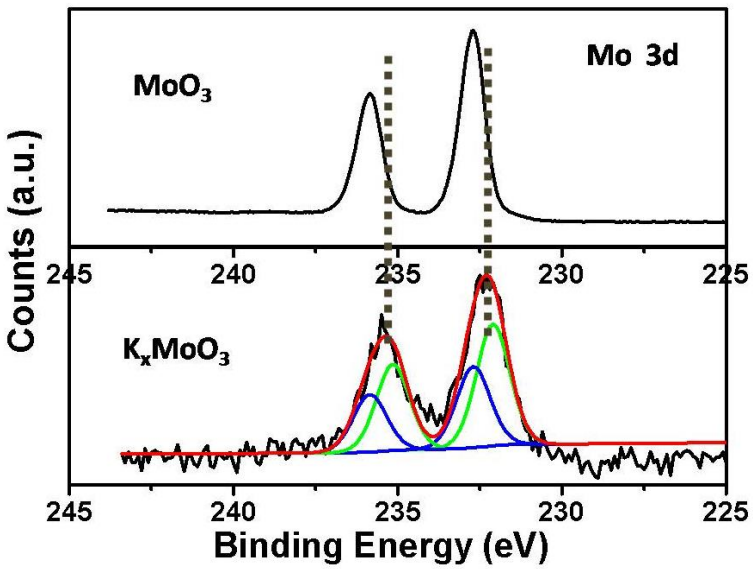

Figure 3.5 XPS spectrum of MoO_3 microbelt (upper curve) and K_xMoO_3 nanobundle (lower curve).

We performed a XPS experiment to measure the valence variation of the Mo atoms in the nanobundle upon K intercalation using the MoO_3 microbelts and transferred K_xMoO_3 nanobundles. The upper curve in Figure 3.5 shows XPS spectra of microbelt, the two peaks at position of 235.8 eV (Mo3d 3/2) and 232.7 eV (Mo3d 5/2) illustrate the valencies of Mo is 6+.[49] Consequently, the microbelts are identified as MoO_3 microbelts. The black curve in lower chart of Figure 3.5 shows the measured XPS spectra of nanobundle with peak position at 235.3 eV (Mo3d 3/2) and 232.2 eV (Mo3d 5/2). The right-shifted peaks suggest the reduction from Mo^{6+} towards Mo^{5+}. To precisely identify the valence, the curve is peak fitted by Mo^{6+} peaks (red peaks 235.8 eV (Mo3d 3/2) and 232.7 eV (Mo3d 5/2)) and Mo^{5+} peaks (blue peaks 235.1 eV (Mo3d 3/2) and 232.0 eV (Mo3d 5/2)).[50] The area ratio of Mo^{5+} over Mo^{6+} is around 1.5, suggesting the valencies of Mo roughly +5.4, which is consistent with the estimation from stoichiometry of nanobundle.

By EDX and XPS measurement, we confirm that K ion intercalated MoO_3 nanostructures are successfully synthesized, and the ion intercalation reduces part of Mo atoms from +6 to +5. To understand the effect of ion intercalation imposing on the MoO_3 structure, lattice structure determination is carried out.

Characterization 3: Lattice Structure

As reported, intercalation ions would induce expansion of lattice and transform the crystalline structure into amorphous structure when great amount of ions or large size ions are intercalated.[29, 42] To explore the lattice structure after intercalation, we subsequently remove the MoO_3 microbelts and K_xMoO_3 nanobundles from the substrate and transfer them to the TEM grid for further characterization. The selected area electron diffraction (SAED) pattern of the MoO_3 microbelts on the (010) surface orientation is shown in Figure 3.6 and the inset image shows the SEM image of the MoO_3 microbelts along the [001] growth direction. The microbelts exhibit a typical rectangular diffraction pattern on the (010) surface as highlighted by yellow rectangle in the figure. The diffraction pattern denotes that the lattice adopting an orthorhombic lattice structure, same as bulk MoO_3. Based on the diffraction pattern on (010) surface of MoO_3 microbelt, we derive the lattice constants *a* and *c* as *a* = 4.01 Å and *c*= 3.69 Å. The value is in excellent agreement with the reported experimental XRD data.[51]

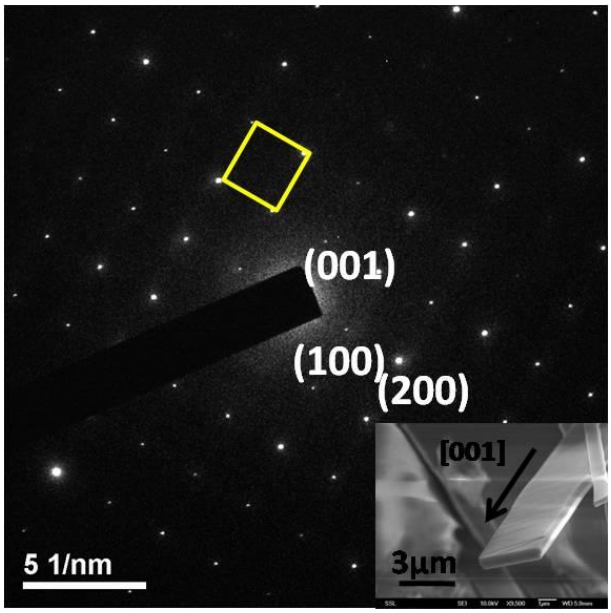

Figure 3.6 Electron diffraction pattern of the MoO_3 microbelt on the (010) surface. The highlighted yellow rectangle denotes the orthorhombic lattice structure. The inset image shows a SEM image of the typical MoO_3 microbelt growing in the [001] direction.

The SAED pattern of the K_xMoO_3 nanobundles on the (010) surface is shown in Figure 3.7(a) with the inset image displaying a low-magnification TEM image of the

nanobundles along the [001] growth direction. The highlighted yellow rectangular diffraction pattern formed by large bright spots represents K intercalated MoO_3 structure on the (010) surface. The rectangular diffraction pattern indicates that K_xMoO_3 nanobundles are single crystalline materials with orthorhombic lattice structure. It suggests that the orthorhombic structure of MoO_3 is maintained upon insertion of significant amount of K atoms. Between every two bright spots there are five weaker, evenly-distributed spots along the [100] direction of the K_xMoO_3 nanobundles (highlighted by white arrow). These smaller diffraction spots suggest that K_xMoO_3 nanobundles possess a periodic superstructure with 6 primitive cells along the [100] direction.

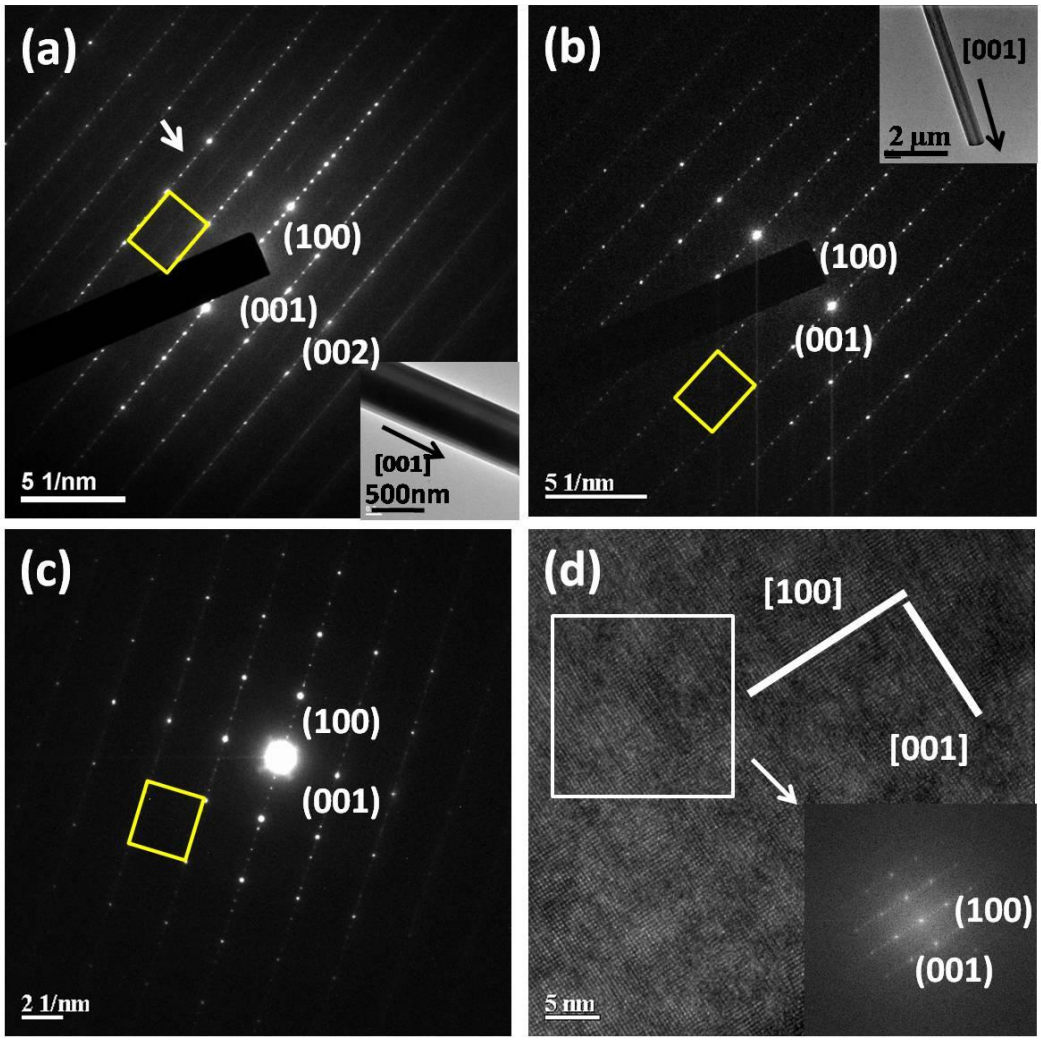

Figure 3.7 (a~c) Electron diffraction pattern K_xMoO_3 nanobundle on (010) surface, the highlighted yellow rectangle constructed by large bright spots represents lattice structure of K intercalated MoO_3, inset image in (a~b) shows TEM image of typical

K_xMoO_3 nanobundle growing in [001] direction. (d) HRTEM image of K_xMoO_3 nanobundle, inset image is FFT analysis of select area highlighted by white square.

More diffraction patterns of different K_xMoO_3 nanobundles are shown in Figure 3.7(b~c). Although the spacing between spots varies in nanobundles with different K atomic percentage, same diffraction pattern is observed. In Figure 3.7(c), for the middle brightest spot is not covered, the weaker spots are not all distinct, but blur lines formed by these weaker sports along [100] direction are still visible. The rectangular diffraction pattern and these smaller diffraction spots in all figures illustrate that all K_xMoO_3 nanobundles with x range from 0.20 to 0.25 possess the same orthorhombic lattice structure and periodic superstructure. The HRTEM image is acquired to reveal the detailed structure of the nanobundle as shown in Figure 3.7(d). Fourier transformation (FFT) analysis of select area in HRTEM image highlighted by white square is shown in inset image. Same diffraction pattern is observed. Bright spots appear in rectangular configuration and 5 weaker spots evenly distribute between every two bright spots along [100] direction. The FFT analysis demonstrates that every area on the nanobundle possesses same orthorhombic lattice structure and periodic superstructure.

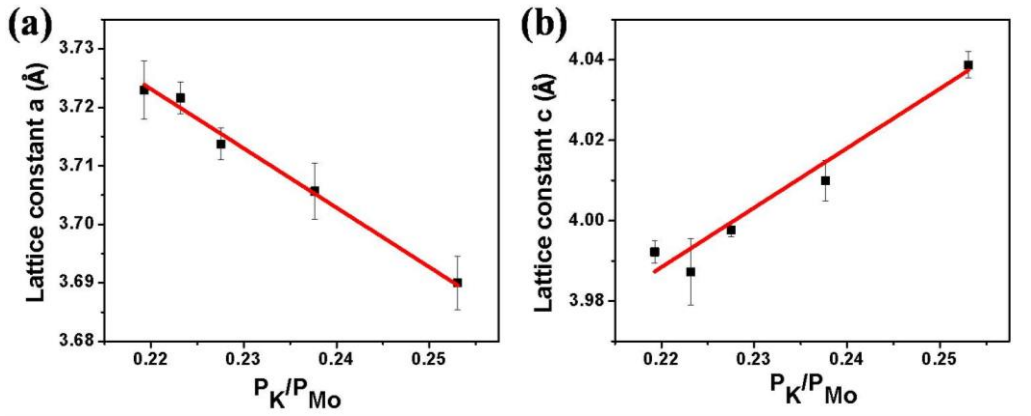

Figure 3.8 (a~b) Black square spots shows calculated lattice constant *a*, *c* in different nanobundles with varied atomic percentage ratio of K over Mo, red lines are the fitted lines correspondingly.

Based on the TEM diffraction pattern of K_xMoO_3 nanobundles with varied K atomic percentage, we derive the lattice constants *a* and *c* of the K_xMoO_3 nanobundles

with different atomic percentage ratio of K over Mo as shown in Figure 3.8(a) and (b) respectively. Compared with reported lattice constant of MoO_3 that a = 3.96 Å and c= 3.70 Å,[51] significant lattice change is observed with the contract of the a axis and expansion of the c axis by approximately 0.3 Å upon K insertion. As the atomic percentage ratio of K over Mo increases from 0.22 to 0.25, the lattice constant a decreases from 3.72Å to 3.69Å while the lattice constant c increases from 3.98 Å to 4.04 Å. Linear lines are fitted according to the calculated value. It shows that upon the K uptake lattice constant a linearly shrinks and it decreases more when greater amount of K atoms are intercalated, while lattice constant c behaves in opposite trend. The intercept of linear fitting lines in Figure 3.8(a) and (b) are 3.95 Å and 3.67 Å respectively. Both values are near the cell parameter of MoO_3. It denotes that when no K atoms are inserted, the structure is exactly the same as MoO_3, and the lattice structure gradually deforms as more K atoms are intercalated. Of course we cannot put more K ions in (atomic percentage ratio K/Mo >0.25) since this depends on the concentration of K ions in mica substrate.

For the relatively larger size of nanobundle width than thickness, the transferred nanobundles are placed on the TEM grid with the [010] direction perpendicular to the grid. Although the grid could be made to tilt by 15°, we are unable to find a clear diffraction pattern that contains information along the [010] direction. Instead, we utilize X-ray diffraction to further resolve the structure of the K_xMoO_3 nanobundles.

Two pieces of mica substrate are used to produce materials at different temperatures for XRD analysis. During the growth, mica substrate A is heated at 500 °C while mica substrate B is heated at 600 °C. Due to the significant role mica substrate plays in growing K_xMoO_3 nanobundles, the temperature to successfully synthesize K_xMoO_3 nanobundle is limited due to mica properties. Muscovite can be synthesized by hydrothermal treatment of mixtures at 650-700 °C, which suggests the surface melting point of muscovite mica roughly lies within 600-650 °C.[52] To form

K_xMoO_3 liquid islands, surface of mica should be partly melted to react with MoO_3 vapour. Consequently, the heating temperature required to grow K_xMoO_3 nanobundles should around 600 °C. As a result, only MoO_3 mircobelts are produced on substrate A while both MoO_3 mircobelts and K_xMoO_3 nanobundles are observed on substrate B.

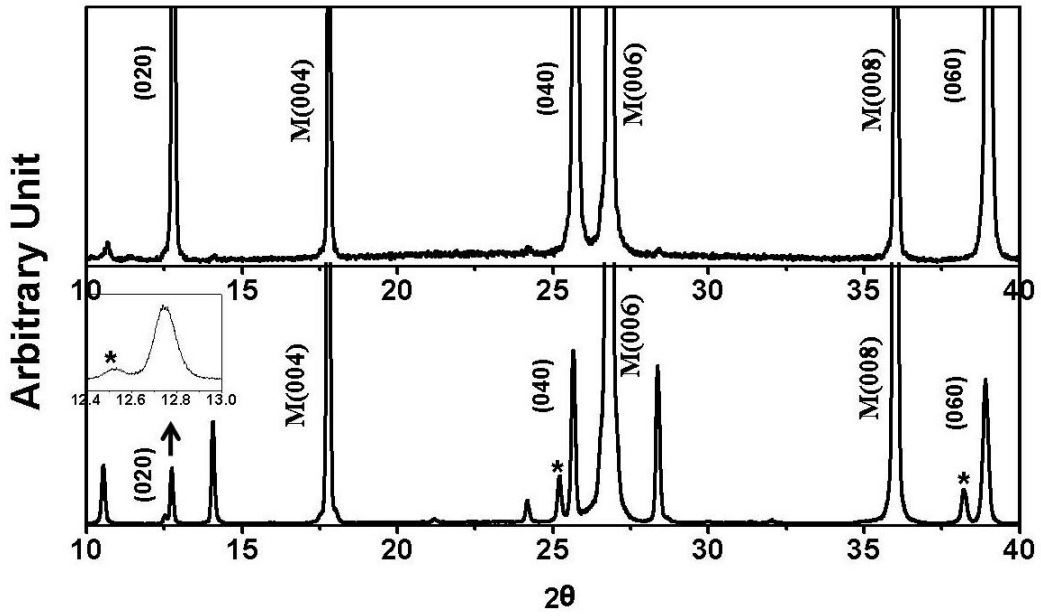

Figure 3.9 The XRD spectrum of the mica substrate A with the MoO_3 microbelts (upper chart) and the mica substrate B with both the MoO_3 microbelts and the K_xMoO_3 nanobundles (lower chart). The label peaks with M are muscovite peaks while the label peaks without notation are MoO_3 peaks. The three peaks that are labelled with asterisks denote the layered structure of K_xMoO_3 correspond to expand along (020), (040) and (060). The rest of the peaks could be attributed to other faces of K_xMoO_3.

Figure 3.9 displays the XRD measurement of substrate A (upper curve) and substrate B (lower curve). In two curves, the peaks that labelled with M come from mica substrate and the peaks that labelled with (020), (040), (060) denoting the layered structure of MoO_3 microbelts. According to these three peaks, the lattice constant *b* of MoO_3 microbelts is calculated as 13.87 Å, in well agreement with reported value.[51] Three new peaks highlighted with stars next to (020), (040), (060) surface of MoO_3 appear in lower chart due to the significant amount of K_xMoO_3 nanobundles on substrate B. Compared with these three peaks of MoO_3, the left shifted peaks of K_xMoO_3 nanobundles suggest the expansion of lattice constant *b* upon K

intercalation. There are still some unlabeled peaks on substrate B, they should denote other surfaces of K_xMoO_3 nanobundle.

The calculated lattice constant *b* of K_xMoO_3 nanobundle is 14.16 Å and the value is derived using the apex of the peaks in XRD spectrum from the most abundant nanobundles over the range of K contents (for x from 0.20 to 0.25). It is anticipated that the real value of *b* in individual nanobundle should be lower for x near 0.20 and higher for x close to 0.25 since a higher K content naturally leads to greater lattice expansion. Compared with the reported value in MoO_3 lattice *b* =13.86 Å, the structure expands by 0.3 Å. Considering the high atomic percentage ratio of intercalated K atoms and large radius of K (1.5 Å), the expansion in *b* axis (0.3 Å) is comparatively small. The XRD spectrum of the K_xMoO_3 nanobundles clearly indicates that the complex preserves a layered structure as evidenced by the significant peaks located at (020), (040) and (060). This is distinctively different from the XRD analysis reported by Sian *et al.*,[11] in which the intensity of all the peaks associated with MoO_3 was reduced with the increase of the K contents and, in particular, all peaks vanished upon *x* reaching 0.2, indicating the complete loss of the initially layered structure.

Raman spectroscopy study also provides further insights about atomic structure. Upper chart in Figure 3.10 shows the Raman structure of individual MoO_3 microbelt on silicon substrate. Strong peaks in the range of 600-1000 cm^{-1} correspond to stretching modes of MoO_6 octahedra in three directions, 996 cm^{-1} (A_g, ν_{as} Mo=O stretch in [010] direction), 819 cm^{-1} (A_g, ν_{as} Mo=O stretch in [100] direction) and 668 cm^{-1} (B_{2g}, B_{3g}, ν_{as} O-Mo-O stretch in [001] direction).[53, 54] Peaks observed in the 400-200 cm^{-1} range correspond to various bending modes of the orthorhombic MoO_3 crystal. The peak at 518 cm^{-1} comes from Si substrate. The vibration of Mo-O bond would shift to lower wavenumbers when bond length increases.[55, 56] According to the lattice constant analysis in the above discussion, the expansion of lattice constant *b* and *c* suggests the increase of Mo-O bond length in [010] and [001] direction, thus in

the Raman spectrum of single K_xMoO_3 nanobundle as shown in lower chart in Figure 3.10, the 996 cm^{-1} and 668 cm^{-1} peaks shift leftwards to 946 cm^{-1} and 630 cm^{-1}. While the shrinkage of lattice constant *a*, explains the rightward shift peak at 820 cm^{-1}. Considering the periodic superstructure along [100] direction with spacing of 6 primitive cells, it is possible that three kinds of Mo=O bonds with different bond length arrange in certain sequence in every 6 cells in [100] direction due to the stress upon K intercalation in MoO_3 structure. Consequently, the 820 cm^{-1} peak right shifts and splits into three peaks of 820 cm^{-1},841 cm^{-1} and 866 cm^{-1} respectively.

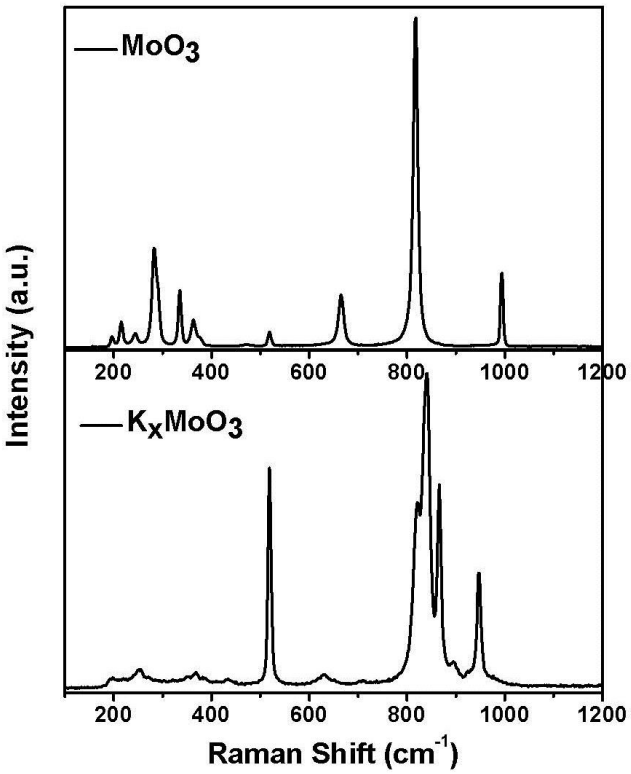

Figure 3.10 Raman spectrums of individual MoO_3 microbelt and K_xMoO_3 nanobundle on Si substrate.

After lattice structure determination, we find that with great amount of large size ion insertion (1.5 Å in size and ~0.2 in atomic ratio), the orthorhombic structure and layered structure of MoO_3 preserves with small lattice constant adjustment. Especially, the lattice expansion in *b* axis is amazingly small compared with the atomic size. To achieve a thorough understanding about the structure after ion insertion, theoretical calculation is performed in the following.

3.3 Theoretical Simulation of K_xMoO_3 nanobundle structure

To interpret the experimental results and clearly identify the atomic structure, we perform density functional theory calculations to understand the structures and properties of the pure and K-intercalated MoO_3 materials. Compared with the size of atoms, the thicknesses and widths of the MoO_3 microbelts and the K_xMoO_3 nanobundles are several orders of magnitude larger. Therefore, it is justified to model these nanomaterials with 3-dimensional periodic bulk-like structures, assuming that the edge effects on structures and physical properties are insignificant. All simulations are carried out using the Perdew-Burke-Ernzerhof (PBE) exchange-correlation functional under the generalized gradient approximation as implemented in the Vienna *Ab-initio* Simulation Package (VASP). The projector augmented wave (PAW) method is used to describe the core electrons of the atoms, and the valence orbitals are represented with a plane wave basis set with a cutoff energy of 450.0 eV. All calculations are performed using a spin-polarization scheme. The brillouin zone integration is performed using a 4×2×4 Monkhorst-Pack *k*-point mesh. For calculations of the band structure (BS) and density of states (DOS), the *k*-points mesh is doubled. The conjugate gradient algorithm is selected to optimize both the ion positions and the lattice parameters with no constraint. The energy and SCF convergence threshold is set to be 5.0×10^{-5} and 1.0×10^{-5} eV, respectively.

A 2×1×2 supercell of the MoO_3 primitive lattice containing 16 Mo atoms and 48 O atoms (Figure 3.11(a)) is first selected to model the MoO_3 microbelts. The fully optimized lattice structure of the MoO_3 supercell, shown in Table 3.1, is in excellent agreement with the experimental result and reported experimental XRD data,[51] suggesting that our computational method is reliable for structural predictions for the type of materials we deal with.

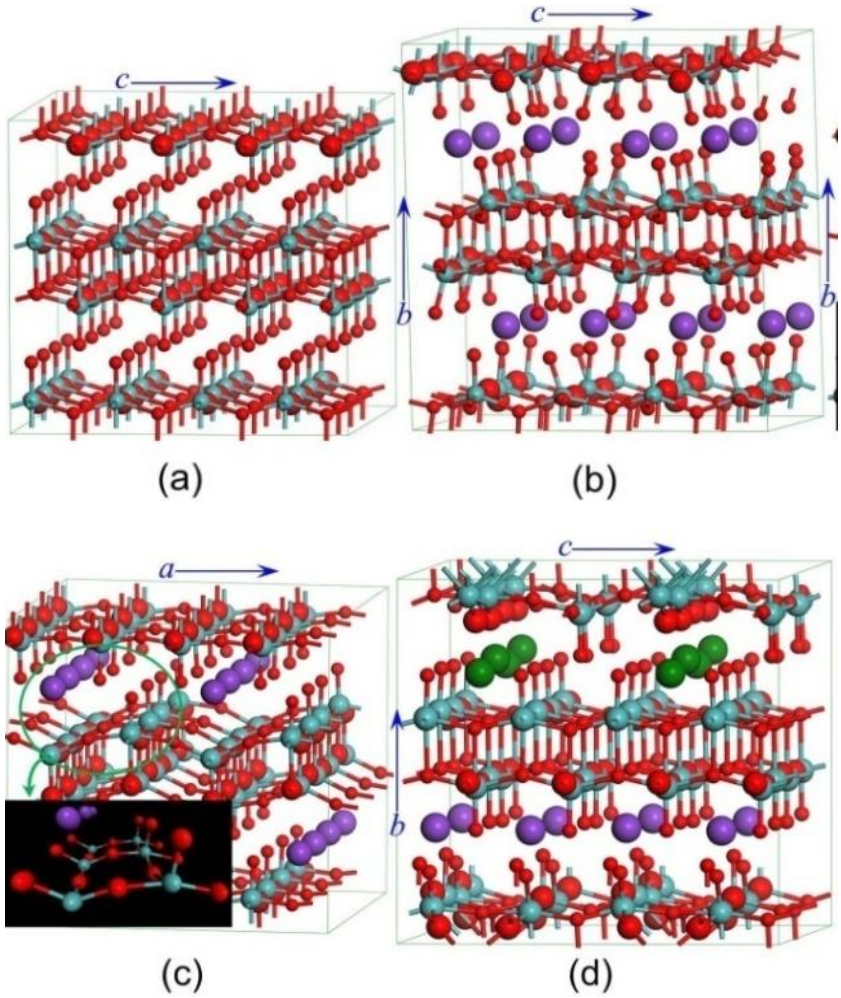

Figure 3.11 The optimized structure of (a) the pure MoO_3, and K_xMoO_3 structure with (b) K as intercalants, (c) K as occupants and (d) mixed. In the structures, red balls represent O atoms, blue balls represent Mo atoms and purple balls represent intercalated K atoms. In the mixed case, the purple and green balls represent intercalants and occupants, respectively.

Table 3.1 The measured and calculated lattice constants of the MoO_3 microbelt and the K_xMoO_3 nanobundle.

		a(Å)	*b*(Å)	*c*(Å)
MoO_3	Exp	4.01	13.87	3.69
	Calc	3.91	13.76	3.71
	Rep[51]	3.96	13.86	3.70
K_xMoO_3	Exp	3.69-3.72	14.16	3.97-4.05
	Calc[a]	3.82	14.89	3.81
	[b]	3.73	14.25	3.86
	[c]	3.80	14.56	3.81

K as [a] intercalants, [b] occupants and [c] mixed (half intercalants and half occupants).

Subsequently, we explore the lattice structure of K_xMoO_3 with various scenarios of K atoms acting as intercalants, as lattice occupants at oxygen vacancies or as both in the supercell for x=0.25. In the case of K intercalation, the K atoms are placed in between the MoO_3 layers (Figure 3.11(b)). In occupation case, to model the O vacancies in the lattice, we remove one dangling O atom between the layers for each K atom introduced (Figure 3.11(c)). For K atoms act as both intercalants and occupants, we substitute two terminal O atoms with K atoms and place two K atoms as intercalants in the supercell (Figure 3.11(d)). In all cases, various K distribution configurations are calculated and, upon full lattice optimization, the lowest energy configurations are obtained. The optimized structures and the cell parameters are shown in Figure 3.11 and Table 3.1, respectively. Clearly, only in the case where the K atoms act as occupants the calculated K_xMoO_3 cell parameters *a*, *b* and *c* are in good agreement with the experimental data. In the other two scenarios K-uptake in the lattice results in significantly higher lattice expansion (greater value of lattice constant *b*) than what is observed experimentally. Furthermore, the calculated average cohesive energies of -7.94 eV (occupants), -7.80 eV (intercalants) and -7.88 eV (mixed) indicate that the K occupation at the oxygen vacancy sites is indeed energetically preferred.

According to the theoretical calculation, K atoms most possibly locate in the oxygen vacancies in the MoO_3 structure, which results in the amazingly small expansion in *b* axis. This is also consistent with the experimental fact that the atomic ratio of O over Mo in the K_xMoO_3 nanobundle is lower than the stoichiometric value due to the existence of O vacancies.

3.4 Growth Mechanism of K_xMoO_3 nanobundle

We have successfully synthesized K ion intercalated MoO_3 nanostructure without destroying the structure of MoO_3 by the simple thermal evaporation method on muscovite mica substrate, which is not reported before. To further increase the

production and apply the simple method to synthesize other metal oxide nanostructure, we study the growth mechanism of K_xMoO_3 nanobundles.

Muscovite mica $K(Al_2)(Si_3Al)O_{10}(OH)_2$, possesses laminated structure with potassium locating between the lamellae.[57] Each lamella containing several layers displays typical structure of phyllosilicates. Potassium atoms easily diffuse between lamellae, which facile the release from mica to solution.[58, 59] Considering the high diffusion coefficient of K in mica and the presence of K in nanobundles, we speculate that K atoms are absorbed from mica substrate to K_xMoO_3 nanobundle. To reveal the flow of K atoms in mica during growth process, two pieces of mica substrates are prepared for EDX Spectrum analysis in SEM.

Table 3.2 Atomic percentage of compounds in mica (unit: %)

	Pure Mica	Treated Mica		
		Area A	Area B	Area C
Al	15.76	15.76	15.87	15.73
Si	18.65	18.17	18.19	18.72
K	1.79	0.41	1.00	1.79
Mo	0	1.34	0	0

The first piece of mica substrate is used as control, and the second piece is used for the growth of nanobundle and then subsequently all products are sonicated away. On second piece of mica, different areas are studied. Area A is the position where K_xMoO_3 nanobundles grew before, it includes grain boundaries. Area B is the place where MoO_3 microbelts grew before and it is near Areas A. Area C is near the edge of mica, where nothing grew on it before. Table 3.2 shows atomic percentage of Al, Si, K and Mo in these two pieces of mica. Atomic percentage of Al and Si are around 16% and 18% respectively on both mica substrates in all areas, suggesting Al and Si on mica are not involved during synthesis process.

In Area A, atomic percentage of K decreases to 0.4%, reveals that K atoms are extracted to K_xMoO_3 nanobundles from mica. Although all products are removed, Mo is detected in this area, indicating Mo-K ion exchange during growth process. For the ion exchanged Mo atoms are below the top surface, they are not sonicated away. In Area B, there is around 1% of potassium. Due to the high diffusion coefficient of K in mica, K atoms diffuse to nearby area (Area A) where K concentration is depleted to support continuous growth of K_xMoO_3 nanobundles. Meanwhile, no Mo is detected and surface of area B is flat. It reveals that synthesis of MoO_3 microbelts by nucleation of MoO_3 vapour does not react with mica surface and they are easily removed without affecting the mica surface. In Area C, the components possess the same atomic percentage as pure mica, suggesting that mica is thermal stable in experiment. The measurement reveals that K atoms are extracted to K_xMoO_3 nanobundles at the position nanobundles grew and the nearby K atoms diffuse to this area for continuous growth.

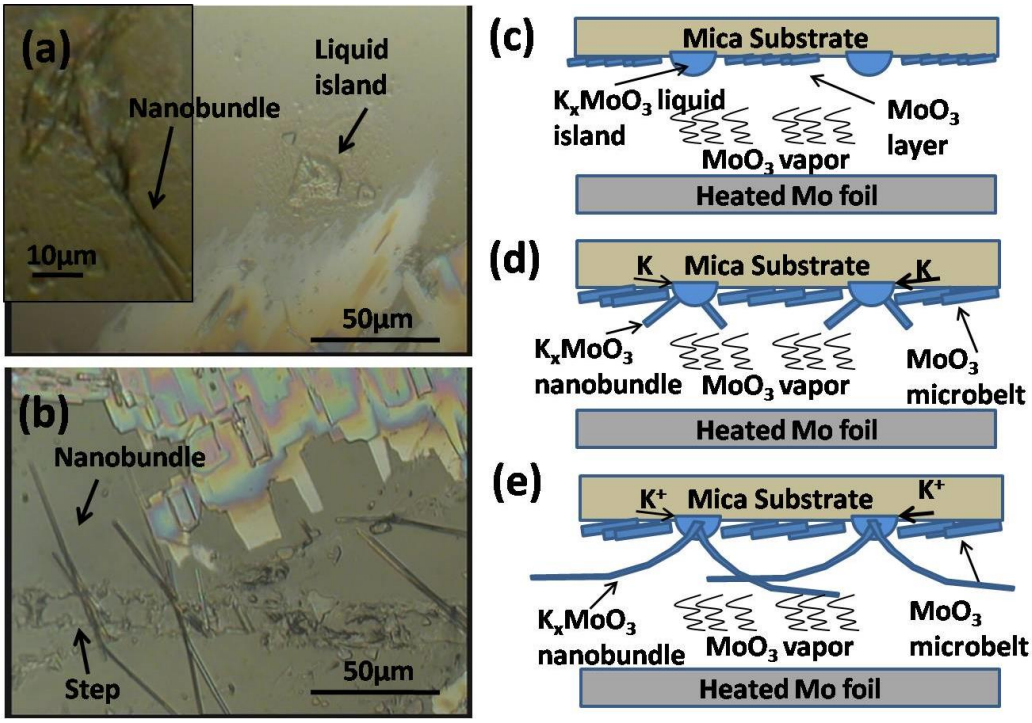

Figure 3.12 (a) Optical microscope image of flat mica surface after growth for 20 min, inset image is the liquid island after 30 min growth (b) Cracked mica surface after 20 min growth (c-e) schematic of growth process of K_xMoO_3 nanobundle.

For further characterizing the way K atoms being absorbed to nanobundle, the mica substrates that used to grow for short duration (20~30 min) are observed to elucidate the growth mechanism of K_xMoO_3 nanobundles. Figure 3.12(a) and (b) shows the different places where K_xMoO_3 nanobundles grow at the beginning. On the flat mica surface, liquid island forms in Figure 3.12(a). After heating for longer duration, nanobundle extends out of the island as shown in inset image of Figure 3.12(a). On the crack surface (Figure 3.12(b)), K_xMoO_3 nanobundles directly grow out of the side of step, where is the cleavage of mica sheet. After long duration, more K_xMoO_3 nanobundles extend out of liquid island or side of steps. Meanwhile, MoO_3 microbelts grow with a layer of MoO_3 on surface first as shown in the colourful part of Figure 3.12(a) and then MoO_3 crystals nucleate on top of it layer by layer without reaction with mica substrate.

According to the EDX measurement of mica substrate after nanobundle synthesis and the morphology of mica surface at the beginning of growth, we propose the following growth mechanism of K_xMoO_3 nanobundle. Figure 3.12(c-e) show the schematic of growth process. Mo is oxidized on Mo foil and vaporizes upwards till it arrives at mica substrate. On the surface of mica, MoO_3 vapour reacts with surface of mica to form liquid islands of K_xMoO_3 and creating channel for ion exchange between K^+ and Mo^{6+}. With the continuous absorption of MoO_3 vapour, K_xMoO_3 becomes oversaturated in the island and K_xMoO_3 nanobundle nucleates out of the island in preferred direction. The growth of K_xMoO_3 nanobundle maintains the low concentration of K^+ in island compared with that in mica sheet. This low concentration further induces the influx of K^+ towards the island continuously. In return, the combination of K^+ and MoO_3 vapour promotes the further growth of K_xMoO_3 nanobundles. While on the side of steps, channels for K atoms to diffuse and intercalate into MoO_3 structure already exist on the cleavage surface according to the laminated structure of mica. Consequently, K_xMoO_3 nanobundle can directly grow out of the steps.

Due to the facility to absorb K atoms from cleavage surface and lower energy required for nanobundles nucleating on steps, K_xMoO_3 nanobundles are widely found on these steps. It provides a method to pattern the growth of K_xMoO_3 nanobundles by designing steps on mica surface. On the other hand, liquid island possesses larger contact area with surrounding mica to extract more K atoms and provides larger area for K_xMoO_3 nanobundle to grow out. Although there are only a few islands forming on mica surface, each island produces great amount of nanobundles, as shown in the Figure 3.2.

For the different growth mechanism of MoO_3 microbelts and K_xMoO_3 nanobundles, the morphology of them differs correspondingly. The bottom-up growth from substrate forces the nanobundles to grow with a strong orientational preference and extend into air. While microbelts produced by nucleation of MoO_3 vapour does not display specific orientation. As Figure 3.2 shows, the length of K_xMoO_3 nanobundles can grow as long as 200~300μm with a width of roughly 700~900 nm, while the length of MoO_3 microbelts is 10~15μm with width around 3~5μm. The corresponding aspect ratios are around 300 and 3 respectively, illustrating the difference in growth mechanism.

3.5 Summary of Results

We have discovered a simple but effective technique to grow K intercalated MoO_3 nanobundles by thermal evaporation method on muscovite mica substrate. With the help of various experimental characterization techniques, we find that the orthorhombic lattice structure and the layered structure remaining essentially intact. Considering the great amount of large size ion insertion (1.5 Å in size and ~0.2 in atomic ratio), the expansion between layers is amazingly small. Density functional theory is used to assist the K_xMoO_3 structural determination. Our results suggest that

the K atoms in the nanobundles most likely occupy the O vacancy sites, allowing the K atoms to be intercalated without incurring large distortion of the MoO_3 layered structure. The absorption of K ions by Mo-K ion exchange in mica substrate and MoO_3 vapour from heated Mo foil promotes the continuous growth of K_xMoO_3 nanobundles. The simple synthesize method opens a new opportunity to develop nano-structured materials of large-ion intercalated metal oxides. It is noted that the preparation method is simple and straightforward. It utilizes the open-ended furnace only and is carried out in ambient and moderate temperature. The simpleness makes the method repeatable in other environment.

Chapter 4 Electrical Conductivity and Photo-Electrical Response

Alkali ion intercalation into structure always deforms the band structure and enhances the electrical conductivity.[3, 43, 60, 61] Considering the great amount of K ions being inserted into MoO_3 nanostructure, the electrical performance of MoO_3 is expected to be greatly enhanced. The electrical property of individual nanobundle is systematically studied, and the theory calculation about the band structure explains the high performance of nanobundle. Significant photon electrical response is observed and the mechanism is discussed as well.

4.1 Electrical Measurement

Electrode Device

To investigate the electrical properties of individual nanobundle, the micro-electrode device is fabricated. Individual nanobundle is transferred from the growth substrate to SiO_2/Si substrate and photolithography method is utilized to achieve designed metal (Au(400 nm)/Cr(10 nm)) finger electrodes (of gap ~10 μm) that make contact with the nanobundle. The process of device fabrication is described in Chapter 2 in detail.

The SEM image of individual nanobundle electrode device is displayed in Figure 4.1(a). Four Au finger electrodes with 10 μm width cover on 70 μm length individual nanobundle, and a ~10 μm gap exists between every two electrodes. Figure 4.1(b) displays the schematic side view of the device. On the Si substrate, the 100 nm SiO_2 layer acts as insulator to avoid current leaking through Si substrate. The individual

nanobundle is placed on the substrate and Au electrodes cover on the nanobundle. The electrode is further soldered with copper wire and connected to Keithley 6430 source-measure unit for electrical measurement. Besides the photolithography method, Electron Beam Lithography (EBL) method can be utilized to design even smaller pattern on the substrate. Figure 4.1(c) displays the electrodes with width of 4µm and separation of 5µm written by EBL method. Figure 4.1(d) shows the side view of nanobundle electrode device with metal electrode covers on the nanobundle both on the top and two sides.

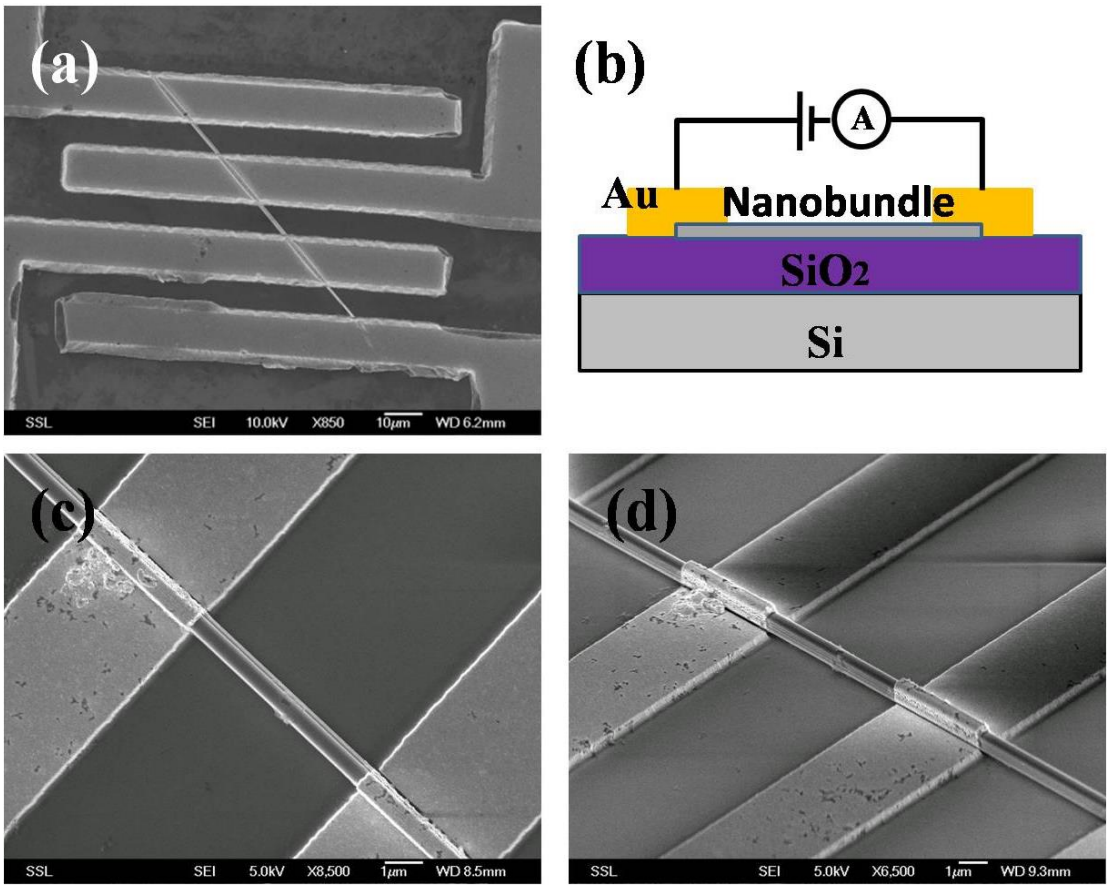

Figure 4.1 (a) SEM image of individual nanobundle electrode device (b) Schematic image of the side view of device for electrical measurement. (c) Zoom in image of the gap between electrodes (d) Side view of electrodes.

Electrical Conductivity at Room Temperature

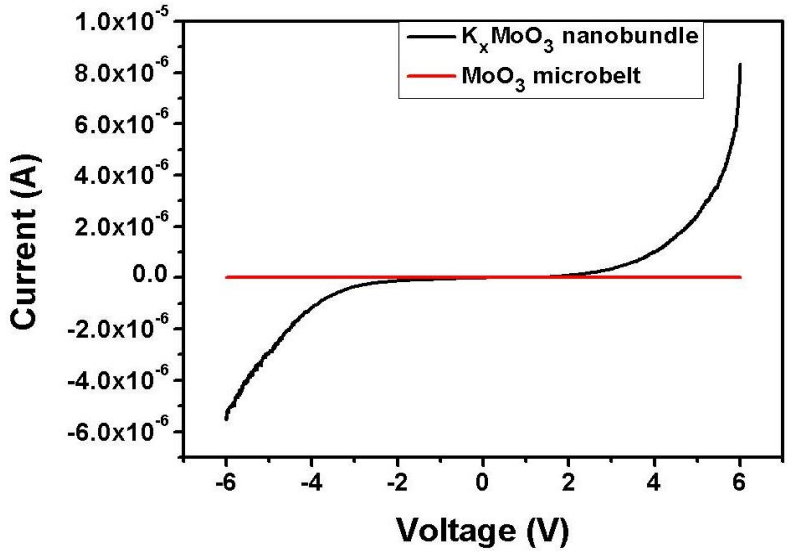

Figure 4.2 I-V curves of K_xMoO_3 nanobundle and MoO_3 microbelt.

The K_xMoO_3 nanobundle device and MoO_3 microbelt device are fabricated, and the electrical measurement on both devices are carried out subsequently. Figure 4.2 displays the measured IV curves for the two materials. For the MoO_3 microbelt (red curve in Figure 4.2), the measured current is on the order of ca. 1 *p*A at ca. 5 V. From the measured effective length and cross section of this material, we estimate the electric conductivity of the MoO_3 microbelt to be ca. 10^{-6} S m^{-1}, consistent with the reported value of the MoO_3 nanobelts.[43] For the K_xMoO_3 nanobundles (black curve in Figure 4.2), at room temperature, the measured current is 6.64 μA at a bias of 5 V and the I-V curve displays typical semiconductor-like behaviour. It is remarkable that the electric conductivity is enhanced substantially by seven orders of magnitude from 10^{-6} S m^{-1} of the MoO_3 microbelts to 24 S m^{-1} for K_xMoO_3 nanobundle. The magnitude is also three orders higher than that of the lithiated MoO_3 bulk ($Li_{0.25}MoO_3$ 3.1×10^{-2} S m^{-1})[61] and five orders higher than that of lithiated MoO_3 nanobelt (10^{-4} S m^{-1})[43]. With same voltage amplitude, the magnitude of current may differ when polarity changes. As Figure 4.2 shows, the current is 8.5 μA at +6 V, while it becomes -5.6 μA at -6 V. The changed conductivity is possibly due to the different contact property between metal electrode and nanobundle. We have tested over twenty samples. The conductivity

varies a bit between different samples, but the order of values and the IV trend is the same. Considering the symmetric IV behaviour in both positive and negative voltage, and the repeatable electrical property in all samples, we excludes the possibility that non-linear behavior comes from Shottky barrier, which is non-symmetric and could not always be observed with similar conductivity values. Consequently, we believe that the electrical properties originate from nanobundle itself, instead of metal-semiconductor junction.

Temperature Dependent Electrical Conductivity

To study the temperature effect on the conductivity, the device is mounted on the heating stage to systematically control the temperature of nanobundle. The inset schematic image in Figure 4.3 displays the set up. The conductivity of the K_xMoO_3 nanobundles increases rapidly upon heating as shown in Figure 4.3. At the bias of 5 V, the current increases from 6.64 μA to 0.15 mA as the temperature increases from 23 °C to 142 °C, raising the conductivity from 24 S m^{-1} to 530 S m^{-1}. The significant thermal enhanced conductivity suggests great amount of electrons are excited by thermal energy, and it indicates the small band gap of the nanobundle.

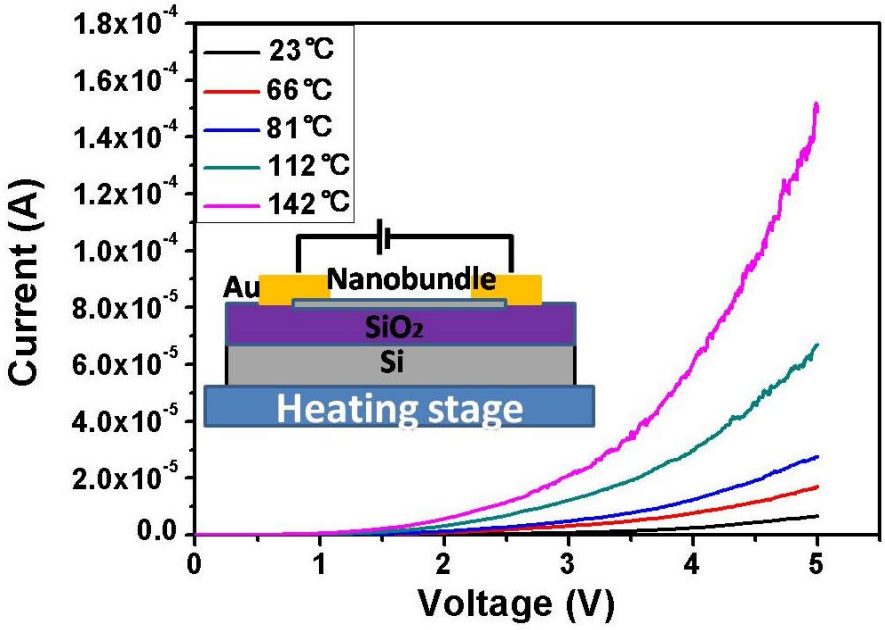

Figure 4.3 I-V curves of K_xMoO_3 nanobundle at different temperatures. Inset image shows the set up.

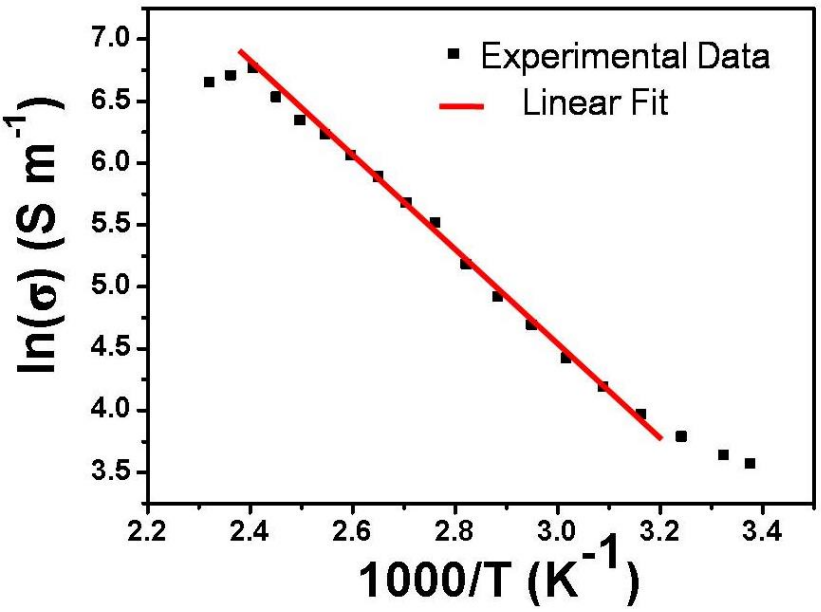

Figure 4.4 Temperature dependence conductivity of the nanobundle in log scale at voltage of 4 V.

Subsequently, the conductivity at the voltage of 4 V as a function of reciprocal of temperature is plotted on a log scale as shown in Figure 4.4. Two kinks in the curve are clearly observed at 310 K and 410 K. At the temperature below 310 K, log scale of conductivity changes in smaller slope, and the slope gradually increases as temperature rises. As temperature increases from 310 K to 410 K, the log scale of conductivity varies linearly with reciprocal of temperature. In this region, electrical conductivity increases exponentially with reciprocal of temperature. According to $\sigma=ne\mu$, where σ is the conductivity of nanobundle, μ is the mobility of electrons, n is the electron density, the mobility in the region does not vary significantly due to relatively low electron density, the electron conductivity is thus determined by electron density. Moreover, the significantly increased conductivity (jumps 20 times higher by raising the temperature from 25 °C to 140 °C) suggests the effusion of excited electrons. The variation of σ with temperature in this linear range thus can be attributed to the change of electron density with temperature. Base on the thermally activated transport model,[62, 63]

$$\ln(n) = \ln(n_0) - \mathrm{W}/2\mathrm{kT}$$

where n is the electron density, n_0 is the density value when T is infinity, k is the Boltzmann constant and W is the thermal activation energy. The thermal activation energy is determined to be around 0.5 eV based on the slope of the linear fit to the data (Figure 4.4). The value suggests the energy required to thermally excite localized electrons to conduction band. The effect of phonon scattering increases for thermally excited lattice atoms and the effect becomes more prominent at high temperature due to sufficient high electron density. Consequently, above 410 K, the conductivity decreases due to the decreasing mobility induced by significant phonon scattering.

Electron Mobility

Field Effect Transistor (FET) uses an electric field to control the conductivity of a channel of charge carriers in semiconductor material. By the way conductivity changes with gate voltage, the type of charge carriers could be identified, and the mobility of these carriers in the semiconductor material can be measured.

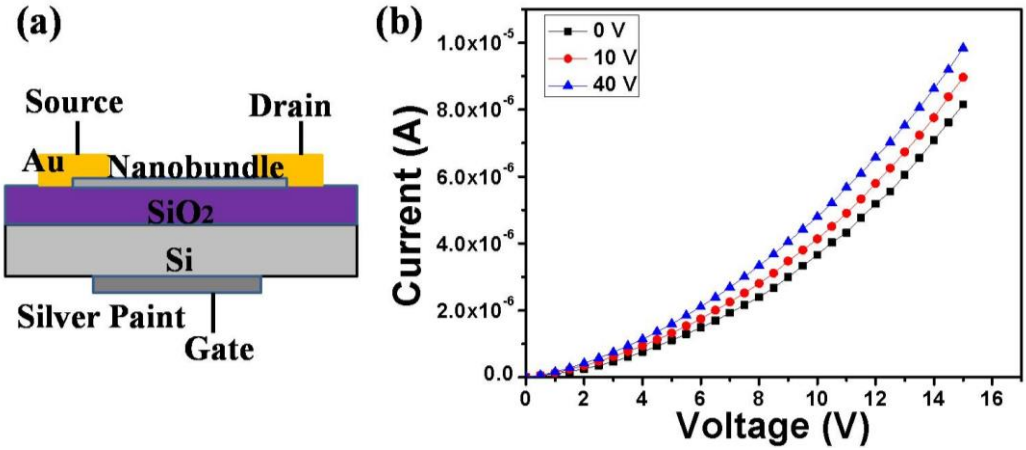

Figure 4.5 (a) Schematic setup of FET device (b) Current (I_{sd}) versus source drain voltage (V_{sd}) curves recorded at different gate voltages (0, +10 V and +40 V) for the device shown in (a).

For FET measurement, the nanobundle device is further treated. The bottom of the device is scratched to remove the SiO_2 layer, and silver paint is plastered on the bottom of it. Gate voltage is applied from the bottom and the surface electrodes act as source and drain (Figure 4.5(a)). The current between source and drain I_{sd} versus source drain voltage V_{sd} at different gate voltage is displayed in Figure 4.5(b). Clearly that I_{sd}

increases as gate voltage increases. The performance denotes the K_xMoO_3 nanobundles exhibit n-type semiconductor behaviour with electrons as charge carriers.

The mobility of nanobundle device can be estimated using[64]

$$\frac{dI_{sd}}{dV_G} = \frac{\mu C}{L^2}$$

where μ is the carrier mobility, C is the capacitance of the device, L is the active nanobundle length between the electrodes. The capacitance is given by

$$C = \frac{2\pi\epsilon_0\epsilon_{SiO_2}L}{\ln\left(\frac{4h}{d}\right)}$$

in which h is the thickness of SiO_2, d is the diameter of nanobundle, ε_{SiO2} is the dielectric constant of the gate SiO_2, ε_0 is the vacuum permittivity. The calculated electron mobility in K_xMoO_3 nanobundle is ~10 cm^2/ VS. The value is similar with the magnitude measured in ZnO nanowire FET.[64]

4.2 Band Structure Analysis

The electronic structure of MoO_3 is well understood and the compound is an *n*-type semiconductor with a band gap of 3.3 eV.[65] Little amount of electrons could be excited to conduction band for the large band gap. It results in the extremely low conductivity of MoO_3 as measurements displaying above. In MoO_3, the valence band is largely dominated by the *2p* orbitals of oxygen, while the conduction band consists of chiefly the *4d* states of molybdenum with a significant contribution from the *2p* states of oxygen.[65]

To understand the significantly enhanced conductivity of K_xMoO_3 nanobundle, we perform Bader charge analysis[66] and calculate the band structure of K_xMoO_3 nanobundles in which K atoms act as occupants at oxygen vacancies. Upon potassium uptake in the lattice, however, the electronic structure undergoes a substantial change

due to the charge transfer from potassium to molybdenum, which forces electrons to populate in the conduction band. This is clearly seen in the calculated band structure of the K_xMoO_3 lattice depicted in Figure 4.6. The projected density of states (PDOS) for the K-*4s* and Mo-*4d* states indicates that the electrons from the K atoms are fully transferred to the adjacent Mo atoms. This results in the reduction of the adjacent Mo atoms. The prediction is confirmed by the XPS experiment displayed in Chapter 3. The ion insertion reduces the average valence of Mo atoms from +6 to +5.4.

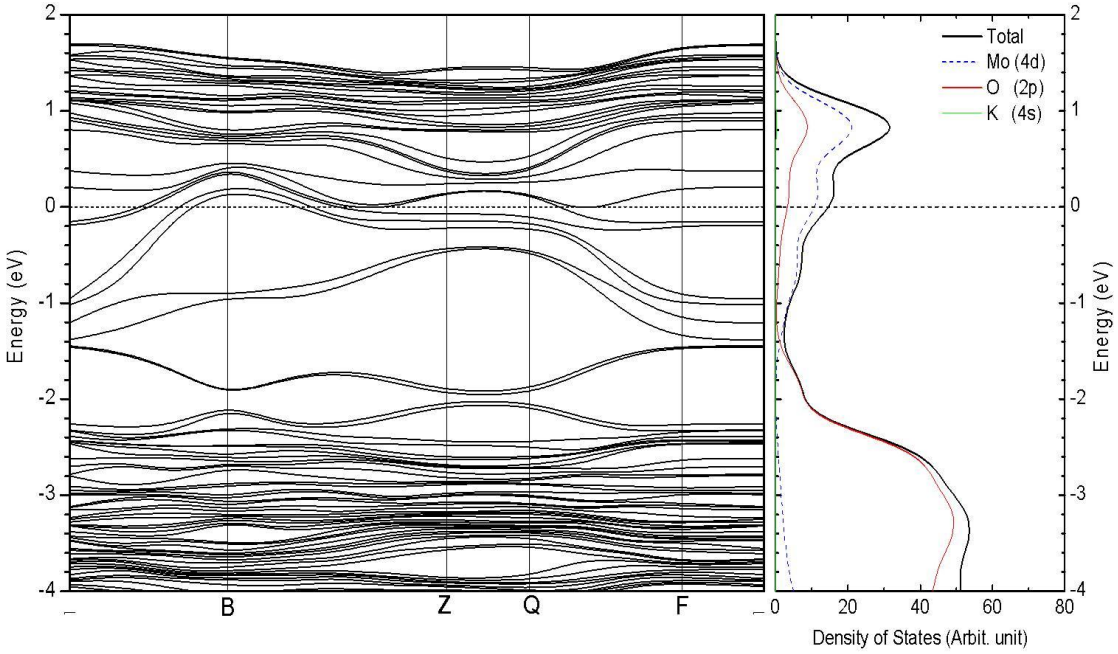

Figure 4.6 Calculated Band structure and the Density of States (DOS) of K_xMoO_3 Nanobundle.

Because of the strong overlap between the Mo-*4d* orbitals and the O-*2p* orbitals in the conduction band, the transferred electrons are populated and readily delocalized. The electric conductivity is thus significantly enhanced. Therefore, the conductivity enhancement arises solely from the reduced Mo atoms, which are aligned in the [001] direction as shown in inset image in Figure 4.7. Electric conductivity along these rows thus reaches its maximum. Indeed, the calculated band structure displays wide bands across the Fermi level from G→B and Q→F. The energy bands in other directions, particularly those along the [010] direction, are much narrower due to the high oxidation states of the Mo atoms away from the K atoms. Compared with Li, the ionization potential of K is much lower and thus the adjacent Mo is more readily

reduced. This explains nicely the much higher observed electric conductivity of K_xMoO_3 than that of Li_xMoO_3. We further note that the K_xMoO_3 nanobundle crystalline grows along the [001] direction, in which the voltage is also applied in our I-V curve measurement. From the calculated band structure of $K_{0.25}MoO_{2.75}$, electric conductivity along the rows highlighted in Figure 4.7 is the highest. However, even in the [001] direction, the rows in which the Mo atoms remain in the high oxidation states are still semi-conducting due to lack of electron occupation in the conduction band. It therefore requires energy to shift electrons from the valence band to the conduction band to gain good conductivity. This explains the semiconductor-like behaviour of the nanobundles observed in our I-V curve measurement and indicates the energy (0.5 eV) required for thermal activation.

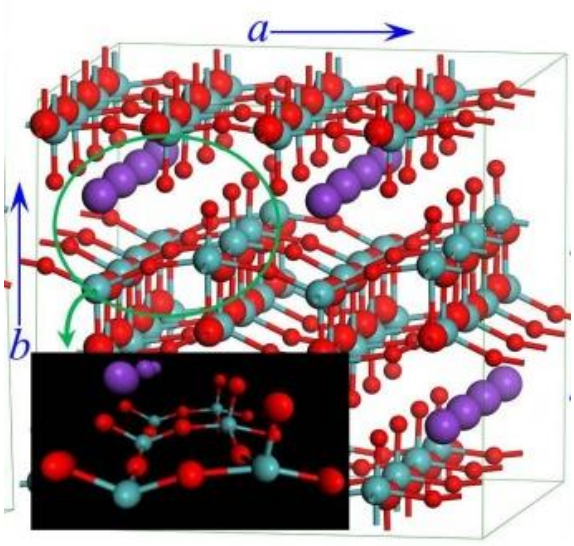

Figure 4.7 Simulated Lattice Structure of K_xMoO_3 nanobundle, inset image display the flow path of electrons, where reduced Mo atoms align. Red balls represent O atoms, blue balls represent Mo atoms and purple ones represent K atoms.

4.3 Photoelectrical Response Measurement

Due to the wide bandgap (3.3 eV) and low conductivity, MoO_3 is not known to be electrical responsive to photon excitation. However, with enriched K intercalation in the structure, the situation changes. The ionization of the K atoms gives rise to the reduction of the adjacent Mo atoms, leading to higher electron population in the

conduction band and consequently enhances the conductivity of the K enriched MoO_3 by seven orders. Although the precise band gap value of the individual nanobundle is not measured, both experimental measurements and theoretical calculation show the band gap of the material to be quite small. The small band gap of the material implies that only a small amount of energy is required to excite the localized electrons. Hence, these attributes make this nanobundle a viable candidate for the investigation of photoelectrical response.

Nanostructured materials have been extensively studied and applied as nanoscale photonic and electronic devices, like optoelectronics, photovoltaics, photodetectors and sensors.[67-71] To probe their opto-electrical properties, photoelectrical response of individual nanowires is widely studied.[70] Due to the commonly adopted broad beam illumination on these nanowires based devices, the observed photoelectrical response depends on the interplay between the intrinsic response of the nanomaterials and nanomaterial-electrode contact barriers.[72-75] In order to evaluate the efficiency of photovoltaic device made of these nanomaterials, it is necessary to elucidate the intrinsic characteristics of these nanomaterials. Hence, photoelectrical response measurements under focused laser beam irradiation are utilized.[76-81]

In the following part of this chapter, we will display the photon induced voltage/current generated from single K_xMoO_3 nanobundle under localized focused laser illumination without externally applied voltage bias. Unlike the previous reports that photon induced voltage was generated from metal-semiconductor junction or PN junction in hybrid nanomaterial,[72, 73, 76, 78, 82] the significant photo induced voltage (36.5 mV) is produced from nanobundle itself with controllable polarity and amplitude by varying the location of focused laser spot irradiation. The measurement of photon enhanced current with externally applied voltage bias is studied as well to further demonstrates the electron excitation phenomenon in the nanobundle.

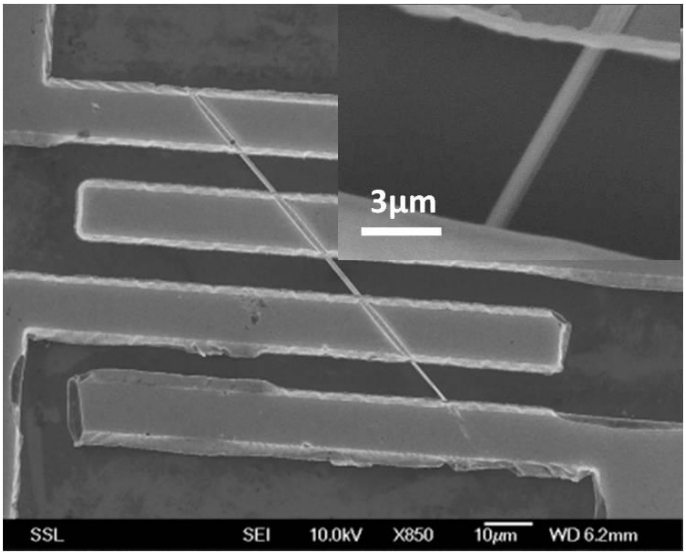

Figure 4.8 SEM image of the K_xMoO_3 nanobundle contacted with metal electrodes. Inset shows zoom in image of middle segment of nanobundle between two electrodes.

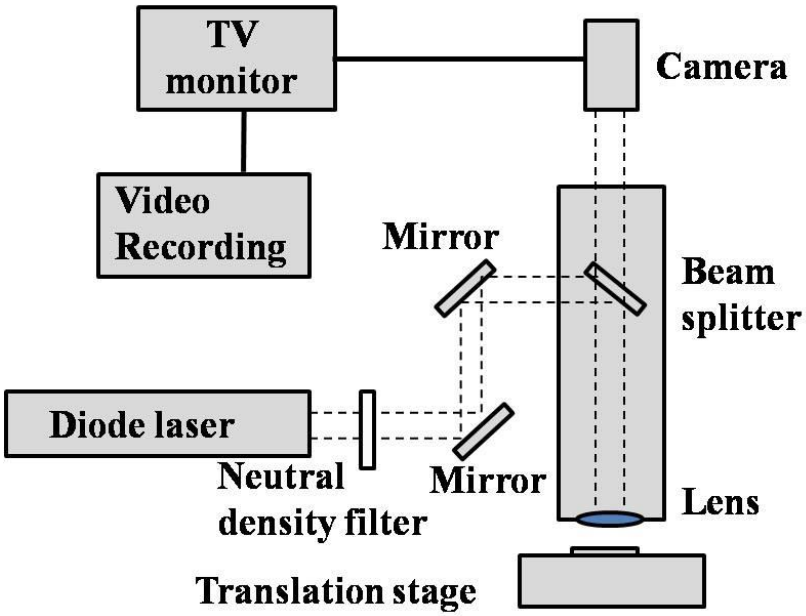

Figure 4.9 Schematic of photon response measurement set-up with focused laser beam radiation on K_xMoO_3 nanobundle.

The individual K_xMoO_3 nanobundle device is fabricated in the process described above. The individual K_xMoO_3 nanobundle is transferred to Si substrate with a 100 nm SiO_2 layer. Patterned electrodes of 10 nm Cr and 500 nm Au are fabricated via standard photo lithography and sputtering of metals. A scanning electron microscopy (SEM) image of single K_xMoO_3 nanobundle device is shown in Figure 4.8. Inset shows the

width of the nanobundle is about 1 μm and the separation between the electrodes is 10 μm. Figure 4.9 shows the schematic of the photon response measurement set-up with focused laser beam irradiation on K_xMoO_3 nanobundle electrode device. The red laser beam (λ=660 nm) is directed into the microscope via two mirrors and reflected by a beam splitter towards the objective lens. The 50× objective lens focuses the laser beam onto the device positioned on the translation stage. The alignment of set ups are described in detail in Chapter 2.

4.4 Photon induced Electrical Response Measurement

Localized Focus Laser Illumination induced Electrical Response

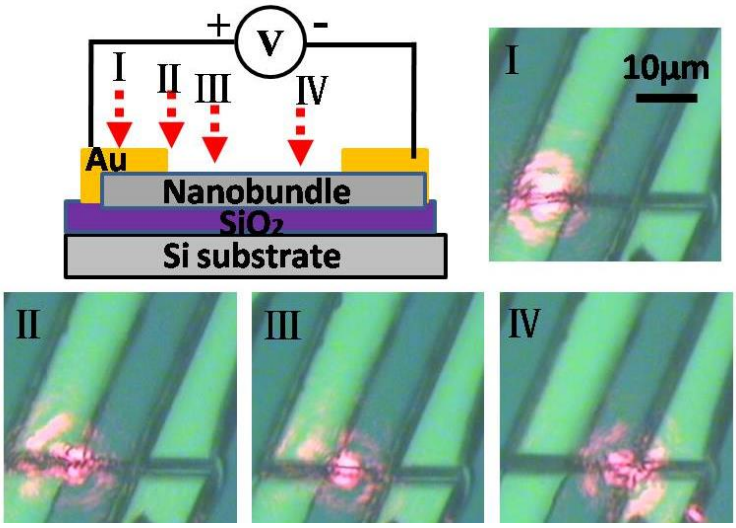

Figure 4.10 Schematic of focused laser beam locally irradiating at four different locations and four optical images showing the position of laser spot on K_xMoO_3 nanobundle device.

Focused laser beam with spot size around 6 μm and power 2.2 mW is locally directed at specific locations as shown in Figure 4.10. Considering the Gaussian beam profile of the focused laser beam, the energy is centred within the width of the Gaussian beam. The ring surrounding the centre spot (as shown in Figure 4.10) is attributed to diffraction effect and it does not contribute any significant photon electrical response to the measurement since the beam energy in this ring is rather small. In location Ⅰ, laser is mainly focused on electrode. In location Ⅱ, the spot lands on the metal

semiconductor junction, half on nanobundle and half on electrode. In location Ⅲ and Ⅳ, laser is fully on the left end and right end of nanobundle respectively.

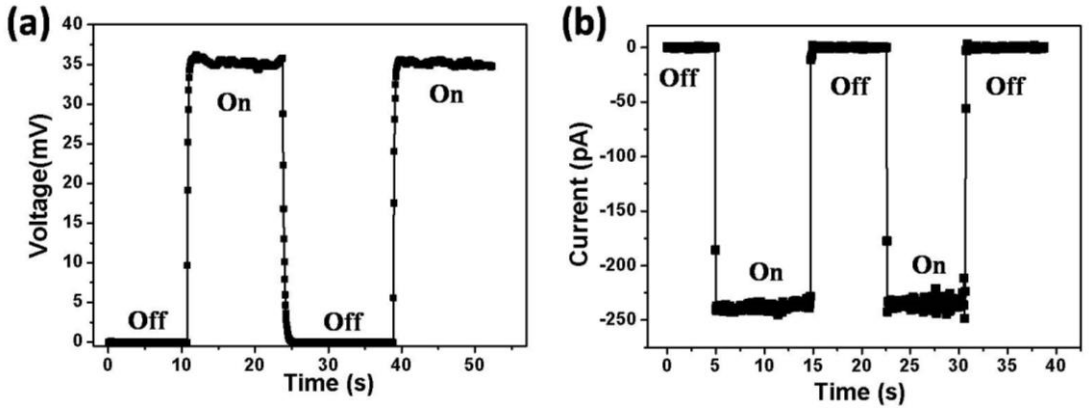

Figure 4.11 Laser spot is directed on location Ⅳ, photon induced voltage and current are measured without externally applied bias voltage respectively in (a) and (b).

Figure 4.11 displays the measured voltage and current between electrodes when laser is directed at location Ⅳ without externally applied voltage bias. As Figure 4.11(a) shows, in the absence of laser beam irradiation, there is no voltage detected. The moment laser is present, voltage increase to 36 mV within 0.4 s. The voltage drops to 0 again when laser is blocked. Since the nanobundle acts as energy source during the electrical measurement, the measured current of circuit is in opposite polarity of measured voltage of the nanobundle. The measured photon induced current at same laser spot location is thus negative as shown in Figure 4.11(b). The moment laser is present, current increases to -240 pA in ~0.05 s. The short response time shows that the photon excited electrons are unlikely to originate from thermal effect, which requires long duration to achieve maximum current.[78] It should be noted that significant voltage (36.5 mV) and current (240 pA) are produced under low laser power (2.2 mW) from individual nanobundle.

Location Dependence of Photon induced Electrical Response

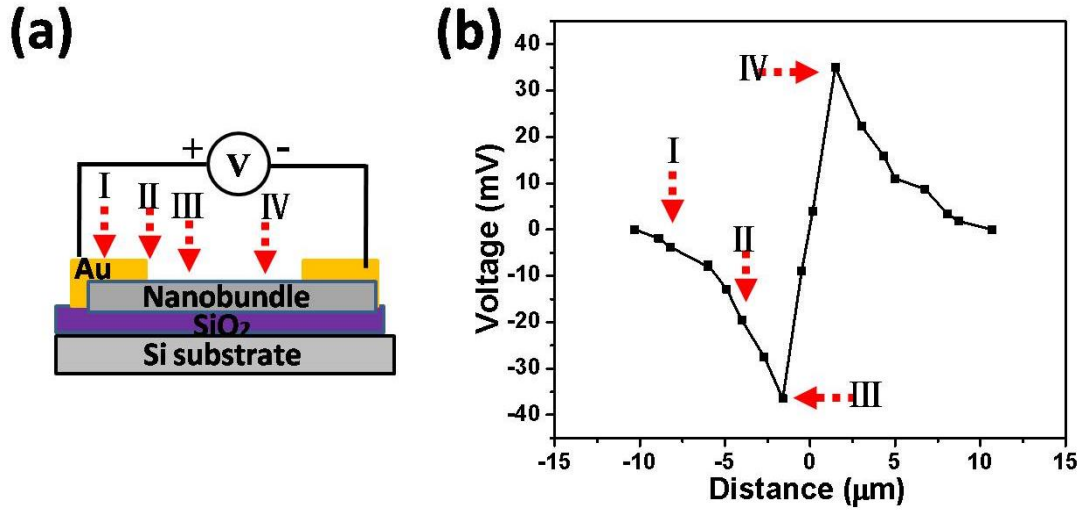

Figure 4.12 (a) Schematic of location dependence measurement process (b) Photon induced voltage at different distance between center of laser spot and center of nanobundle.

Focused laser beam is directed at different locations and the corresponding photon induced voltage is measured as shown in Figure 4.12(b). The distance indicated in the horizontal axis is measured with respect to the center of the nanobundle. When focused laser is fully shone on the electrode or on the substrate, there is no photon induced voltage produced. When part of laser spot is shone on nanobundle, photon induced voltage is detected. With a thick gold layer (500 nm) covering on top of nanobundle, red laser could not penetrate. Thus, only the segment of nanobundle that is directly exposed to laser contributing photon induced voltage. With larger area exposed to laser spot, higher amplitude of voltage is achieved. Compare the measurement at location Ⅰ, Ⅱ and Ⅲ, when exposed area gradually reaches maximum, the amplitude of voltage increases with values of -3.8 mV, -19.5 mV and -36.5 mV respectively. In the reported photon induced current that originated from metal-semiconductor junction, the center of focused laser should land on the junction.[79-81] A small movement from the junction would lead to significant drop of photon induced current. While in our case, the maximum current appears on the end of nanobundle with the whole laser spot lands on the nanostructure. The voltage amplitude on the junction is half of the maximum value, due to the half efficient area that expose to nanobundle. It shows that in K_xMoO_3

nanobundle device the photon induced voltage originates from nanobundle itself instead of nanowire-electrode junction.

When the same area of the nanobundle is exposed to laser, the photon induced voltage produced by nanobundle is controlled by the location of laser spot. With focused laser spot gradually moves from location Ⅲ to location Ⅳ (left end of nanobundle to right end of it), the amplitude of voltage decreases first and the polarity reverses when laser spot passes through the middle of nanobundle. Then, the amplitude of voltage increases and achieves maximum value at location Ⅳ (+36 mV). The observation is reproducible for another three nanobundle devices prepared in the same way. In addition, similar phenomenon is observed when another laser (λ= 532 nm) is used.

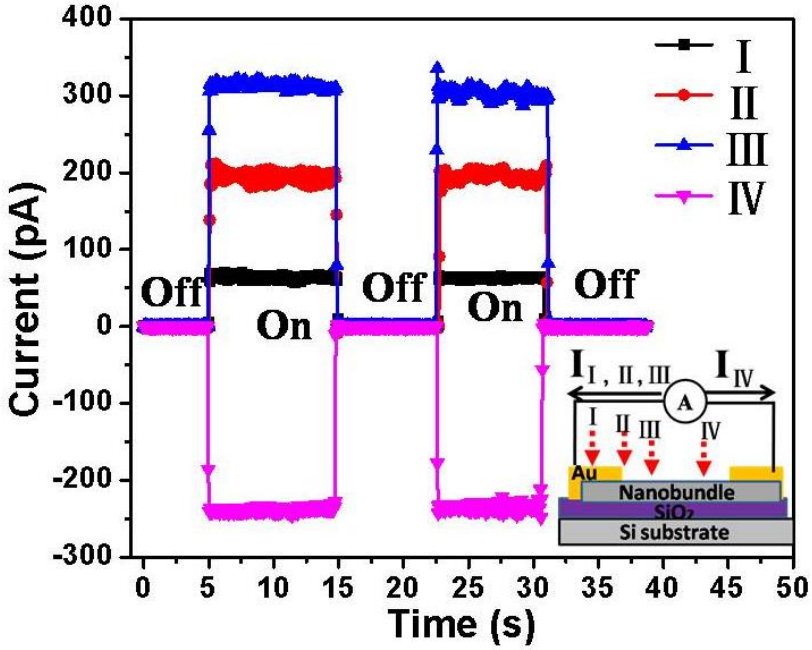

Figure 4.13 Photon induced current measured when laser spot is directed at four different locations without externally applied bias voltage. Inset schematic image displays the measurement set up.

Photon induced current upon different laser locations are measured as well. Figure 4.13 shows the measured current when laser is directed at four locations without external bias voltage. The laser induced current are proportional to the laser induced voltage but in opposite polarity as nanobundle device acts as source. Same with photon

induced voltage, similar laser spot location dependence is observed. With the increasing area exposed to laser spot, current increases as shown by the measurement at location Ⅰ, Ⅱ and Ⅲ with value 70 pA, 190 pA and 320 pA respectively (Figure 4.13). The polarity of photon induced current reverse as the laser spot passes through the middle of nanobundle, and the amplitude reaches maximum when laser spot is directed on the right end of nanobundle with the value of -250 pA. At all locations, current achieved maximum within 0.05 s. The duration is shorter than the period for photon induced voltage reaching maximum (0.4 s), denoting the difference in these two measurement processes.

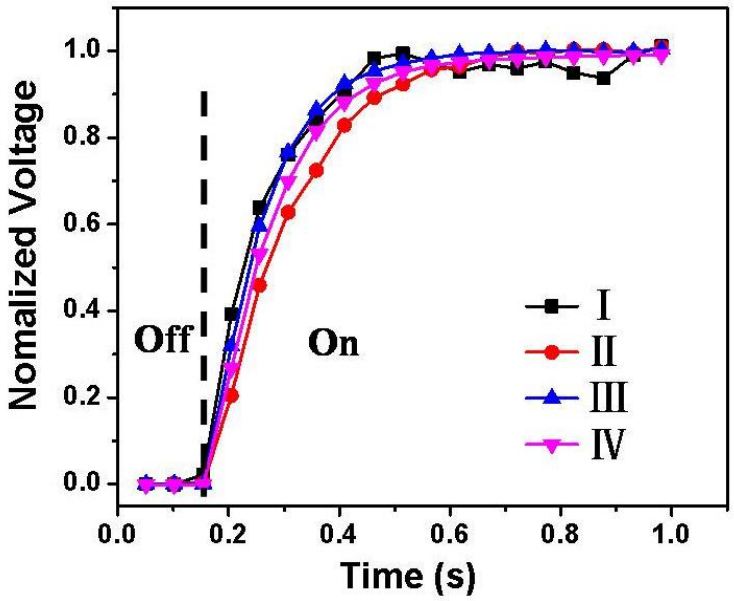

Figure 4.14 Normalized photon induced voltage at the moment laser is present at four different locations.

To further examine the relative long duration required for photon induced voltage reaching maximum, the change of measured voltage is carefully examined at the moment laser is present. Since the polarity and amplitude of photo induced voltage are different at various locations, normalized voltage as a function of time at the moment laser is present is displayed in Figure 4.14. In these experiments, the resolution of the detection is 50 ms and the time to expose the laser is manually controlled, consequently, the exposure time of the first data point at the onset of laser beam dispersed randomly within the 50 ms. Comparison between scenario (Ⅰ) and scenario

(Ⅱ) shows a lag less than 50 ms in scenario (Ⅱ), we believe that it is due to the smaller exposure time in the first 50 ms. At four locations, 0.4 s is required for photon induced voltage to reach equilibrium and the exponential fitting of four curves reveal that the exponential time constant are similar with value around 0.11~0.13 s. The similar voltage increasing pattern and same duration needed to attain maximum voltage at all locations illustrate that diffusion time of electrons does not contribute significantly to the effect. Moreover, the short duration (~0.05 s) required for photon induced current reaching maximum as shown in Figure 4.13 excludes the possibility of electron excitation time. Thus, these results suggest that the time required for photon induced voltage to achieve maximum corresponds to the time required to build up voltage near terminal instead of the time required to excite electrons or the diffusion time of electrons.

Laser Power Dependence of Photon induced Electrical Response

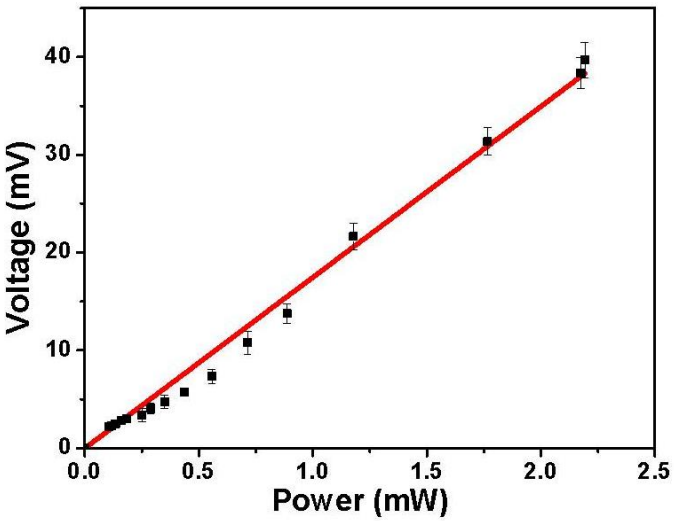

Figure 4.15 Photon induced voltage under different laser power when laser is directed at location Ⅳ.

Neutral density filter is placed in the optical train to change the laser power and focused laser is directed at location Ⅳ. Figure 4.15 shows the measured photon induced voltage when exposed to laser with different power. It shows that at same location, photon induced voltage linearly increases with laser power, but a small non-linear

effect at low laser power is observed. The non-linear effect is contributed by the nanobundle configuration – nanobundle is packed by many parallel nanobelts. Under low laser power, light is not strong enough to penetrate through nanobundle and only excites part of nanobelts. When laser power increases, the amount of excited electrons in already excited nanobelts linearly increases with laser power and there are new contributions from nanobelts in the bottom of nanobundle as they are being excited as well. The combined effect makes photon induced voltage displays small non-linear behavior at low laser power. While in high laser power situation, the nanobundle is already penetrated by laser, thus, the photon induced voltage linearly increases with laser power in high power region.

Mechanism of Photon induced electrical response

According to the observation, we propose the following mechanism for the observed photon induced electrical response. Due to the small band gap of K_xMoO_3, localized electrons and holes are easily created in nanobundle when exposed to laser. The concentration of these charge carriers reaches its maximum in the location where the intensity of light is strongest. Subsequently, the possible processes that follow the creation of these charge carriers include charge recombination, diffusion of the charge carriers and scattering of the charge carriers. Although one expects significant contribution from the charge recombination, some of the charge carriers can diffuse to both electrodes under the influence of mutual repelling force especially in the event of the presence of high concentration of charge carriers. Consequently, if the electrode is far away from the position of laser spot, the amount of excited charge carriers reaching the electrode is low. Thus, at location Ⅰ, Ⅱ and Ⅲ, more charge carriers arrive at left electrode than right electrode due to the shorter distance from center of laser spot to left electrode. As the net charge carriers that reach left terminal result in positive current as shown in Figure 4.13, we attribute the charge carriers to be the electrons considering its higher mobility in lattice and the higher electron concentration in n-type semiconductor. At location Ⅳ, electrons are excited at right part of nanobundle,

significant amount of net electrons reach right electrode. Consequently, the measured photon induced current shows opposite polarity when focused laser is directed at two end of nanobundle. When the laser beam is focused at the middle of nanobundle, due to the equal distance from both electrodes, similar amount of photon excited charge carriers is expected to reach the two electrodes at both ends of the nanobundle. Hence there is no net current detected.

The diffusion ability of electrons in the nanobundle is concluded from electrical measurement. The mobility of electrons μ is measured by FET configuration described above and the value is ~10 cm^2/V s. The diffusion length of the charge carrier can be estimated by

$$L = \sqrt{D\tau}$$

where D is the diffusion coefficient (D=μkT/e) and τ is the life time of the charge carrier. The lifetime of the photon excited electrons in semiconductor nanowire is normally in the time scale of microseconds to milliseconds.[83] Consequently, the diffusion length is estimated to have a minimum value of ~5 μm. Moreover, the conductivity of the nanobundle increases from 24 to 530 S m^{-1} when temperature increases from 23 to 142 ^oC. Thus, the increased temperature induced from localized laser illumination would further increases the diffusion length of excited electrons. Considering the long diffusion length, it is plausible that diffusing charge carriers to find their way towards the electrodes that are in contact with both ends of the nanobundle.

During voltage measurement, excited electrons reach an electrode and accumulate at the electrode due to extreme high resistance of voltmeter. At location Ⅰ, Ⅱ and Ⅲ, net accumulated electrons near left electrode introduce negative voltage while accumulated electrons near right electrode introduce positive voltage at location Ⅳ. Accumulated electrons repel further influx of excited electrons under Coulomb's interaction and consequently the increase in voltage slows down time as shown in

Figure 4.14. After certain duration, the repulsive force originated from accumulated electrons near electrode and excited electrons in the center of laser spot equilibrates. The distribution of excited electrons achieves equilibrium, thus, photon induced voltage achieves equilibrium and remain constant. The process explains the relative longer duration (0.4 s) required to achieve maximum photon induced voltage than that of photon induced current (0.05 s). The study about duration required to build up voltage in nanoscale device is not reported before. It is possible that in conventional photocurrent report, photon response originates from Schottky barrier of metal semiconductor junction and peak concentration of excited electrons locates at junction,[73, 79-81, 84] in which case the voltage builds up rapidly.

4.5 Photon enhanced Electrical Response Measurement

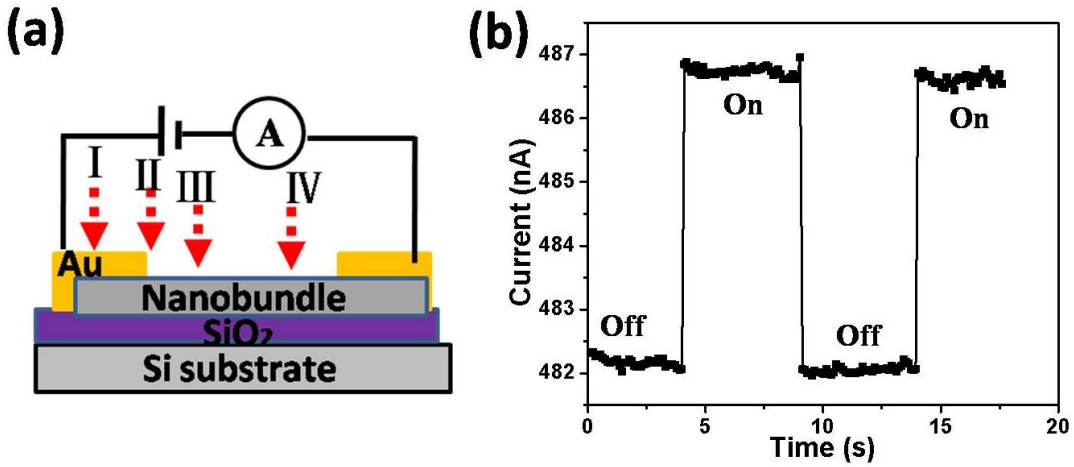

Figure 4.16 (a) Schematic of focused laser beam locally irradiated at four different locations under external bias (b) Photocurrent measured under external bias voltage of 0.4 V with laser spot directed at location III on K_xMoO_3 nanobundle device.

Similar systematic research is carried out with external bias voltage on the individual nanobundle device. When external bias voltage is applied, photon excited electrons are driven to terminal by the applied electric field and thus current is enhanced. Figure 4.16(a) shows the schematic measurement setup. External bias voltage is applied between electrodes and an ammeter is used to measure the flowing current. Focused laser is locally shone on the nanobundle and the change of current is

recorded. Figure 4.16(b) displays the measured current between electrodes when laser is shone at location Ⅲ with external bias voltage of 0.4 V applied. When laser is blocked, current induced from external bias is around 482.1 nA. The moment laser is on, current increases to 486.6 nA in less than 0.05 s. The current dropped to 482.1 nA again when laser is off. The short response time suggests that excited electrons originated from photon excitation instead of thermal effect.

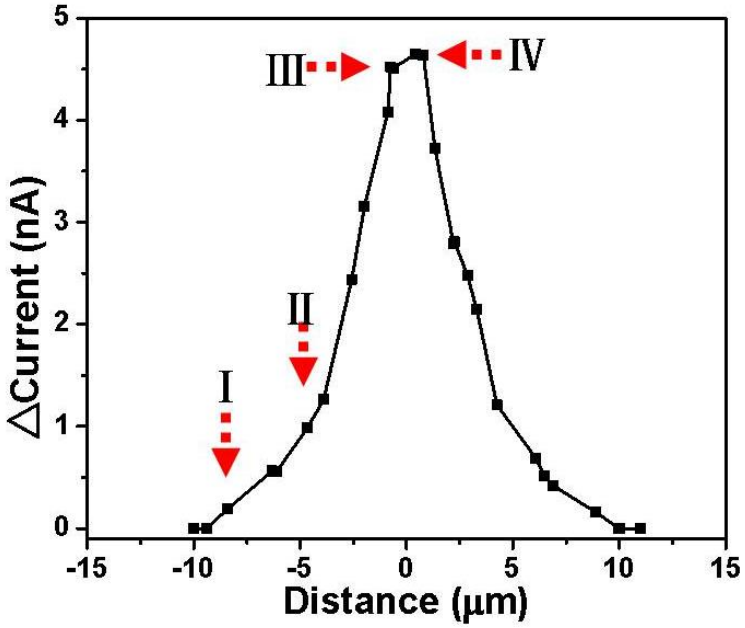

Figure 4.17 The Photon enhanced current at different distance between center of laser spot and center of nanobundle.

Focused laser is directed at different locations as shown in Figure 4.16 (a), the distance is measured with respect to the center of nanobundle and the corresponding photon enhanced current under external bias voltage of 0.4 V is detected as shown in Figure 4.17. When focused laser is fully shone on the electrode or on the substrate, there is no photon enhanced current observed. When part of laser spot is shone on nanobundle, photon enhanced current is detected, and with larger area exposed to laser spot, higher amplitude of enhanced current is achieved. Compare the measurement at location Ⅰ, Ⅱ and Ⅲ, with exposed area gradually reaching maximum, the photon enhanced current increases with value 0.2 nA, 1.0 nA and 4.5 nA respectively. When the same area of the nanobundle is exposed to laser, e.g. at location Ⅲ and Ⅳ, the

photon enhanced currents are almost the same. It is because that under external bias, majority of photon excited charge carriers are driven to the electrode under the applied electric field. With similar amount of charge carriers excited by laser spot, the amplitudes of enhanced current are almost the same. The observation that maximum enhanced current appears when laser spot is fully on the nanobundle and the same photon enhanced current at all locations with same exposure area suggest that photon excited electrons originated from nanobundle itself, consistent with the performance in photon induced electrical response measurement.

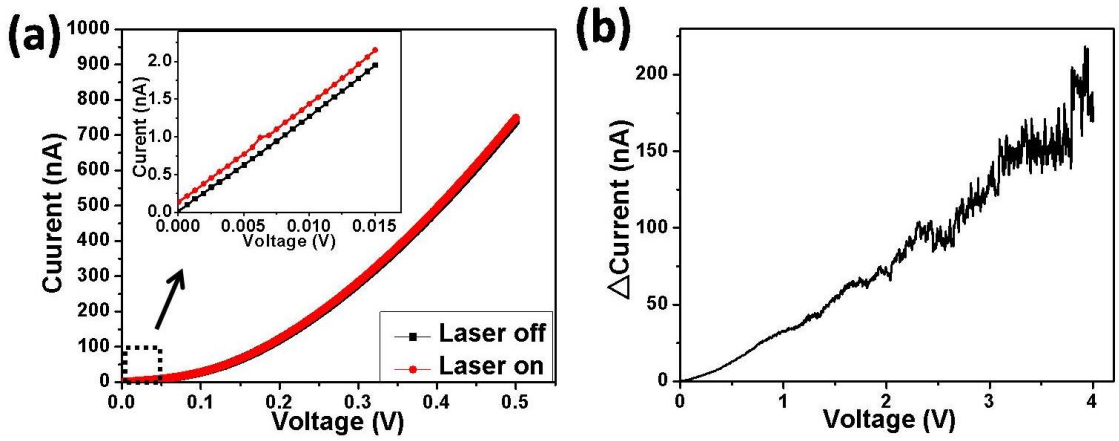

Figure 4.18 (a) Typical I-V characteristics of nanobundle with and without laser spot shown at location III respectively. Inset curve shows the IV behaviour at low bias (b) Photon enhanced current under different external bias voltage.

When exposed to constant laser power at same location, the photon enhanced current is determined by applied voltage. Figure 4.18(a) shows the I-V behaviour of individual nanobundle without and with laser spot at location III respectively. Inset curve shows the current behaviour at low voltage. At 0 bias, the current with laser on is 140 pA. It comes from the photon induced electrons as shown in Figure 4.13. When external bias voltage is increased, the enhanced current increases spontaneously. As shown in inset curve, the enhanced current increases gradually from 140 pA at 0 V to 206 pA at 15 mV. Figure 4.18(b) shows the enhanced current versus voltage in wider range. The enhanced value is 4.6 nA at 0.4 V as shown in Figure 4.16(b) and it increased to 190 nA at 4 V. The high external bias can readily overcome the mutual

attraction between the electron-holes pair, separate and collect the charge carriers and this contributing to the higher enhanced photocurrent.

4.6 Summary of Results

By photolithography and sputtering method, individual K_xMoO_3 nanobundle electrode device is fabricated. The electrical property of K_xMoO_3 nanobundle is systematically studied. Upon K ion insertion, the conductivity of MoO_3 increases by 7 orders of magnitude. The magnitude is also three orders higher than that of the lithiated MoO_3 bulk and five orders higher than that of lithiated MoO_3 nanobelt. The conductivity further increases 20 times as temperature increases from room temperature to 140℃. The calculated band structure of the $K_{0.25}MoO_{2.75}$ indicates the K atoms are fully ionized, giving rise to the reduction of the adjacent Mo atoms. As a consequence, the conduction band is populated, leading to electron delocalization along the rows containing low oxidation state Mo atoms in the [001] direction. These delocalized electrons contribute to the high conductivity of nanobundle. Moreover, as band structure indicates, the energy gap between two nearest states is quite small, and different energy states coexist at same energy level. Thus, the localized electrons below Fermi level could be easily excited to high energy level and contribute to the current. The effect explains the significantly increased conductivity upon heating, and the low thermal activation energy of the nanobundle.

For the low energy required to excite localized electrons and high diffusion mobility of electrons in nanobundle, significant photoelectrical response is observed. High photon induced voltage (36 mV) and photon induced current (320 pA) without external bias voltage is produced from single K_xMoO_3 nanobundle device under low laser power (2.2 mW). The experiment measurements display that the photon excited electrons come from nanobundle itself. It is unlike the reported photoelectrical response, coming from metal-semiconductor junction or p-n hybrid junction. The

amplitude and polarity of photon induced voltage/current can be controlled by the location of focused laser spot. The property enables the potential application that K_xMoO_3 nanobundle acts as nanoscale electrical source with controllable polarity and amplitude by location of focused laser spot. The photon excited electrons also enhance the current when external bias voltage is applied. Unlike the performance of photon induced current, when laser is fully shone on the nanobundle, the enhanced current values are the same regardless the location of laser spot. The same amount of electrons excited by photon and the drive force from external voltage contribute to the effect. The behaviour further demonstrates that photon excited electrons originate from nanobundle itself regardless of distance away from the electrodes. The enhanced value is also determined by the amplitude of external bias voltage. The property can make the nanobundle a possible photo-detector that measures the power of the light.

In conclusion, the great amount of K ion insertion into MoO_3 nanobundles deforms the band structure, enhances the performance of the electronic devices and introduces significant photon electrical response. These excellent performances make MoO_3 good candidate for wider application in electric and photonic related fields.

Chapter 5 Electromigration of K ions between MoO_3 layers

In our K enriched MoO_3 nanobundle, many properties coexist including the high current density, the preserved layered structure, the single crystalline material and the significant amount of K ions being inserted. It is not odd to imagine that the inserted K ions can by driven by continuous collision of numerous electrons in the channel between layers. In this chapter, we will study the amazing reversible migration of K ions between MoO_3 layers driven by electron flow.

5.1 Introduction

Electromigration describes the forced atomic or ionic motion driven by the force of electric field and associated electric current, named electrostatic force and electron wind force.[85-87] The former is exerted by the electric field on the ion, and the electron wind is caused by momentum transfer to an atom from electrons on their scattering. The net driving force causes the atoms/ions to move from its original position. In an interstitial system with applied driving force in the form of electron wind force, small interstitial ions can jump from one interstitial site to neighbouring ones while large atoms can move by position exchange with neighbouring vacancies.[87-89] In the event of high current density, a great amount of electrons scattering with atoms/ions induces electromigration, thus the phenomenon is mainly studied in metals or other materials with low resistivity.[87, 88, 90-93]

With layered crystalline structure, MoO_3 presents a wide range of sites for ions intercalation. In particular, Li ions intercalation into MoO_3 is successfully

demonstrated and the layered structure is found to be preserved during Li^+ insertion/extraction process.[36, 94] When the current density within intercalated MoO_3 is high enough to provide significant electron wind force, intercalated ions could migrate along layers. Compared with the high current density in bulk metal where electromigration takes place (10^3~10^4 A cm^{-2}),[85, 87] the current density of lithiated MoO_3 bulk ($Li_{0.25}MoO_3$ 1 A cm^{-2})[61] and lithiated MoO_3 nanobelt (10^{-3} A cm^{-2})[43] is too low to cause electromigration. Some molybdenum bronze possesses high conductivity,[60, 95, 96] but insertion of ions in the bronze gives rise to substantial structural distortion. Such as blue potassium bronze ($K_{0.3}MoO_3$), the compound becomes infinite sheets with the adjacent sheets held together by potassium ions.[97] The K ions bound by seven or ten oxygen atoms to hold the adjacent sheet can hardly move around. Consequently, the electromigration phenomenon of intercalated ions in layered MoO_3 structure has not been observed before.

In last two chapters, we have successfully synthesized K ions intercalated MoO_3 (K_xMoO_3) nanobundle with the integrity of the layered structure remaining intact. The material displays semiconductor-like behaviour with dramatic enhancement of the electric conductivity from 10^{-6} S m^{-1} of MoO_3 to 24 S m^{-1} upon potassium uptake. For samples (K-intercalated MoO_3) with a length of 10 μm and biased at 5 V, the current densities are measured to be 5×10^{-5} A cm^{-2}. The high conductivity of the K-intercalated MoO_3 nanobundle excludes the possibility of ionic conductivity which is usually low at room temperature.[98, 99] Experimental measurement of K_xMoO_3 nanobundle reveals the significant amount of oxygen vacancies in the structure. Theoretical simulation shows that hopping barrier of intercalated K ions is 0.23 eV. The high current density, the preserved layered structure, the significant amount of oxygen vacancies for position exchange and the low hopping barrier suggest the possibility that K ions can migrate along the layers readily when they are driven by electron wind force.

In the following part of this chapter, we will display the surprising reversible electromigration of the intercalated K ions in K_xMoO_3 nanobundle driven by electron wind force. When an electric current is applied to a K_xMoO_3 nanobundle, the K ions migrate readily and rapidly in the flowing direction of electrons within the nanobundle and accumulate near an electrode. A significant variation in the distribution of K ions in K_xMoO_3 nanobundle before and after the application of current is observed. Upon the reversal of current, the accumulated K ions near one electrode could be driven back and gather near the opposite electrode. By controlling the direction of the electric current, the movement of K ions along layers is shown to be reversible. Most notably, the electromigration process only takes few seconds. Compared with the reported long duration to induce significant variation of ion distribution,[100, 101] the K ions in K_xMoO_3 nanobundle migrate in a much shorter time. Moreover, repeated reversible electromigration of the K ions does not result in any changes in morphology of nanobundles.

5.2 Electromigration of K ions Detected by EDX

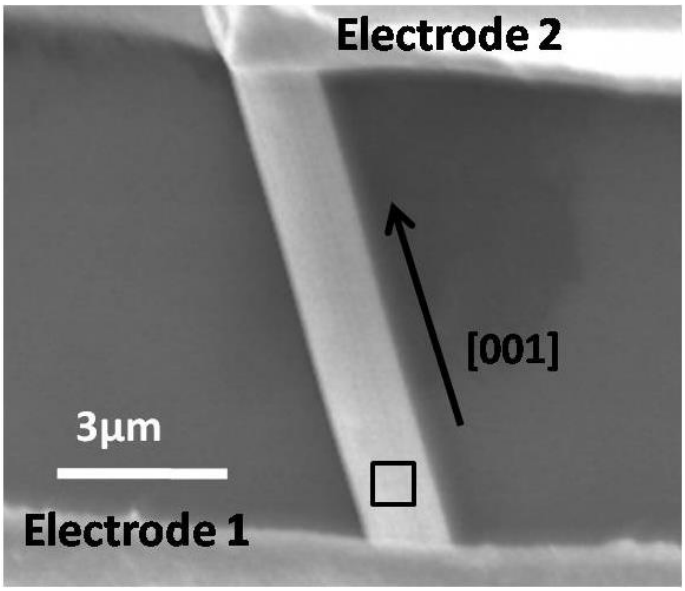

Figure 5.1 SEM image of a typical segment of nanobundle between two gold electrodes.

Similar with the electrode device preparation process described in last chapter, individual K_xMoO_3 nanobundle is transferred to a Si substrate with a 100 nm SiO_2 layer, and patterned electrodes of 10 nm Cr and 500 nm Au are fabricated via standard photo lithography and sputtering of metals. Figure 5.1 shows a scanning electron microscope (SEM) image of a typical segment of nanobundle between two electrodes. The length of the segment of nanobundle is around 10 μm and the growing direction of nanobundle is [001]. The Energy Disperse X-ray spectroscopy (EDX) (EDX in FESEM, JEOL JSM-7600F) of selected spots on nanobundle is measured to explore the distribution of K ions in K_xMoO_3 nanobundle before and after the application of electric current. In these experiments, the electrical measurements are carried out using Keithley 6430 Sub-fA Remote SourceMeter.

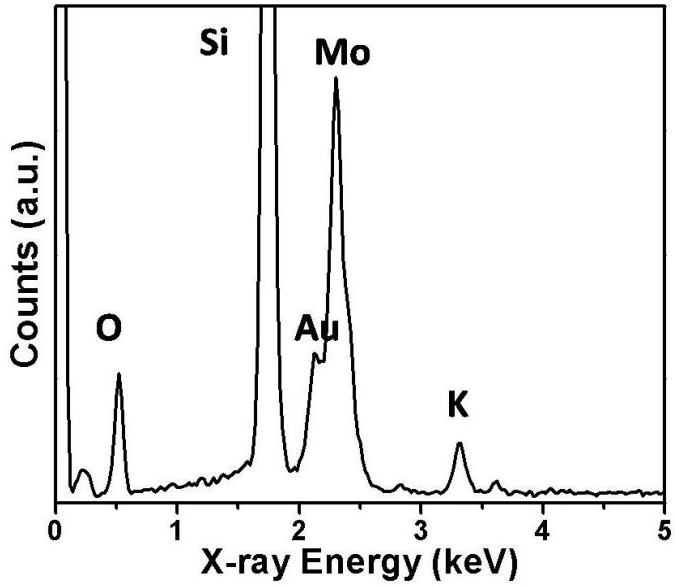

Figure 5.2 Typical EDX spectrum of K_xMoO_3 nanobundle between electrodes.

The select zoom in spot on the nanobundle for EDX measurement is in the size ~ 2μm, which is determined by the energy of electron beam, the atomic weight and density of the material. Figure 5.2 shows a typical EDX spectrum of zoom in spot on nanobundle, the Au peak comes from gold electrode, the Si peak is from Si/SiO_2 substrate, the Mo and K peaks originate from nanobundle. Since the measured atomic percentage of K varies when area exposed to Si substrate and Au electrodes change,

atomic percentage ratio of K over Mo is characterized to exclude the influence of substrate and electrodes. From the area of the peaks, the value and error of atomic percentage ratio of K over Mo are calculated. In MoO_3 structure, each of the lattice Mo atoms is tightly bonded to the surrounding six O atoms and thus can hardly move, while the fully ionized intercalated K atoms are not completely trapped. Electromigration occurs primary through the untrapped interstitial atoms.[87, 102] Consequently, it is reasonable that Mo atoms remain stable and uniformly distributed in the MoO_3 lattice during electromigration process. Hence the atomic percentage ratio of K over Mo is used to study the distribution of K atoms in the following experiment.

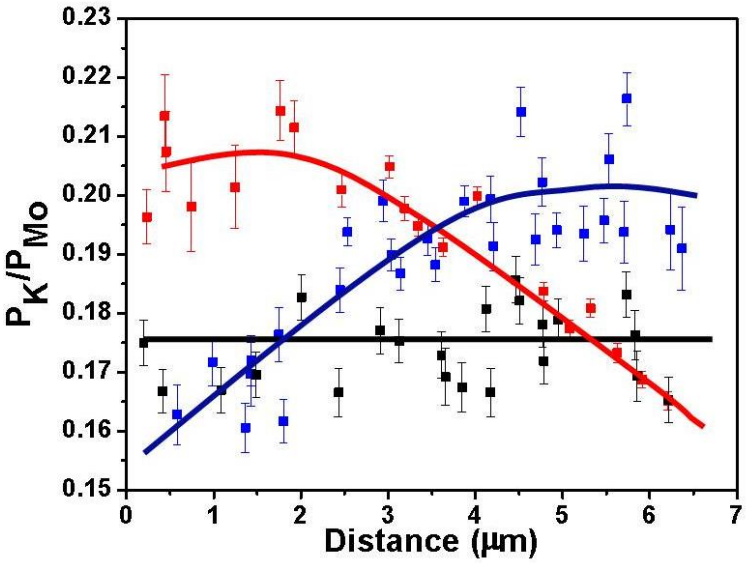

Figure 5.3 Measured atomic percentage ratio of K over Mo versus distance away from electrode 1 in the sample before applied bias voltage (black square), after applied positive bias voltage (red square) and after applied negative bias voltage (blue square).

Before the application of current, the EDX spectra of selected positions along nanobundle in SEM are measured. The atomic percentage ratio of K over Mo versus distance away from electrode 1 is shown in black squares in Figure 5.3. The black line drawn to the data is meant to guide the eyes. The similarity in the magnitude of atomic ratio along the nanobundle reveals the uniformly distributed K ions in nanobundle before applying the current. The result is consistent with the EDX measurement in TEM as described in Chapter 3, that the atomic percentage ratio of K over Mo is fixed along the individual nanobundle.

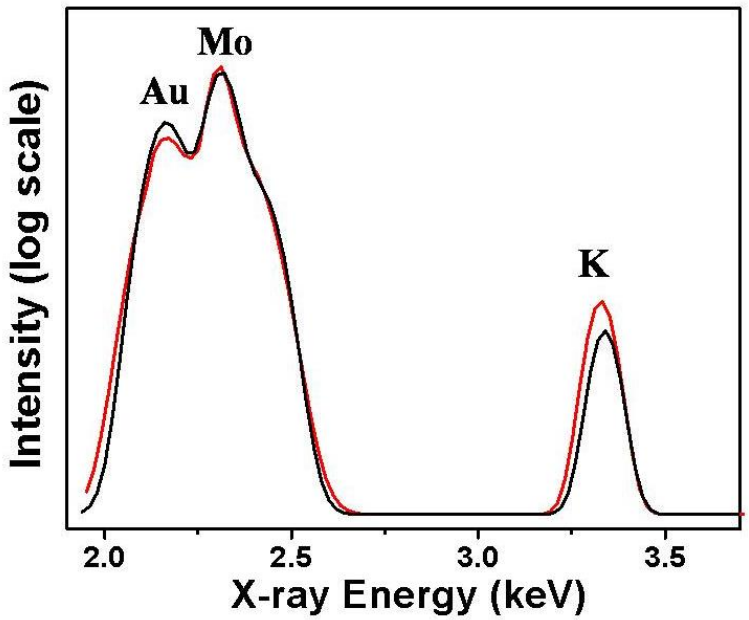

Figure 5.4 Log scale of EDX intensity measurement from the area highlighted by black square in Figure 5.1 before (black curve) and after (red curve) application of electric current.

Upon the application of a positive bias voltage (+5 V) for 30 min, the current flows from electrode 1 to electrode 2 as shown (black arrow) in Figure 5.1. For better displaying the change of ion concentration, log scale of detected X-ray intensity versus X-ray energy is performed. The black and red curve in Figure 5.4 shows the log scale of EDX intensity measurement in the square box highlighted in Figure 5.1 before and after applying current respectively. The area of Mo peak in two curves is almost the same but the area of K peak increases after the application of the electric current. It denotes the increased amount of K atoms in the square box. The red squares in Figure 5.3 shows the measured atomic percentage ratio of K over Mo at different distances away from electrode 1 after applied current. Near electrode 1, the atomic ratio is around 20.5%, while the value decreases to 16.5% for regions close to electrode 2. The accumulated K ions near electrode 1 and the depletion near electrode 2 show that K ions migrate from negative electrode (electrode 2) towards positive electrode (electrode 1) along the direction of electron flow (i.e. opposite to the electric current).

The sample is subsequently subjected to a reverse applied bias voltage (-5 V) for 30 minutes, current flows from electrode 2 to electrode 1. The blue squares in Figure 5.3 describe the resultant distribution of atomic percentage ratio of the sample. The high ratio near electrode 1 in red squares decreases to 16% in blue squares, and the ratio near electrode 2 increases to 20%. It reveals that the accumulated K ions near electrode 1 are flushed back by electron wind force in opposite direction and accumulate near electrode 2 instead.

During the EDX measurement, although the majority of detected X-ray comes from the small area centered at selected spot, the extended beam profile of the e-beam results in some EDX contribution of surrounding region. As shown in the EDX curve (Figure 5.2), due to the large area of surrounding Au electrodes, although the electron beam is aimed at the middle of nanobundle, a small peak of Au is detected. Consequently, the measured atomic percentage is the weighted average value of the area centered at selected spot instead of the precise value at the spot. Taking into account the spreading of electron beam, the value we obtained is thus an underestimation. Meanwhile, we could not carry out EDX analysis and apply the current simultaneously. The EDX measurement is carried out around 30 mins after the application of the electric current. We observe that the accumulated K ions gradually disperse overtime and this is driven by concentration gradient force. Thus the measured concentration of K ions is lower than the value obtained immediately after the application of current. Although the accumulation effect is underestimated considering these two factors, the EDX analysis does clearly show the trend of reversible electromigration of K ions driven by electron wind force.

5.3 Structural Characters for Electromigration

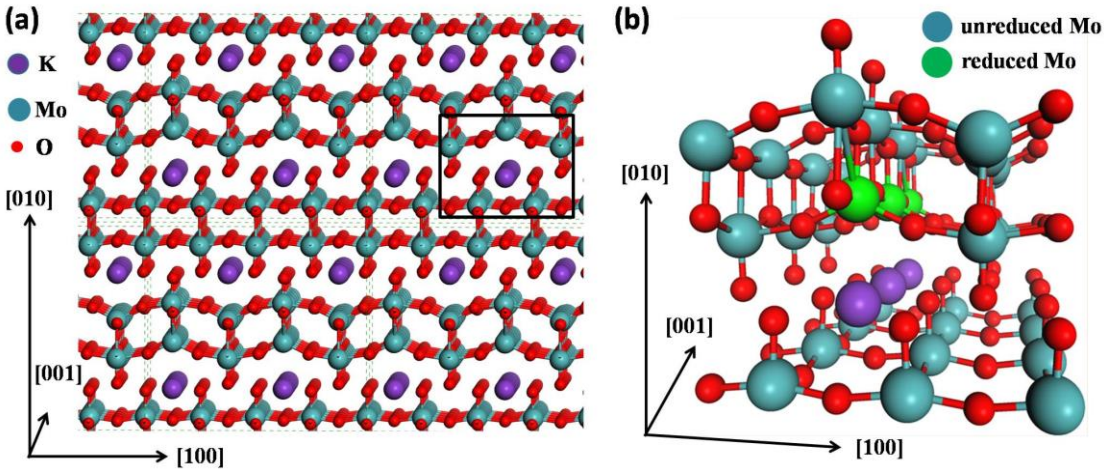

Figure 5.5 (a) Structure of K enriched MoO_3 nanostructure (b) Zoom-in image of area highlighted by black square in (a).

Beside the high current density that guarantees the electromigration of K ions between layers, some unique structural properties of K_xMoO_3 nanobundle favour the electromigration process. According to experimental measurement and theoretical modelling, K atoms likely occupy the oxygen vacancy sites in the lattice. The schematic atomic structure is shown in Figure 5.5(a). Between the MoO_3 layers, the dangling O are removed as O vacancies in the lattice and K atoms occupy these vacancy sites. These K atoms are aligned in the channel formed by O vacancies along [001] direction. The EDX measurement in Chapter 3 shows that the amount of O vacancies is larger than that of K atoms, suggesting that not all vacancy sites are occupied. Figure 5.5(b) is the zoom-in image of the area highlighted by black square in Figure 5.5(a). Two kinds of Mo atoms are notable, one with O vacancy (reduced Mo atoms, green ball) and the other without (unreduced Mo atoms, blue ball). The ionization of the K atoms at vacancy site gives rise to the reduction of the adjacent Mo atoms, leading to electron population in the conduction band. Therefore, the high current density arises solely from the reduced Mo atoms, which are aligned in the [001] direction as shown in Figure 5.5(b). While the rows in which the Mo atoms remain in the high oxidation states are still semi-conductive due to lack of electron occupation in the conduction band. Consequently, when the current is applied in [001] direction, electrons mainly

flow along these rows with the reduced Mo atoms. This is exactly the position where K atoms reside. Thus, K atoms can be mobilized by scattering of a great amount of flowing electrons.

Meanwhile, these fully ionized K ions are weakly bound to the surrounding O atoms in the lattice. Theoretical simulation reveals that the hopping barrier of intercalated K ions is 0.23 eV, which is comparable with electromigration activation energy in conventional electromigration.[103-105] Moreover, a significant amount of oxygen vacancies available in the structure for position exchange ensures facile diffusion of K ions.[87, 89] All these structural characters contribute to the ease of electromigration of K ions in K_xMoO_3 nanobundles.

5.4 Remnant Voltage induced by Accumulated K ions

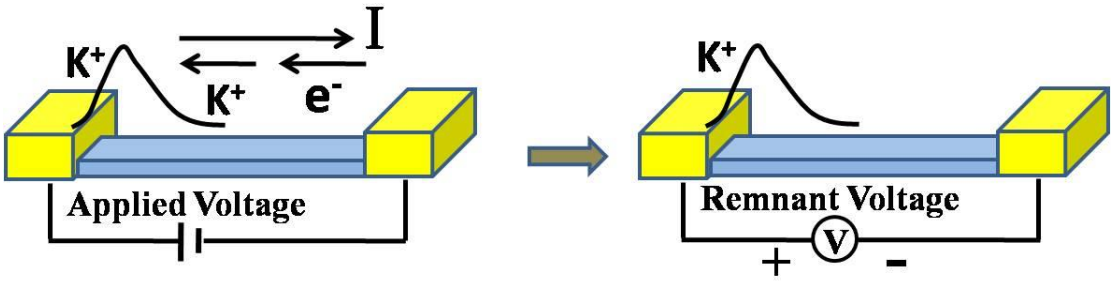

Figure 5.6 Schematic figure shows remnant voltage measurement process.

As shown by the EDX measurement, under the influence of electron wind force, K ions are driven to the electrode. The accumulation of K ions near the electrode introduces additional electric potential to the nearby electrode. After the applied current is removed, the electric potential between two electrodes induced by the accumulated K ions is measured and denoted as remnant voltage. The schematic figures in Figure 5.6 display the described process. To probe the properties of the remnant voltage, the sample is applied at different bias voltage for 20 s and the remnant voltage is measured immediately the moment applied bias is removed.

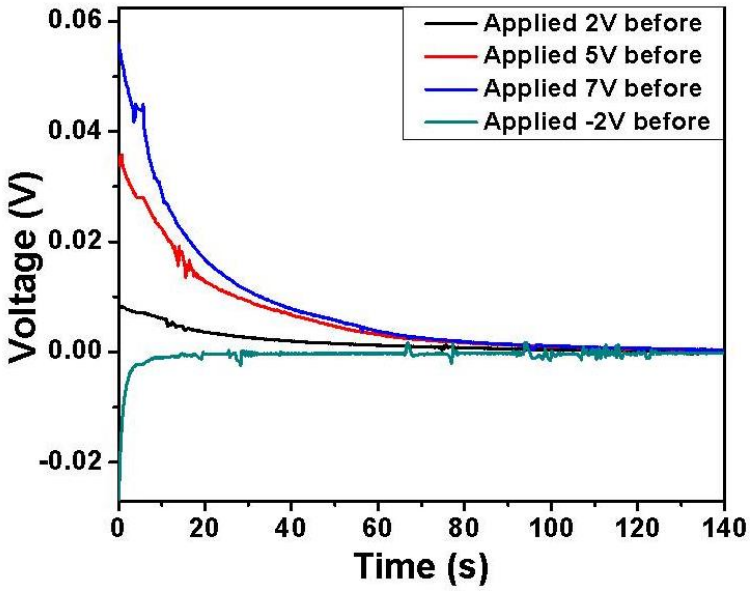

Figure 5.7 After bias voltage (7 V, 5 V, 2 V and -2 V) is applied for 20 s, remnant voltage between two electrodes is measured with time respectively.

The black, red and blue curves in Figure 5.7 show the measured remnant voltage after bias voltage of +7 V, +5 V and +2 V is applied respectively. The measured positive remnant voltage is consistent with the observation that K ions migrate towards positive electrode when positive bias voltage is applied. The significant starting remnant voltage (56 mV after applying 7 V bias for 20 s) indicates that great amounts of K ions are indeed accumulated upon the application of electric current. Figure 5.6 clearly describes the process. Upon the application of the positive bias voltage, electrons flow from negative end to positive end and drive K ions to positive electrode. Immediately after the removal of the bias, the voltage between two electrodes is measured. Since accumulated K ions are near positive electrode, the recorded remnant voltage is positive. The green curve in Figure 5.7 shows the measured remnant voltage after negative voltage of -2 V is applied. The negative remnant voltage suggests that K ions migrate towards negative electrode and accumulate over there. The measured remnant voltage after applying positive and negative bias voltages proves that K ions migrate in the direction of electron flows driven by electron wind force.

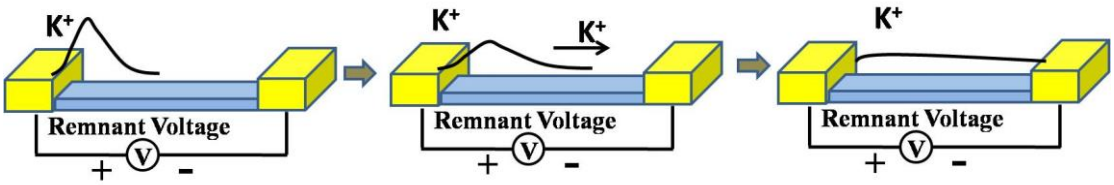

Figure 5.8 Schematic images of K ions dispersion process.

Driven by concentration gradient force, the accumulated K ions diffuse back toward opposite electrode in the nanobundle as shown in Figure 5.8. Accumulated K ions disperse gradually and finally equally distributed along the nanobundle. As the concentration of accumulated K ions decreases with time, the remnant voltage decreases as well. The exponential fitting of black, red and blue curves in Figure 5.7 shows the decay time of remnant voltage is around 20 s. The results indicate a very short relaxation time of accumulated K ions, in contrast to the previously reported system where the relaxation of accumulated ions upon removal of the bias takes a few hours.[92, 101] The short decay time reveals the facile diffusion of K ions along the channel formed by the layered structure.

When accumulated K ions disperse in the same direction, the decay time and the pattern of curve are similar as shown in the black, red and blue curves in Figure 5.7. On the other hand, when accumulated K ions disperse in different directions, the decay time and the pattern of curve are different as shown in the black and green curves in Figure 5.7. This difference can be attributed to different history of the applied current in both directions and the random ion-vacancy position exchange. In addition, the channels, along which the K ions move, are not symmetrical in both ends. Moreover, the contact situation between metal electrode and nanobundle differs on two terminals. Hence even though the same current is applied for the same period in both directions, the distribution of accumulated K ions are different and the way these accumulated ions disperse are also different. It leads to the varied amplitude of starting remnant voltage and the different decay patterns of remnant voltage in both directions. For the same

reasons, the decay time of each device is different from each other. But the values of decay time in all devices are smaller than 40 s, significantly lower than the reported relaxation time of accumulated ions. [92, 101]

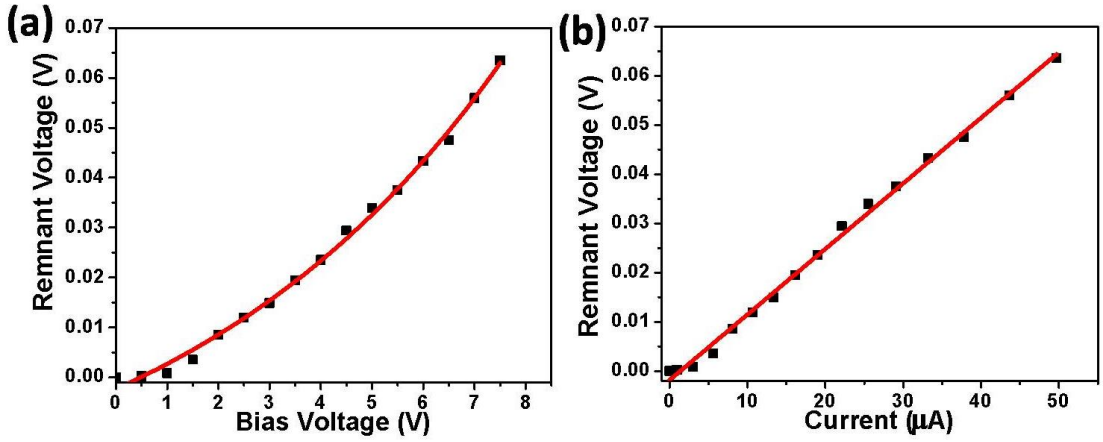

Figure 5.9 (a) Measured starting remnant voltage after different bias voltage is removed (b) Measured starting remnant voltage versus external bias current applied.

Comparison among curves in Figure 5.7 reveals that a higher starting remnant voltage is measured when a larger bias voltage is applied. Figure 5.9(a) shows the measured starting remnant voltage after different bias voltage is applied. The experiment data is well fitted by exponential curve. A higher bias voltage induces a larger current density and higher electron energy and, consequently, enhances the electron wind force. With larger driving force, more K ions are accumulated, which provides higher remnant voltage. To further identify the effect of key parameter – current density, the measured starting remnant voltage versus applied bias current is plotted in Figure 5.9(b). Clearly that the starting remnant voltage increases linearly with bias current denoted by red fitting line. It suggests that the amount of accumulated K ions linearly depends on current density. A kink at 3 μA is observed. The measured starting remnant voltage is quite low and only increased a bit when bias current is lower than 3 μA. It is attributed to the fact that certain energy is required to dislodge K ions and the significant remnant voltage can be observed only when large amount of ions are driven. When low current density (<3 μA) is applied, the energy provided by electron momentum transfer is not strong enough to drive K ions to the electrode. The threshold bias current denotes the hopping barrier of K atoms in the

structure, and the low threshold bias current is indicative of the small activation energy of K atoms in the structure, which is consistent with the theoretical calculation of hopping barrier of K atoms (0.23 eV).

5.5 Temperature dependence of Electromigration

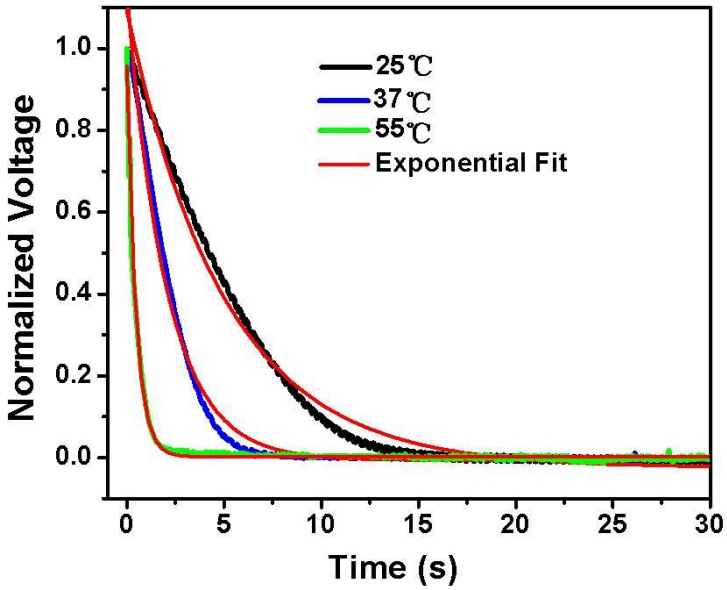

Figure 5.10 After bias voltage 2 V is applied for 20 s, normalized remnant voltage between two electrodes is measured versus time under different temperature.

As described in last chapter, current density in the K_xMoO_3 nanobundle greatly increases with temperature (30 times with temperature increases from 25℃ to 200℃), and the diffusion coefficient increases with temperature as well. Both factors greatly enhance the amount of K ions being driven. Due to the limitation that around 1.5 s is required for Keithly source meter unit to switch between different functions (as source and as voltmeter), and more K ions diffuse back during the interval as temperature increases, the starting remnant voltage versus temperature could not be systematically studied. However, the temperature dependence could be studied by focusing on two factors, current density and diffusion coefficient. The effect of current density is systematically studied as shown in Figure 5.9(b). The change of diffusion coefficient under different temperature could be studied by decay time of remnant voltage under various temperature.

For temperature dependent electromigration observation, the sample is mounted on heating stage and the remnant voltage measurement is repeated under different temperature after bias voltage 2 V is applied for 20 s. To better characterize the diffusion coefficient under different temperature, the maximum remnant voltage values are normalized. The three curves (blue, cyan and green curves) displayed in Figure 5.10 correspond to normalized remnant voltage versus time under temperature of 25℃, 37℃ and 55℃ respectively. Obviously, as temperature increases, remnant voltage decays faster and faster, denoting the higher diffusion coefficient of K ions. These three curves are exponentially fitted, and the decay times are 5.6 s, 2.1 s and 0.5 s respectively. The decreasing decay time suggests the increase of diffusion coefficient in the material as temperature increases.

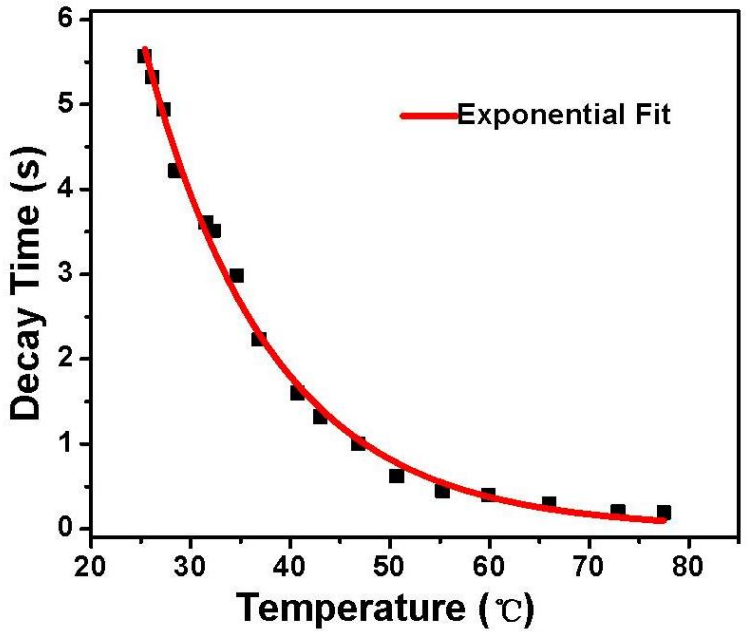

Figure 5.11 The exponential decay time of remnant voltage under different temperature.

The decay time under different temperature is recorded and plotted versus temperature in Figure 5.11. The data is well fitted by an exponential function and shows that the decay time of remnant voltage exponentially decreases as temperature increases with the equation $\tau = \tau_0 e^{-\frac{T}{T_0}}$, τ is the decay time, T is the absolute temperature, T_0 is the decay constant with the value around 12.7 K. Considering the

fact that given a fixed length, the diffusion time is inverse proportional to diffusion coefficient, thus, the diffusion coefficient (D) of K ions in the structure increases exponentially with temperature in the measured temperature region, $D = D_0 e^{\frac{T}{T_0}}$ with constant T_0 around 12.7 K.

The exponentially increased diffusion coefficient of ions upon temperature is the same both in accumulation process and dispersion process. And the current density exponentially increases upon temperature described in Chapter 4. Although the temperature dependent electromigration of K ions driven by electrons are not directly measured, we can conclude that the K ion electromigration is exponentially dependent on temperature of nanobundle.

5.6 Time dependence of Electromigration

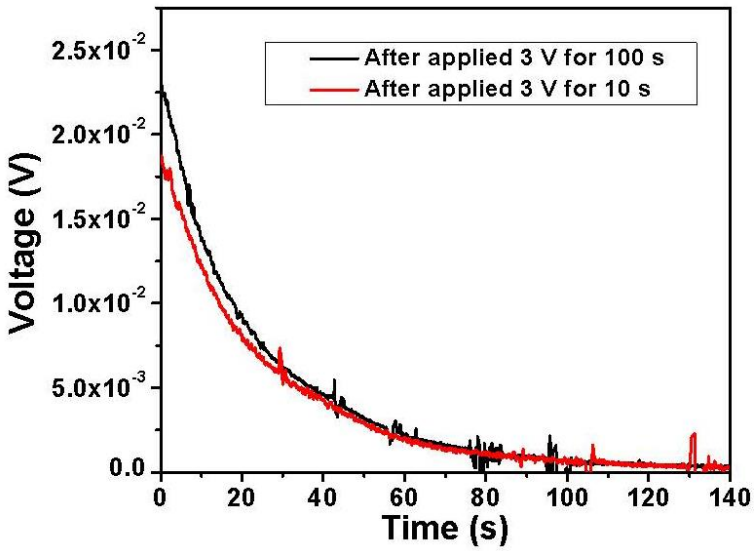

Figure 5.12 After bias voltage (+3 V) is applied for 10 s and 100 s, red and black curve show measured remnant voltage versus time respectively.

In interstitial system, long period (10^3~10^4 s) is required to observe significant concentration change of interstitial atoms upon electromigration.[100, 101] To study the time dependence of electromigration of intercalated K ions in MoO_3 nanostructure, same bias voltage (+3 V) is applied to the sample for different durations and the

remnant voltage is measured immediately the moment bias voltage is removed. Due to the system limitation, the minimum period of the applied bias voltage is around 10 s. The red line in Figure 5.12 shows the measured remnant voltage versus time after bias voltage +3 V is applied for 10 s, and the starting remnant voltage is 18.7 mV. The black line shows the remnant voltage versus time after bias voltage +3 V is applied for 100 s, and the starting remnant voltage is 23.5 mV. Applying similar bias voltage for a longer duration, e.g. 3000 s, the starting remnant voltage is around 24~25 mV. The small variation of starting remnant voltage implies that the accumulation of K ions becomes saturated with no additional K ions accumulated near the electrode. Moreover, the pattern of remnant voltage decay is almost the same when different duration of bias voltage applied, suggesting the long time application of bias voltage does not impose effect on ion diffusion.

We assume that the initial electron wind force is much larger than the concentration gradient force and electrostatic force, for the uniformly distributed K ions along nanobundle. This results in rapid accumulation and a significantly enhanced remnant voltage of 18.7 mV for the initial 10 s. With a longer period of current applied and more K ions accumulated, the net force on K ions gradually decreases and eventually diminishes without any net K ion accumulation. Thus, the starting remnant voltage only increases by 4.8 mV in the interval from 10 s to 100 s, and it further enhances slightly (<1 mV) in the period from 100 s to 3000 s. The short duration (10 s) required to achieve significant accumulation of K ions is consistent with the short relaxation time (30 s) of remnant voltage as shown in Figure 5.7. Both values indicate the high diffusivity of K ions in the structure. The duration is much shorter than the time (10^3~10^4 s) required in the interstitial systems reported previously.[100, 101] It should be noted that in these interstitial system, only small intercalated ions, such as Li^+ and H^+, are studied, while in our system, the size of intercalated ion K^+ is significantly larger. The performance that shorter duration required to move larger ions along layers makes our nanobundle an excellent material to act as ion channels.

5.7 Reversible Electromigration observation

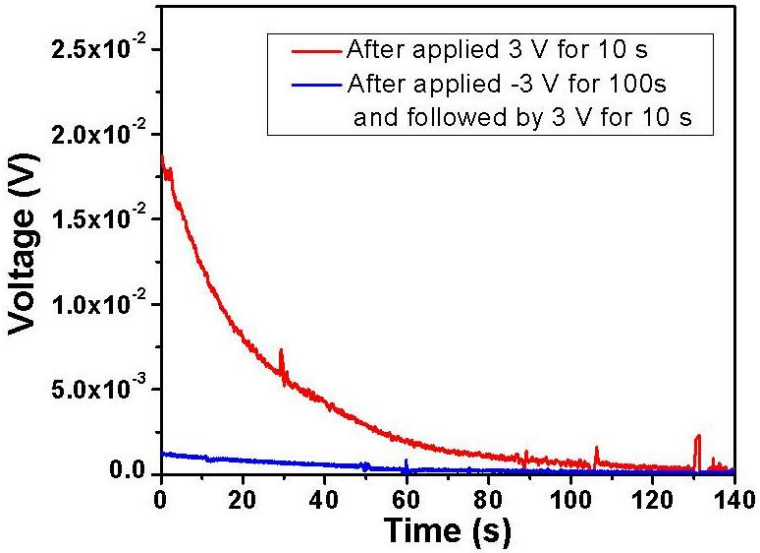

Figure 5.13 After bias voltage (+3 V) is applied for 10 s, the remnant voltage versus time is shown by red curve. After bias voltage (-3 V) is applied for 100 s and then bias voltage (+3 V) is applied for 10 s, blue curve shows measured remnant voltage.

The accumulated K ions on one end forced by electric field could be driven back by concentration force between ions and electron wind force in opposition direction. The reversible electromigration in nanobundle is subsequently studied. We firstly apply negative voltage -3 V for 100 s, upon the removal of the negative bias voltage, positive bias voltage +3 V is immediately applied for 10 s and the remnant voltage is measured as shown in blue curve in Figure 5.13. The measured remnant voltage is positive, while the value after minus voltage applied should be negative as shown in Figure 5.7. It suggests the accumulated ions near negative electrode is driven back and partly accumulate near positive electrode. The starting remnant voltage is 1.2 mV, which is significantly lower than the starting remnant voltage (18.7 mV) when no bias voltage is applied before the application of positive voltage (red curve in Figure 5.13).

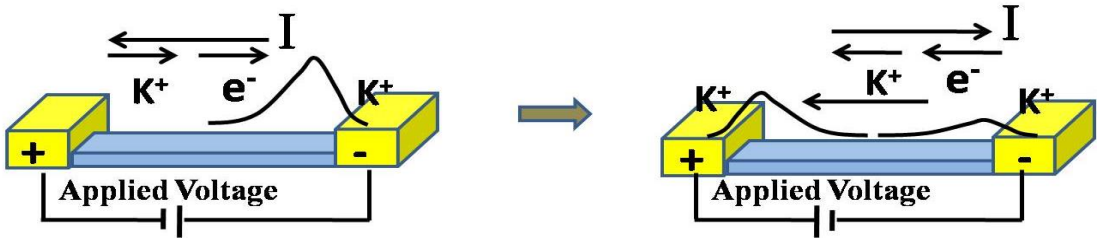

Figure 5.14 Schematic image describes the reversible electromigration process.

The schematic figures in Figure 5.14 describe the above reversible electromigration process. Due to the long duration of negative bias voltage applied, great amounts of K ions accumulate near negative electrode driven by electron wind force. When positive bias voltage is applied, for the same direction of electron wind force and concentration gradient force, accumulated K ions are driven back quickly and aggregate near positive electrode. As a result, the K concentration near positive electrode is higher than that near negative electrode, and the measured remnant voltage is thus positive. However, it takes time to move K ions from negative side to positive side. Consequently, in the same duration (10 s), the measured starting remnant voltage (1.2 mV) is lower than the value (18.7 mV) when K ions are moved from uniform distribution to positive end. When longer duration (20 s) of positive voltage (+3 V) is applied, the measured remnant voltage versus time is almost the same as red curve in Figure 5.13 with starting voltage around 19 mV. Various arrangements of different voltage are further tried. The experiments show that when higher negative voltage (-5 V) is applied for 100 s, the applied positive voltage (+3 V) for 10 s is not strong enough to drive large amount of ions to opposite terminal in limited duration (10 s). Thus, the measured remnant voltage is still negative. A longer duration or a larger positive bias voltage can drive more accumulated K ions back and make the remnant voltage positive.

In general, the experiment shows that accumulated K ions can be driven back and gather in the other end when the current in opposite direction is applied. The distribution of accumulated ions depends on the duration and amplitude of the applied bias voltage and the history of the applied bias voltage. After the reversible ion movement is repeated for hundred times, the reversible migration of K ions is still observed in remnant voltage measurement and, in particular, no expansion, void and cracks in the nanobundle are observed, while expansion and cracks is always observed in traditional electromigration process both in bulk and in nanostructure.[87, 106] The unchanged morphology and the existence of reversible electromigration suggest that

the MoO_3 layered structure is highly stable, and the ions movement along layers and the ion accumulation do not significantly deform the structure.

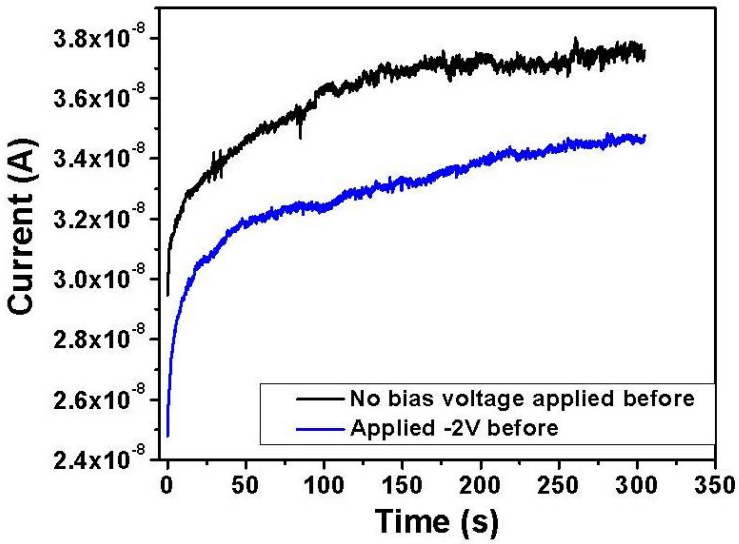

Figure 5.15 Current increases with time when bias voltage (+2 V) is applied in sample without bias voltage applied before (black line) and with bias voltage (-2 V) applied before (blue line).

During the application of current, K ions are driven to one end which imposes an additional voltage and thus influences the current. Positive bias voltage +2 V is applied to the sample and current is measured versus time as shown in black curve in Figure 5.15. The current starts from 29.5 nA and increases sharply in the first few seconds. Then the slope gradually decreases, and finally the current reaches the equilibrium value of 37.5 nA. The increased current is due to the additional electric potential induced by accumulated K ions and the stable current suggests that the concentration distribution of K ions is equilibrated under electrostatic force, electron wind force and concentration gradient force. The sharp increase of the current in the first few seconds reflects the fast increase of additional voltage which is induced by the rapid accumulation of K ions at the beginning as discussed above.

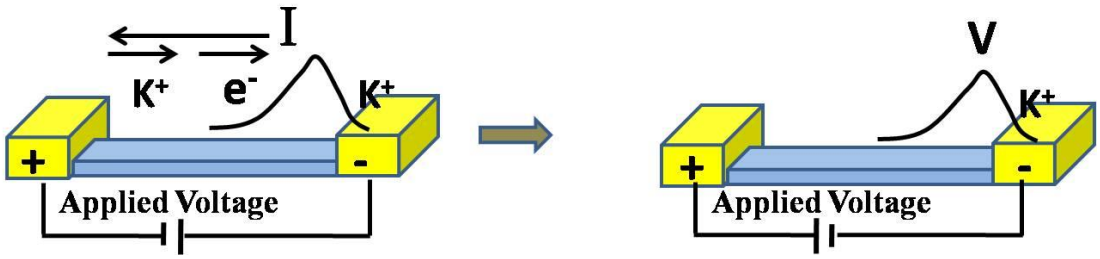

Figure 5.16 Schematic image describes the distribution of K ions at the moment the polarity of external bias voltage reverses.

Subsequently, negative bias voltage -2 V is applied to the sample for a certain period of time to drive back K ions to negative electrode. The measured remnant voltage becomes negative, denoting the accumulation of K ions near negative electrode. Then positive bias voltage +2 V is applied and the current is measured as shown in blue line in Figure 5.15. The starting current is 24.7 nA, lower than the starting current (29.5 nA) in black curve. Figure 5.16 describes the distribution of K ions at the moment the polarity of external bias voltage reverses and explains the mechanism of blue curve in Figure 5.15. Due to the negative bias voltage applied, K ions are driven to negative electrode. The accumulated K ions near negative terminal induce an additional remnant voltage which cancels part of electric potential when positive bias voltage is applied. Thus the starting current is lower than the value obtained with no prior applied voltage. If larger amplitude of negative bias voltage is applied, lower starting current can be then measured due to increased concentration of accumulated ions near negative electrode.

In the first 10 s, the current increases more sharply from 24.7 nA to 29.8 nA (blue curve, increase 5.1 nA) than from 29.5 nA to 32.6 nA (black curve, increase 3.1 nA). It is consistent with the observation discussed above that greater amount of K ions moves in the same duration under same bias voltage when accumulated K ions are driven back. After 300 s, although the blue curve tends to close to the black curve, there is still a gap of approximately 2.5 nA between them. It is possible that when K ions are scattered by electrons, some of them hop to the oxygen vacancies in the nearby channels where the

current density is low due to the high oxidation state of surrounding Mo atoms. It makes these K ions hard to be driven back by electron wind force. Consequently, longer duration is required to achieve equilibrium. This is also the reason we could still detect accumulated K ions by the EDX measurement half an hour after K ions packing.

5.8 Summary of Results

In summary, we report an interesting observation of reversible electromigration of intercalated K ions in layered single crystalline K_xMoO_3 nanobundles. The varied concentration distribution of K ions from the EDX measurement, the remnant voltage measurement and I-t measurement confirm the observation that when subjected to the application of electric current, K ions in the lattice migrate along nanobundle and ions move in parallel to the flowing direction of electrons. Our results reveal that K ions are driven by electron wind force. Upon the reversal of current, accumulated K ions near one electrode are driven back and gather near the opposite electrode. For the rapid diffusion of K ions in the lattice, the duration required to induce significant accumulation of K ions and the relaxation time are significantly shorter than the value reported in other interstitial systems. The amount of accumulated ions can exponentially increase with temperature, resulted from exponentially increased current density and diffusion coefficient with temperature in the nanobundle. The layered structure is preserved during reversible electromigration of intercalated ions with no expansion, void or cracks observed.

The reversible electromigration of K ions in our nanobundle provides a new direction to study the ion migration in semiconductor and in nanostructure. It is such a new phenomenon that electromigration mechanism could be further explored by systematic examination of the effect. Moreover, the easy electromigration of K ions in K_xMoO_3 nanobundle enable its application as ion diffusion channels or ion exchange hosts.

Chapter 6 Synthesis and Characters of K enriched WO_3 nanostructure

Considering the similar structural and chemical properties of W with Mo, we assume that the synthesis method of K_xMoO_3 could be used in WO_3 system and the new performance induced by intercalated K ions should be observed. In this chapter, we apply the same simple one-step method to synthesize K ion intercalated WO_3 nanostructure. Various experimental characterization techniques are used to characterize the material. The electrical property and photon electrical response are studied as well.

6.1 Introduction

The lattice of tungsten oxide is capable of accommodating considerable ion insertion. Modified by ion incorporation, and together with oxygen deficiency commonly found in these compound, WO_3 displays new properties and exhibits broad technological applications,[107-109] including electrochromic devices,[3, 110, 111] batteries,[112] photochromic devices,[113] gas sensors[114] and catalysts[115, 116], as discussed in Chapter 1. However, upon the intercalation, the structure of WO_3 is known to deform and proceed to higher symmetry. Intercalation of alkali metal ions into WO_3 by electrochemical method reveals the phase transition from monoclinic phase to tetragonal phase occurs with x ~0.1 (Li_xWO_3) and further deforms to cubic phase with x~0.36.[117, 118] The chemical reduction of WO_3 is also accompanied by structural changes. The lattice tends to eliminate these oxygen vacancies by a crystal shear mechanism, where groups of edge sharing WO_6 octahedra are rearranged along some crystallographic planes.[119-121] Further reduction involving the formation of pentagonal columns occurs when x> 0.13

(WO_{3-x}). Schematic images in Figure 6.1 display the monoclinic structure of WO_3 and the structure of W_5O_{14} in the [001] direction. Clearly that, the monoclinic structure of WO_3 deforms after chemical reduction and displays a net-work of hexagonal and pentagonal columns.[119] To date, intercalating cationic species into WO_3 structure and chemical reduction of WO_3 without giving rise to severe structural deformation or a change of phase has remained a technical challenge.

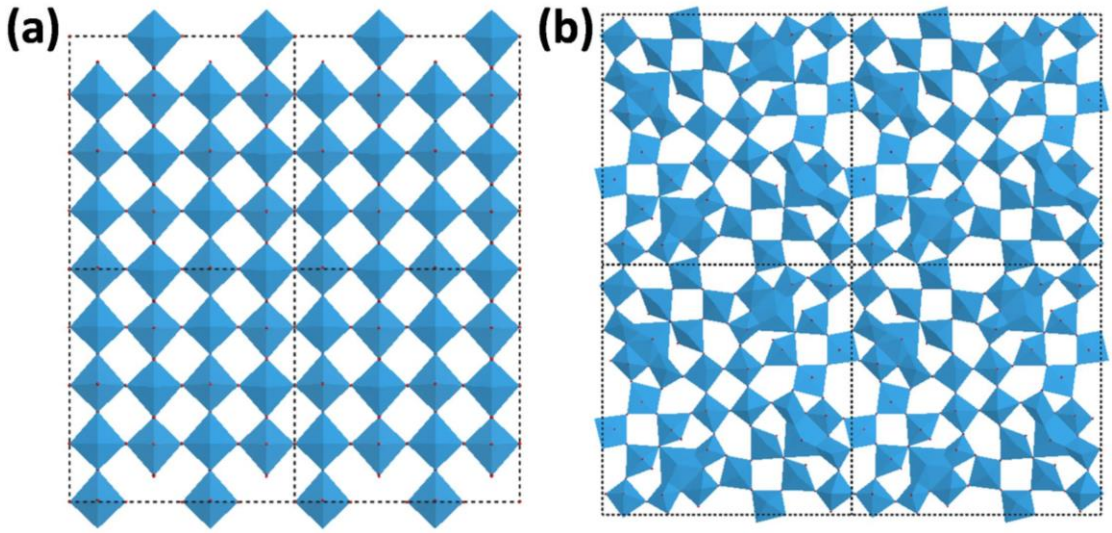

Figure 6.1 Schematic representation of (a) monoclinic WO_3 in the [001] direction (b) W_5O_{14} in the [001] direction with a net-work of hexagonal and pentagonal columns.[119]

In last three chapters, we have shown the synthesis of enriched K ions intercalated MoO_3 by simple thermal evaporation method on mica substrate. The layered MoO_3 structure is found to be preserved despite the large amount of K atoms intercalation. Ion intercalation introduces many amazing properties to MoO_3. The electrical conductivity of the K enriched MoO_3 nano-material is enhanced by seven orders of magnitude, the significant photon electrical response and reversible electromigration are observed. Continuing our successful attempt, the same growth method is applied to grow K enriched WO_3 nano-materials.

In the following of this chapter, we will describe the synthesis method and characters of K-intercalated WO_3 single crystalline nanostructure. Although a high amount of K atoms are intercalated, the pseudo-orthorhombic structure (monoclinic

structure with β close to 90°)[7] of WO_3 is preserved. The K_xWO_3 nanostructure exhibits substantially high electrical conductivity with the value enhances five orders from 10^{-4} Sm^{-1} of WO_3 to 40 Sm^{-1} upon potassium intercalation. This value further increases 200 times when temperature increases from 23 ℃ to 200 ℃. The electrical conductivity is also found to be thermally activated with an energy barrier of ~1eV. Density functional theory (DFT) under the generalized gradient approximation (GGA) is utilized to understand the variation of electronic structure of the nano-materials upon insertion of K ions and to explain the observed high n-type conductivity. Both calculated band structure and measured thermal activation energy consistently suggest that only a small amount of energy is required to excite the localized electrons to the conduction band. During experiment, the nanobundle exhibits significant photon induced current (9 nA) without external bias under low laser power (2 mW) while the value measured in reports concerning other semiconductor nanomaterials ranged from ~10 pA to ~500 pA.[72, 77, 78]

6.2 Synthesis of K ion intercalated WO_3

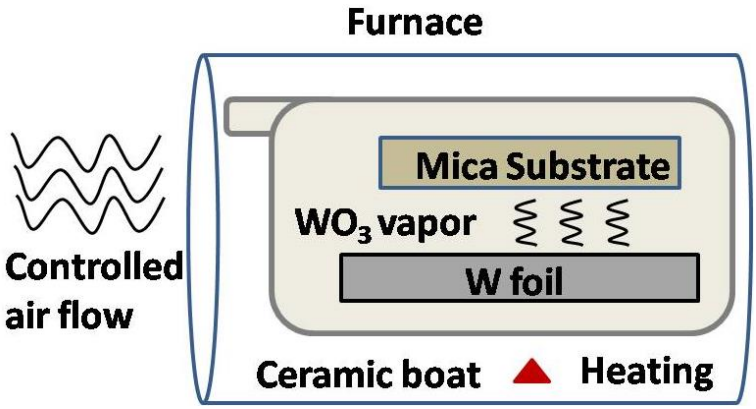

Figure 6.2 Schematic of the synthesis system of K_xWO_3.

Our group has successfully fabricated WO_3 nanowire using thermal evaporation method on silicon substrate.[122] Considering the similar structural properties, chemical properties and the synthesis process with MoO_3 nanowire, we continue our effort on ion insertion into transition metal oxide nanostructure. Similar with the synthesis process described in Chapter 3, we begin with a W foil (5 mm×5 mm×0.05 mm in

size, from Aldrich Chemical Co., Inc.) as W source. A muscovite mica sheet is prepared as substrate and K source. Unlike the synthesis of K_xMoO_3, the mica sheet is placed directly on top of the W foil in this case. The system is inserted into a tube furnace (Carbolite MTF 12/25/250) and heated for 3 days in ambient at 650 ℃ with controlled air flow. The synthetic scheme of the K intercalated WO_3 nanostructure described is shown in Figure 6.2.

Same as the synthesis of K_xMoO_3, adequate oxygen is highly required to successfully synthesize K_xWO_3 nanostructure. A fan near one end of furnace is thus utilized to continuously provide fresh air flow. The distance between substrate and foil is controlled to maintain adequate vapour concentration and reaction speed. Since the melting point of WO_3 (1473 ℃)[123] is greatly higher than that of MoO_3 (795 ℃)[124], the concentration of WO_3 surface vapour is significantly lower than MoO_3. In K_xMoO_3 case, when mica substrate directly covers on the Mo foil, the concentration of MoO_3 vapour is so high that the nucleation process suppresses the reaction with mica surface, resulting the low productivity of K_xMoO_3. While in K_xWO_3 case, when mica substrate is elevated, the concentration of WO_3 vapour is so low that little reaction takes place, resulting low productivity of K_xWO_3. Consequently, the substrate is elevated in K_xMoO_3 case, but directly covers on foil in K_xWO_3 case.

Temperature for nanostructure synthesis is optimized. K_xWO_3 nanostructures are produced in the temperature window ranged from 650 ℃ to 720 ℃, while nothing is observed when temperature is out of the range. The inferior temperature limit is determined by the high melting point of WO_3. Higher temperature will accelerate the evaporation of WO_3 vapour and prompt the synthesis. The superior temperature limit is determined by the structural stability of mica substrate. The mica substrate is heated under different temperature for 2 hrs and the XRD measurement is performed respectively to study the thermal stability of mica substrate. Figure 6.3 displays the peak denoting (004) surface[125] after substrate is treated under different temperature.

The substrate displays distinct layered structure as shown by red curve with significantly large peak intensity. As heated in 600 ℃, the structure slightly deforms with distance between layers shifting a bit. It reduces the peak intensity and broadens the peak. However, the layered structure is still preserved and the peak position does not change as shown by green curve. As temperature increases to 750 ℃, the layered structure further deforms. Mica dehydrates as temperature increases and transforms to other material.[52] The changed layer distance and the deformed structure block the diffusion channel of K ions between layers.[58, 59] The formation of K_xWO_3 is thus terminated and no nano-material is produced.

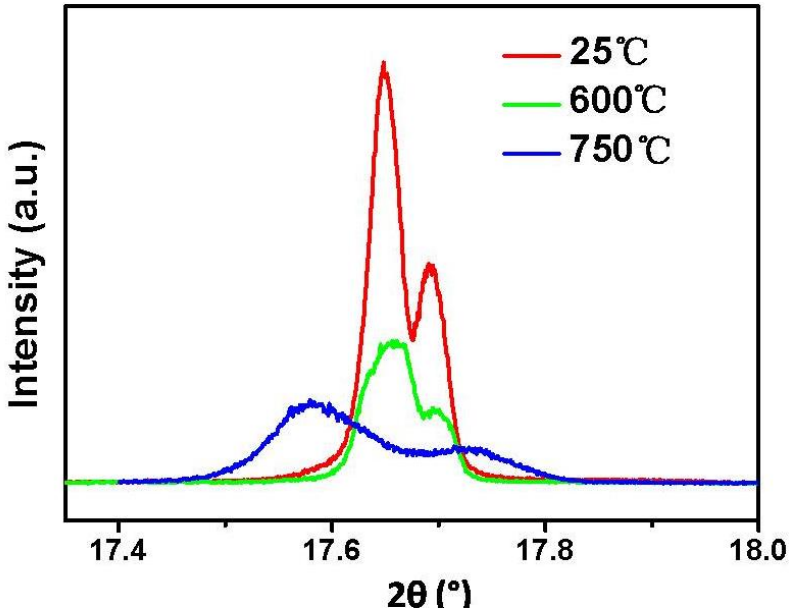

Figure 6.3 XRD spectrum of (004) surface of Mica substrate upon heating in different temperature for 2 hrs.

The property of mica sets temperature limit for success synthesis of ion intercalated metal oxide nano-structure. As discussed in Chapter 3, the surface melting temperature of mica determines the inferior temperature limit, since metal oxide vapour should react with melted mica to form ion intercalated structure. The structure stability upon heating sets the superior temperature limit, for the layered structure of mica will be destroyed upon high temperature treating, which blocks the K ion diffusion between layers.

6.3 Characterization of K ion intercalated WO_3 Nanobundle

After the synthesis process described above, the ceramic boat is cooled down to room temperature, and nanostructures on mica substrate are transferred for further characterization. These characterization methods include morphology characterization by SEM, elemental composition and chemical state detection by EDX and XPS, lattice structure determination by TEM and XRD.

Characterization 1: Morphology

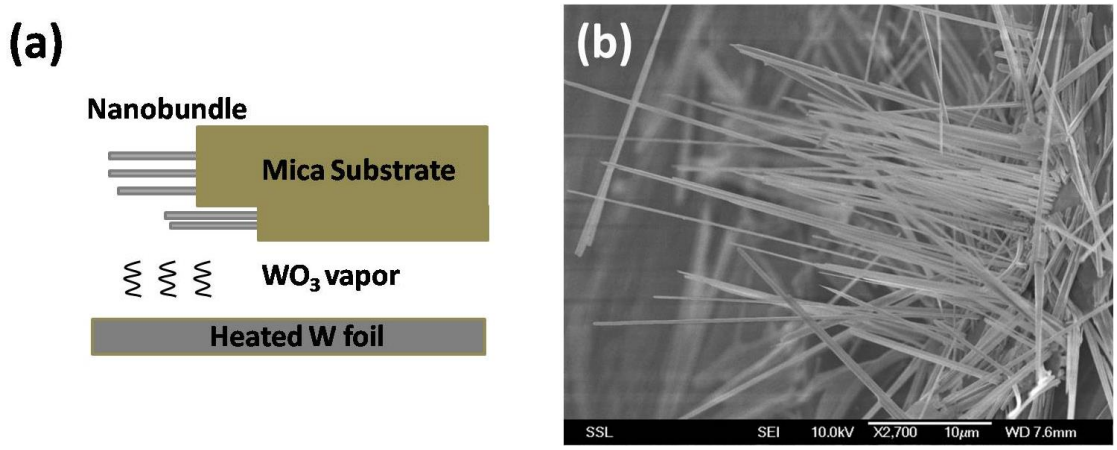

Figure 6.4 (a) Schematic of the position nanobundles grow (b) Top view SEM image displays nanobundle grown on the cleavage of mica substrate.

The deposition of the oxidized W yields nanobundles on the cleavage of mica substrate, including the edge of substrate and steps on the top surface, as shown by schematic image in Figure 6.4(a). Figure 6.4(b) displays the top view SEM image of edge of the mica substrate. These nanobundles extend out of cleavage with a length of 50~100 μm, a width of 500~700 nm and a thickness of 150~300 nm. Unlike K_xMoO_3 nanobundles that packed in bundles on the top surface of substrate, the K_xWO_3 nanobundles individually extend out of the cleavage. It should due to the low vapour concentration of tungsten oxide during the synthesis, the high activation energy on the steps and the presence of K ion channel on the cleavage surface. Thus, the amount of nanostructure at each growing point is quite small, and the K_xWO_3 nanobundle only extends out of the cleavage. These K_xWO_3 nanobundles vertically grow from the

cleavage, parallel with the layers of mica substrate, indicating the nanobundles adopt bottom up growth mechanism from the cleavage surface.

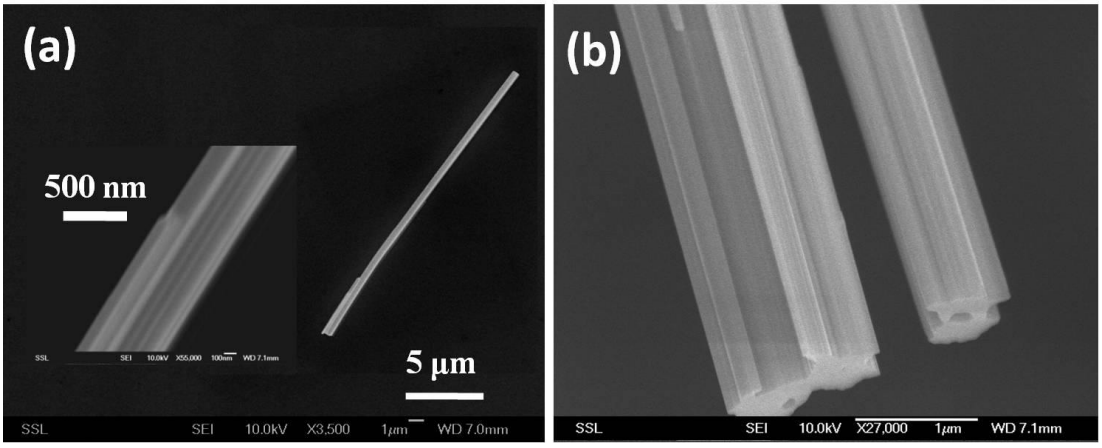

Figure 6.5 (a) Typical morphology of a single K_xWO_3 nanobundle. The inset image is a zoom in image of the left end of the nanobundle (b) Zoom in image of the end of nanobundle.

For further observation, individual nanobundle is transferred to Si substrate. Since the nanobundles are firmly attached to the substrate, only a segment of the nanobundle is transferred to Si substrate as shown in Figure 6.5(a) with the length, width and thickness of 21 μm, 550 nm and 250 nm respectively. The inset, displays the enlarged image of the left end of the nanobundle, indicating that the nanobundle is constructed by several parallel nanobelts. These nanobelts are much thinner with a width and a thickness of approximately 100 nm and 80 nm. The nanobundle structure is observed in all wires, as the side view from the end shown in Figure 6.5(b). These smaller nanobelts are regularly packed into layers.

Characterization 2: Elemental Composition and Chemical States

These nanobundles are transferred to TEM grid for further elemental analysis by micro-probe-station under microscope. Figure 6.6 shows the EDX spectrum elemental analysis for an individual nanobundle in TEM. The Cu peaks come from TEM grid while the K, W and O peaks originate from the nanobundle. It reveals that tungsten oxide nanobundle contains a significant percentage of K atoms (denoted as K_xWO_3).

The K:W ratio in the K_xWO_3 complex is fixed in the same nanobundle but differs between different nanobundles with x ranging from 0.18 to 0.28.

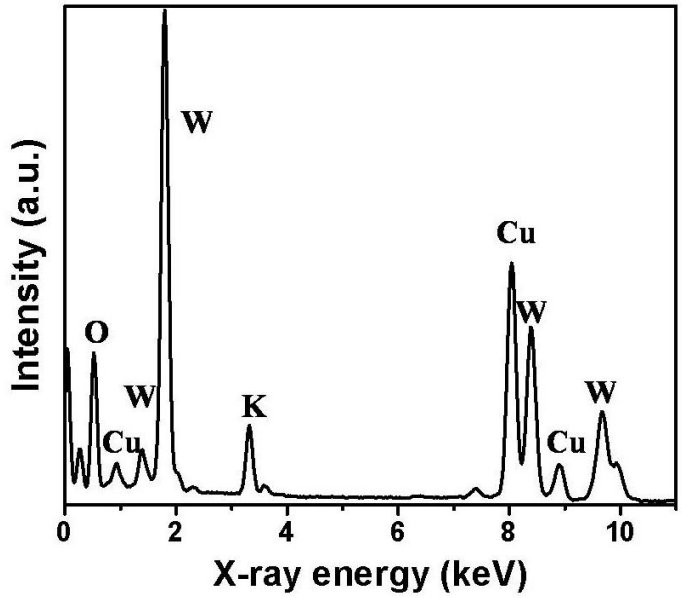

Figure 6.6 EDX spectrum of individual nanobundle on TEM grid.

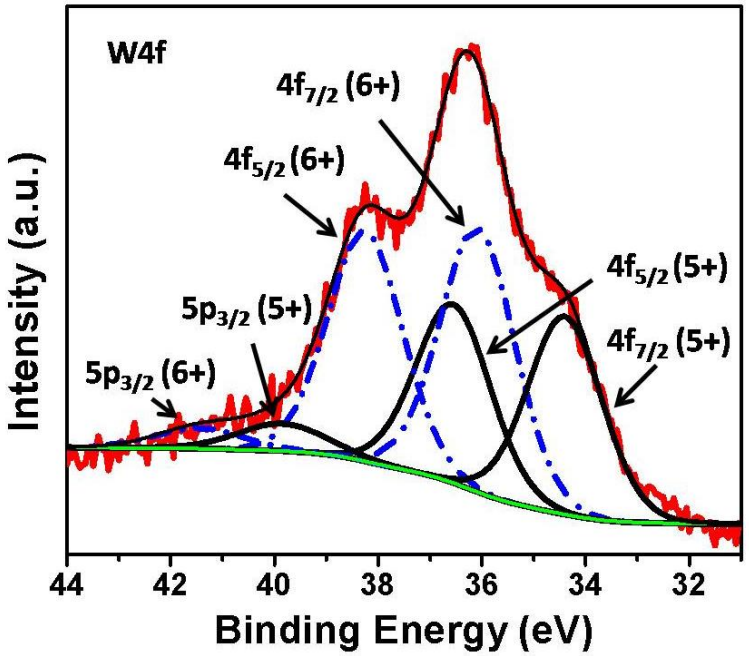

Figure 6.7 XPS spectrum of W4f peaks in nanobundle. The raw data (red curve) is fitted by W^{6+} peaks (blue dash curve) and W^{5+} peaks (black solid curve).

To further identify the material, XPS experiment is performed to measure the valence of W atoms in nanobundles. The energy distribution of W 4f photoelectrons is shown in Figure 6.7. The original data (red curve) is fitted by W^{6+} peaks (blue dash

curve) and W^{5+} peaks (black solid curve). The peaks at 36.1 eV, 38.2 eV and 42.0 eV represent emission from W $4f_{7/2}$, $4f_{5/2}$ and $5p_{3/2}$ levels from the W atoms in the 6+ oxidation state while the peaks at 34.4 eV, 36.6 eV and 40.2 eV come from W $4f_{7/2}$, $4f_{5/2}$ and $5p_{3/2}$ levels from the W atoms in the 5+ oxidation state.[121] The area ratio of W^{6+} over W^{5+} is around 4:3, revealing the valences of W is +5.57. For the most common K:W atomic percentage ratio found in individual nanobundles is ~0.23, the combined valencies of K and W is +5.80 in the material, considering the neutrality of the nanobundle, the stoichimetry of O is around 2.9, implying the existence of oxygen vacancies in the structure of WO_3.

Characterization 3: Lattice Structure

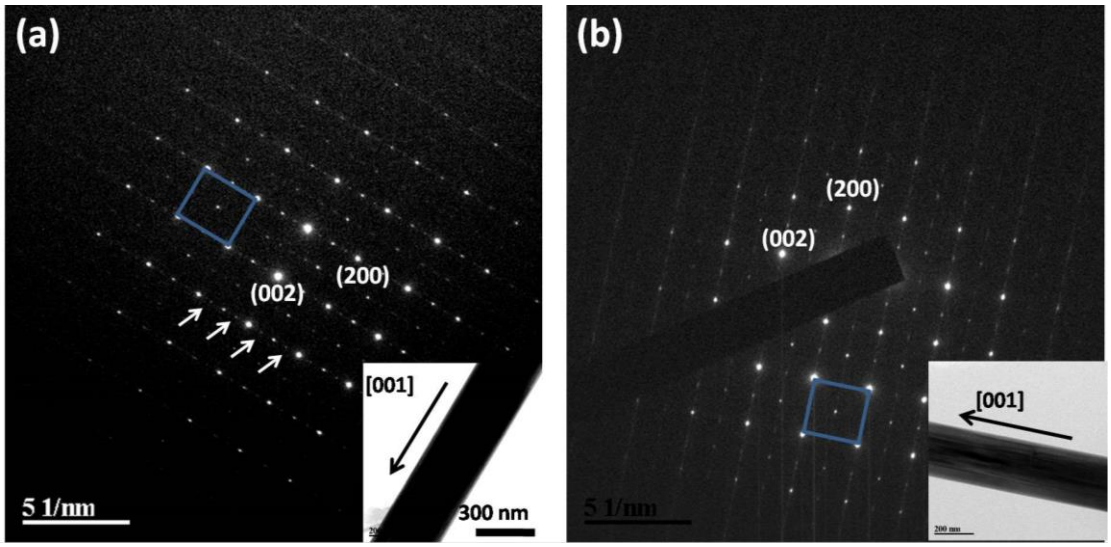

Figure 6.8 (a~b) Electron diffraction pattern of the K_xWO_3 nanobundle along [010] zone axis, the highlighted blue rectangle formed by large bright spots represents the lattice structure of the K intercalated WO_3. The inset image shows a TEM image of the typical K_xWO_3 nanobundle growing in the [001] direction.

To characterize the structure of the complex, the selected area electron diffraction (SAED) pattern of the K_xWO_3 nanobundles on the (010) surface is shown in Figure 6.8(a) with the inset image displaying a low-magnification TEM image of the nanobundle along the [001] growth direction. The nanobundle exhibits pseudo-rectangular diffraction pattern with $\beta=90.37\pm0.02°$ along the [010] zone axis highlighted by blue rectangle formed by large bright spots. It represents the WO_3

structure adopting a pseudo-orthorhombic configuration. Between every two bright spots, there is one weaker spot located in the middle along the [100] direction of the K_xWO_3 nanobundle indicated by white arrows. These smaller diffraction spots suggest that K_xWO_3 nanobundles possess a periodic superstructure with two primitive cells along the [100] direction. All nanobundles exhibit the same rectangular diffraction pattern, indicating the same pseudo-orthorhombic single crystalline structure in all wires. Figure 6.8(b) shows the diffraction pattern of another nanobundle. Rectangular diffraction pattern is observed, displayed by blue rectangle. Although the diffraction patterns are all the same, the distance between bright spots varies in different nanobundles, suggesting the different lattice constant in different nanobundles, which possibly induced by varied K ion concentration in nanobundles.

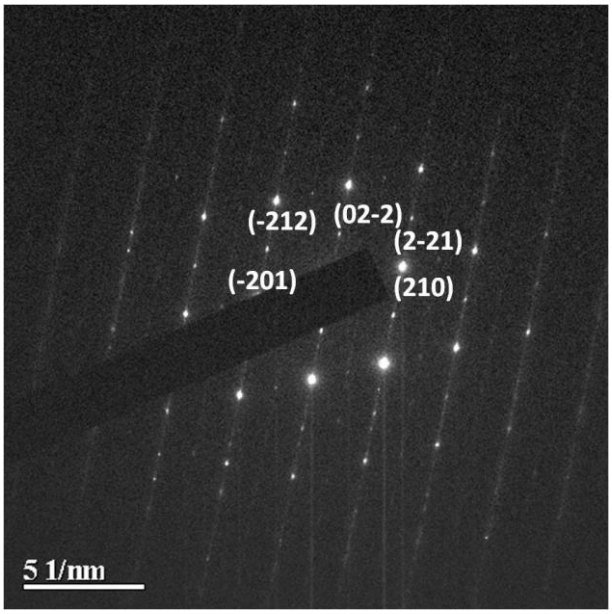

Figure 6.9 Electron diffraction pattern of the nanobundle along the [122] zone axis.

Since the diffraction pattern along the [010] zone axis only provides the structure information along *a*- and *c*- axes, the diffraction pattern along other zone axis is also captured to achieve lattice information along *b*-axis. Figure 6.9 shows the SAED pattern of the nanobundle along [122] zone axis, the diffraction pattern is similar with the projection of pseudo-orthorhombic structure along [122] zone axis. With the help of diffraction patterns along [010] and [122] zone axis, lattice constants of each individual nanobundle can be derived.

Table 6.1 The measured lattice constants of WO_3 powder and K_xWO_3 nanobundle.

		a(Å)	*b*(Å)	*c*(Å)
WO_3	Exp.	7.40	7.60	7.79
	Rep.[126]	7.39	7.57	7.79
K_xWO_3	X=0.18[a]	7.44	7.45	7.79
	Average[b]	7.58	7.32	7.81
	X=0.28[c]	7.63	7.15	7.83

The data in [a] and [c] is calculated from TEM diffraction pattern, the data in [b] is calculated from XRD peaks with x around 0.23.

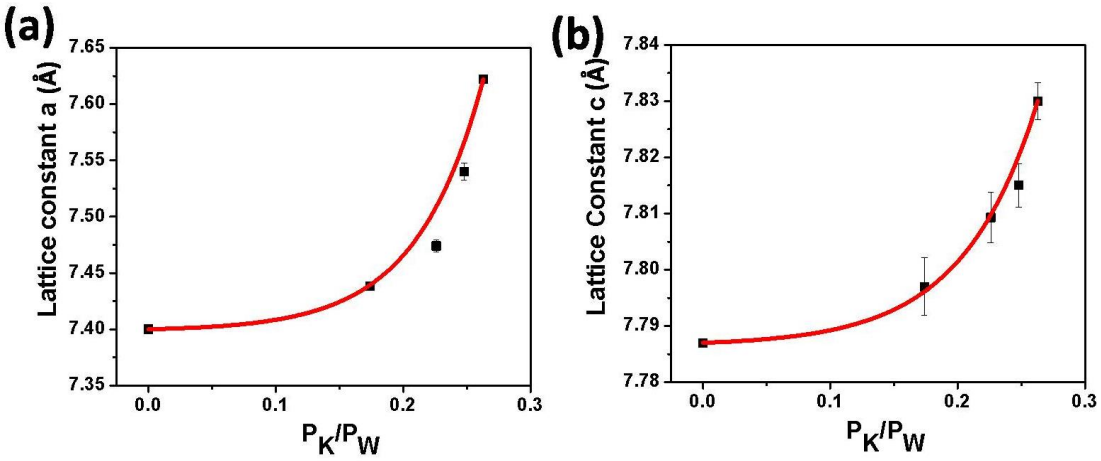

Figure 6.10 Lattice constant (a) *a* and (b) *c* at various atomic percentage ratio of K over W.

Upon the considerable uptake of K atoms in the WO_3 structure, the pseudo-orthorhombic structure preserves with the expansion of *a*- *c*- axes and contraction of *b*-axis. Table 6.1 presents the lattice constant of individual K_xWO_3 nanobundles with varied K concentration. As the K content in the lattice increases, the atomic percentage ratio of K over W (x) increases from 0.18 to 0.28, the lattice constant *a* increases from 7.44 Å to 7.63 Å, *c*-axis expands a bit from 7.79 Å to 7.83 Å and *b*-axis contracts from 7.45 Å to 7.15 Å. Lattice constant *a* and *c* under different atomic percentage of K are systematically studied as shown in Figure 6.10(a) and (b) respectively. Black squares present the calculated lattice constant, and these data points are exponential fitted shown by the red curves. The curve displays that both lattice constant *a* and *c* expand exponentially with the amount of K ions inserted, but to a different degree. It is noted that upon significant amount of K insertion (x=0.28), the

nanobundle maintains well aligned pseudo-orthorhombic single crystalline structure as displayed by SAED patterns. The transferred nanobundles are easily placed on the TEM grid with [010] direction perpendicular to the grid, it is hard to tilt the nanobundle to the suitable angle to achieve same diffraction pattern that contains information along the [010] direction for all nanobundles. Thus, the lattice constant *b* at various K concentrations is not systematically studied.

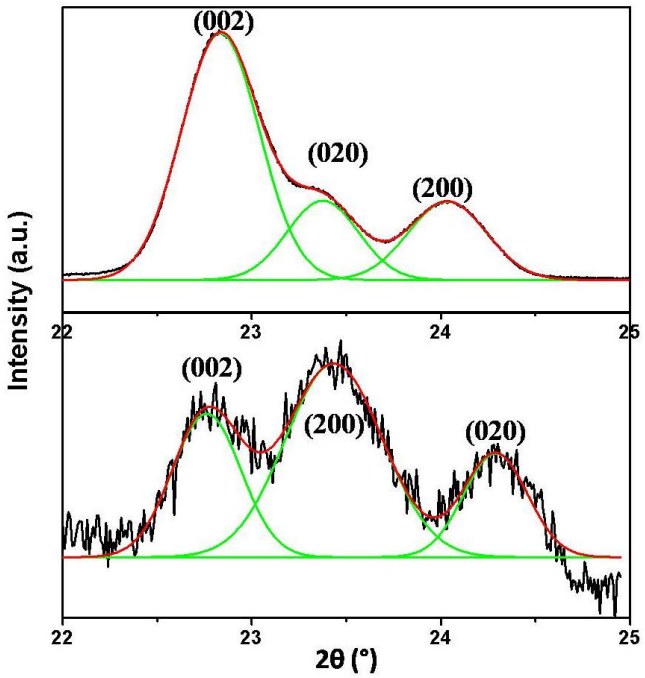

Figure 6.11 XRD spectrum of WO_3 powder (upper curve) and K_xWO_3 nanobundles (lower curve).

Similar with the synthesis of K_xMoO_3 nanobundle, the K_xWO_3 nanobundle grows by the evaporated oxidized tungsten vapour reacting with cleavage surface of mica to form K_xWO_3 complex. With the continuous adsorption of WO_3 vapour and K ions from mica substrate, K_xWO_3 becomes oversaturated on the cleavage surface and K_xWO_3 nanobundle nucleates out of the surface in the preferred direction. According to the described growth mechanism, the structure of K_xWO_3 should be related to the initial WO_3 powder where the oxidized tungsten vapour comes from. During synthesis procedure, the W foil is gradually oxidized and turns into yellow-green WO_3 powders. The structure of these yellow-green WO_3 powders suggests the structure of K_xWO_3 with x=0. The X-ray diffraction is utilized to identify the structure of powder. Upper

curve of Figure 6.11 shows the powder exhibits orthorhombic structure of WO_3 with lattice constant *a* =7.40 Å, *b* = 7.60 Å and *c* =7.79 Å, the values are consistent with the reported result (for better comparison, the experimental result and report result are list in Table 6.1).[126] These values contribute to the first data points in Figure 6.10, which display the lattice constant of K_xWO_3 without K insertion.

The K_xWO_3 nanobundles are also studied by XRD and the lower curve in Figure 6.11 shows the structure of nanobundles. According to the structure of WO_3, these three peaks denoting the (200), (020), (002) surfaces. From peak position, lattice constants of 7.81 Å, 7.58 Å, 7.32 Å are calculated corresponding to the peaks from left to right. Since the averaged K:W atomic percentage ratio measured by large scale EDX measurement is ~0.23 and the trend shown in Figure 6.10 suggest the averaged lattice constant should lie between the maximum and minimum value, three peaks are thus identified as (002), (200), (020) peaks respectively and the lattice constants determined are list in Table 6.1. The significant peaks confirm the pseudo-orthorhombic structure of the nanobundle analysed above. Compared with the fitting curve in Figure 6.10, the values of lattice constant *a*=7.58 Å and *c*=7.81 Å in the curve denoting the atomic percentage ratio of K over W is around 0.23, which is consistent with the measurement by EDX.

According to previously reported formation of intercalated WO_3 and reduced WO_3, phase transition is observed to occur upon intercalation or chemical reduction. In these reported works, the monoclinic structure of WO_3 upon intercalation proceeds to higher symmetry. In Li_xWO_3 for example, this occurs initially by a phase transition to a tetragonal phase with x ~0.1 and later by phase transition to a cubic phase when x~0.36.[117, 118] Upon chemical reduction, the structure of WO_3 changes by crystal shear mechanism, where groups of edge sharing WO_6 octahedra are rearranged along some crystallographic planes.[119-121] In the case of tungsten oxide with similar stoichiometry $W_{20}O_{58}$, WO_6 octahedras are rearranged with crystal shear planes along (103) direction

and the unit cell (monoclinic) is enlarged with a =12.1 Å, b =3.78 Å and c =23.4 Å.[127] These phase transitions are however not observed in our K_xWO_3 nanobundles, the pseudo-orthorhombic structure is preserved even with intercalation of great amount of K atoms and chemical reduction of WO_3.

We have effectively grow K intercalated WO_3 nanobundles by thermal evaporation method on muscovite mica substrate. With the help of various experimental characterization techniques, we find that the pseudo-orthorhombic lattice structure and the layered structure remaining essentially intact upon K ion insertion. Considering the great amount of large size ion insertion (1.5 Å in size and ~0.23 in atomic ratio), the deformation in the lattice is amazingly small. Compared with K_xMoO_3, the lattice deformation in K_xWO_3 is different with the contraction in b axis, while we naturally assume that ion insertion leads to layer expansion. It is possibly due to the different atomic bonding process.

6.4 Electrical Properties of K_xWO_3 Nanobundle

Electrical Conductivity at Room Temperature

Alkali ion insertion would enhance the conductivity of the material. For electrical property measurement, individual nanobundle electrode device is next fabricated in the same process described in Chapter 2. Individual nanobundle is transferred from the growth substrate to SiO_2/Si substrate and photolithography method is utilized to achieve designed metal (Au(400 nm)/Cr(10 nm)) finger electrodes (of gap ~15 μm) that make contact with the nanobundle. Figure 6.12 displays the SEM image of an individual K_xWO_3 nanobundle contacted by electrodes. The electrical measurements are carried out using Keithley 6430 source-measure unit.

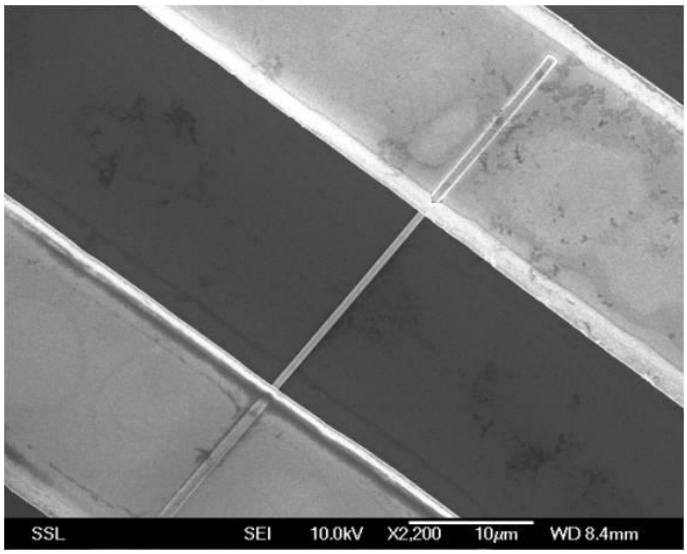

Figure 6.12 SEM image of individual nanobundle contacted by electrodes.

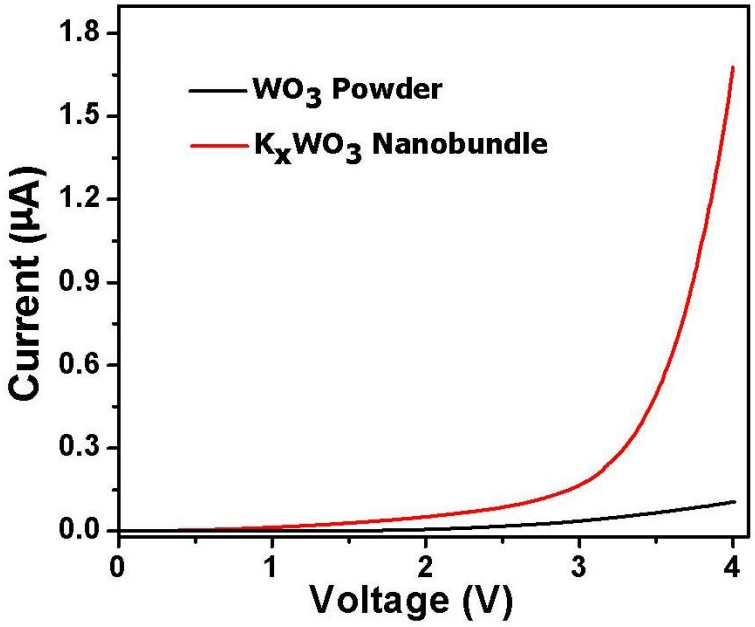

Figure 6.13 I-V curves of WO_3 powder (black) and individual K_xWO_3 nanobundle (red).

As a comparison, as-grown WO_3 powder is compressed and deposited on similar electrode pattern on SiO_2/Si substrate, the measured current is on the order of ca. 100 nA at ca. 4 V, as shown in black curve in Figure 6.13. From the effective length of electrode (100 μm), separation between electrodes (15 μm) and thickness of the powder, we estimate the electric conductivity of the WO_3 powder to be 10^{-4} S m^{-1},

consistent with the reported value of WO_3 film.[128] For the K_xWO_3 nanobundle, at room temperature, the measured current is 1.7 μA at a bias of 4 V (red curve in Figure 6.13). From the measured effective length and cross section of the nanobundle, the electric conductivity is estimated to be 40 S m^{-1}. It is remarkable that the electrical conductivity is enhanced substantially by 5 orders of magnitude from 10^{-4} S m^{-1} of the WO_3 powder to 40 S m^{-1} of the K_xWO_3 nanobundle. The I-V curve displays typical semiconductor behaviour of two materials.

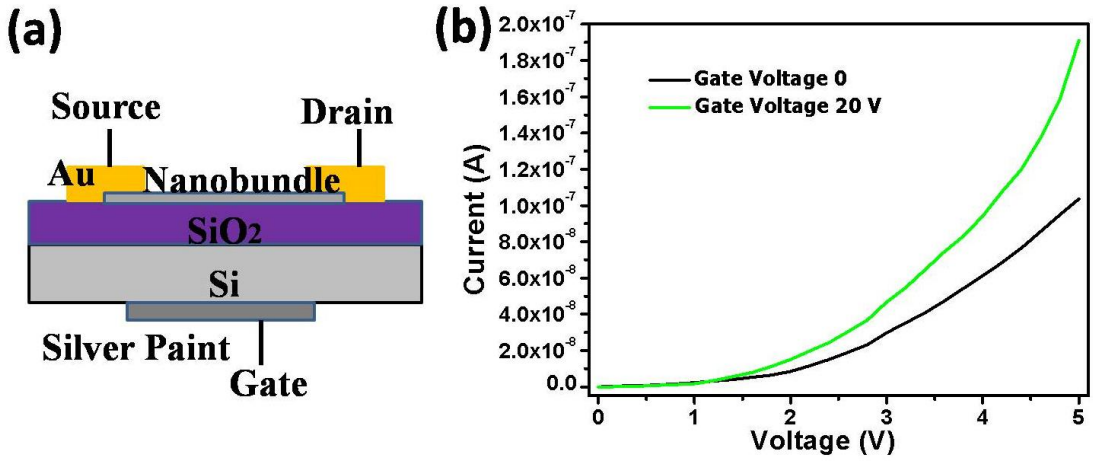

Figure 6.14 (a) Schematic setup of FET device (b) Current (I_{sd}) versus source drain voltage (V_{sd}) curves recorded at different gate voltages (0, +20 V) for the device shown in (a).

For FET measurement, the bottom of the device is scratched to remove the SiO_2 layer, and silver paint is plastered on the bottom of it. Gate voltage is applied from the bottom and the surface electrodes act as source and drain (Figure 6.14(a)). The current between source and drain I_{sd} versus source drain voltage V_{sd} at different gate voltage is displayed in Figure 6.14(b). Clearly that I_{sd} increases as gate voltage increases. The performance denotes the K_xWO_3 nanobundles exhibit n-type semiconductor behaviour with electrons as charge carriers.

Temperature Dependent Electrical Conductivity

To study the temperature effect on the conductivity, the device is mounted on the heating stage to systematically control the temperature of nanobundle. The inset

schematic image in Figure 6.15 displays the set up. The conductivity of the K_xWO_3 nanobundles increases rapidly upon heating as shown in Figure 6.15. At the bias of 4 V, the current increases from 0.7 μA to 140 μA as the temperature increases from 23 ℃ to 200 ℃, raising the conductivity by 200 times from 40 to 8000 S m^{-1}. The significant thermal enhanced conductivity suggests great amount of electrons are excited by thermal energy, and it indicates the small band gap of the nanobundle.

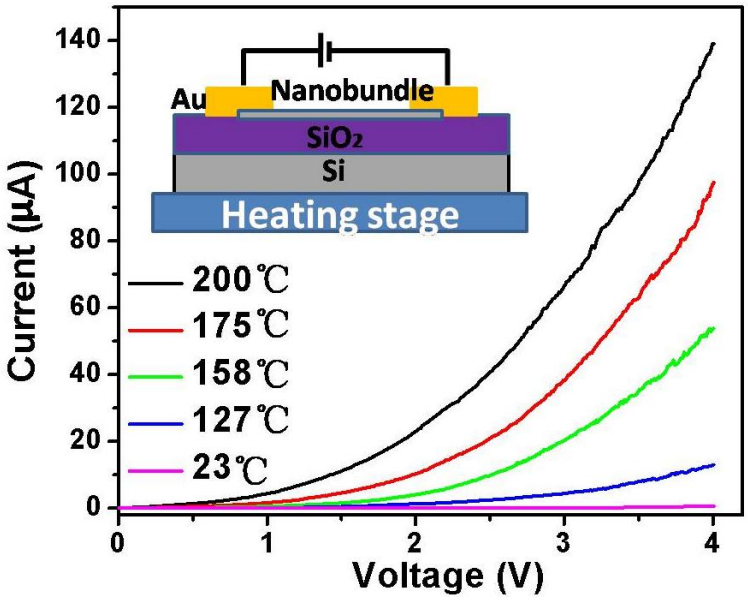

Figure 6.15 I-V curves of K_xWO_3 nanobundle at different temperatures. Inset image shows the set up.

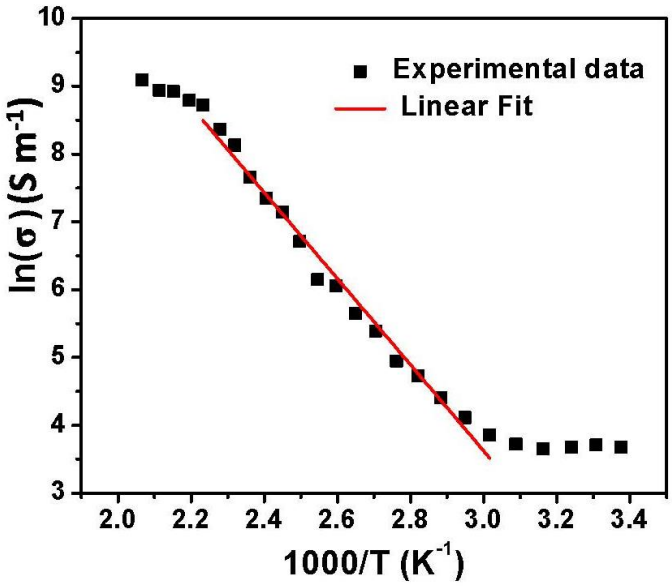

Figure 6.16 Temperature dependence conductivity of the nanobundle in log scale at voltage of 4 V.

Subsequently, the conductivity at voltage of 4 V as a function of reciprocal of temperature is plotted on a log scale as shown in Figure 6.16. Two kinks in the curve are clearly observed at 331 K and 448 K. At the temperature below 331 K, conductivity does not change significantly. As temperature increases from 331 K to 448 K, the log scale of conductivity varies linearly with reciprocal of temperature. In this region, electron conductivity increases exponentially with reciprocal of temperature. According to $\sigma=ne\mu$, where σ is the conductivity of nanobundle, μ is the mobility of electrons, n is the electron density, the mobility in the region does not vary significantly due to relatively low electron density. The electron conductivity is thus determined by electron density. And the variation of σ with temperature in this linear range can be attributed to the change of electron density with temperature. Base on the thermally activated transport model,[62, 63] $\ln(n) = \ln(n_0) - W/2kT$, where n is the electron density, n_0 is the density value when T is infinity, k is the Boltzmann constant and W is the thermal activation energy. The thermal activation energy is determined to be around 1 eV based on the slope of a linear fit to the data (Figure 6.16). The value suggests the energy required to thermally excite localized electrons to conduction band. The effect of phonon scattering increases for thermally excited lattice atoms and the effect becomes more prominent at high temperature due to sufficient high electron density. Consequently, above 448 K, the slope of conductivity decreases due to the decreasing mobility induced by significant phonon scattering.

6.5 Theoretical Simulation of Lattice Structure and Band Structure

To interpret the significantly enhanced conductivity, we perform density functional theory calculations to understand the structural and electronic properties of the pure and K-intercalated WO_3 materials. Since the thicknesses and widths of the WO_3 powders and the K_xWO_3 nanobundles are several orders of magnitude larger than

the size of atoms, we employ a 3-dimensional periodic bulk-like structure to model the present system. A 2×1×1 supercell of the pseudo-orthorhombic WO_3 primitive lattice containing 16 W atoms and 48 O atoms (Figure 6.17(a)) is first selected to model the pure WO_3 powder. The fully optimized lattice of the WO_3 supercell, with the lattice constants a =7.45 Å, b = 7.65 Å and c =7.76 Å are in well agreement with the experimental data shown above and the reported XRD data,[126] suggesting that our computational method is reliable for predicting structural information of the materials we deal with.

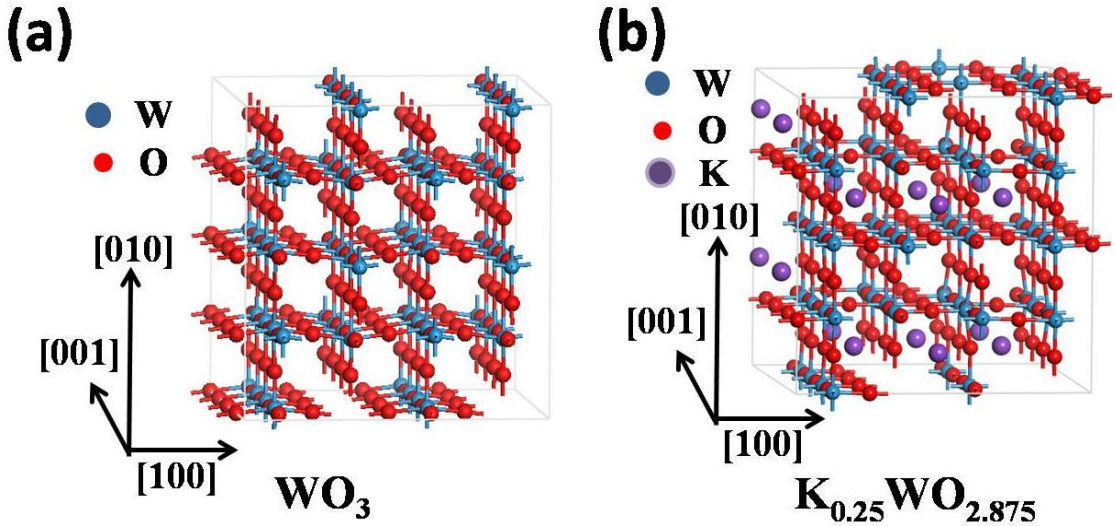

Figure 6.17 Atomic structure of (a) WO_3 and (b) $K_{0.25}WO_{2.875}$.

Based on the stoichiometry of nanobundle, we substitute two O atoms with K atoms and place two K atoms as intercalants in the supercell. The optimized structure of $K_{0.25}WO_{2.875}$ in Figure 6.17(b) shows that, either as intercalants or occupants, K atoms finally relocate to the tunnel along [001] direction of the cell, where each K atom is encapsulated by 3 or 4 adjacent O atoms. The oxygen vacancies lead to slight distortion of the lattice, while the inserted K atoms cause an expansion of 0.2 Å along the *a*-axis, which is in good agreement with experimental observation.

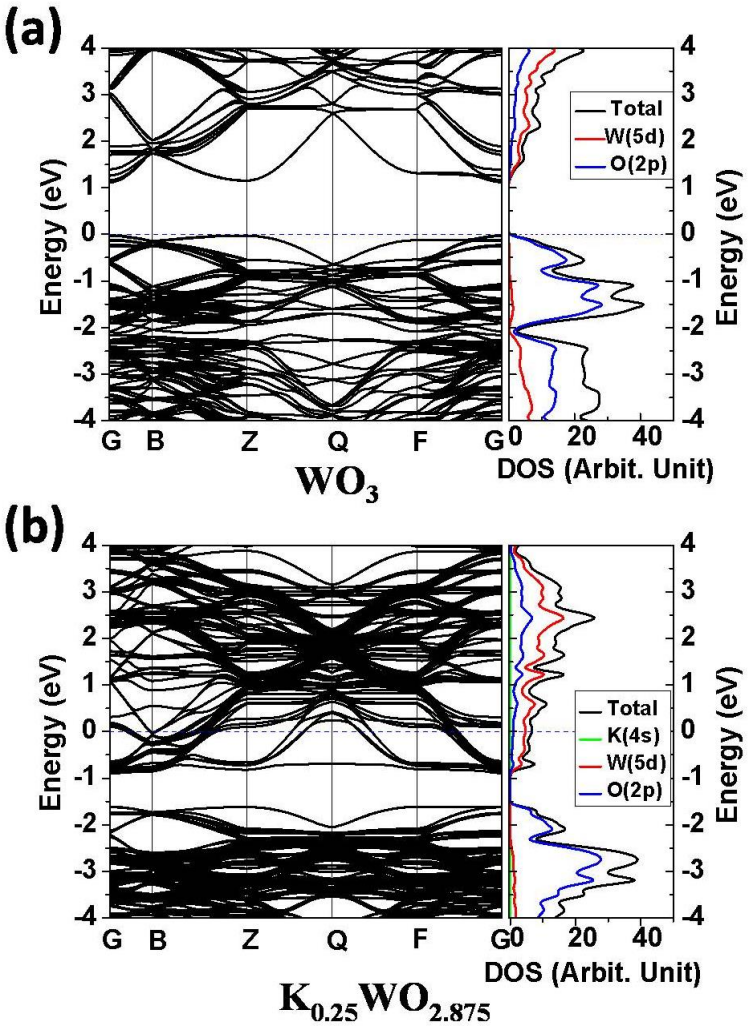

Figure 6.18 The calculated band structure and the density of states (DOS) of (a) WO_3 and (b) $K_{0.25}WO_{2.875}$.

The electronic structures of pseudo-orthorhombic WO_3 and K_xWO_3 are calculated based on the optimized structure. The band structure and density of states of WO_3 are displayed in Figure 6.18(a). The valence band is largely dominated by the *2p* orbitals of oxygen, while the conduction band consists of chiefly the *5d* states of tungsten with a significant contribution from the *2p* states of oxygen. This calculated band structure of pseudo-orthorhombic WO_3 with a direct band gap ~ 1.2 eV is consistent with other reports.[129] The band structure of the $K_{0.25}WO_{2.875}$ lattice is depicted in Figure 6.18(b). Upon potassium uptake in the lattice, the electronic structure undergoes a substantial change due to the charge transfer from potassium to tungsten, which forces electrons to populate the conduction band. The projected density of states (PDOS) for the K-*4s* and W-*5d* states indicates that K atoms are fully ionized and the adjacent W atoms are

accordingly reduced, which is consistent with the observation from XPS measurement that averaged valencies of W ion reduces from +6 to +5.57. Because of the strong overlap between the W-*5d* orbitals and the O-*2p* orbitals in the conduction band, the transferred electrons are populated and readily delocalized, thus, the electrical conductivity is significantly enhanced.

In the projected density of state of $K_{0.25}WO_{2.875}$ in Figure 6.18(b), the Fermi level (at 0 eV) is located in the conduction band and these electrons can easily be excited and delocalised to the higher energy states directly above upon heating as there are continuous available states in the conduction band (no gap). The excitation of these electrons to these states leaves unoccupied states, especially the ones near the bottom of conduction band. According to the band structure in Figure 6.18(b), the minimum energy to excite the valence electrons to the conduction band can be given by Conduction Band Minimum (CBM) – Valence Band Maximum (VBM) and it has a value of ~ 1 eV. Thus, the electrons in valence band require at least ~ 1 eV to be excited to these unoccupied states in conduction band to contribute to the measured current. Consequently, at relatively low temperature due to the insufficient thermal energy provided, electrons in valence band could not be excited to conduction band to increase the current density. As a result, below 331 K, the conductivity does not change with temperature as shown in Figure 6.16. When sufficient energy is provided, the localized electrons in valence band can be excited to the unoccupied states in conduction band and contribute to the conductivity. As such the electrical conductivity is greatly enhanced above 331K. Notably, the gap of ~1eV is close to the thermal activation energy for electrical conductivity shown in Figure 6.16.

6.6 Photoelectrical Response Measurement

The small activation energy of the material (~1 eV) implies the nanobundle is a viable candidate for the investigation of photon electrical response. Upon laser

illumination, localized electrons in nanobundle can be excited by photons and contribute to the current. The focused laser illumination system described in Chapter 2 is utilized to study the photon electrical response of K_xWO_3 nanobundle. The green laser beam (λ=532 nm) is directed into the microscope via mirrors. Inside the microscope, the laser beam is reflected by a beam splitter towards a 100X objective lens. The objective lens focuses the laser beam onto the device that is positioned on the translation stage. The individual nanobundle electrode is the same as the device for electrical measurement shown in Figure 6.12. Focused laser beam with spot size around 2 μm and power 2 mW is locally directed at specific locations on the nanobundle as shown in Figure 6.19. In location Ⅰ and Ⅲ, laser is focused on the left and right electrode-nanobundle junction respectively. In location Ⅱ, the spot lands on the middle of nanobundle.

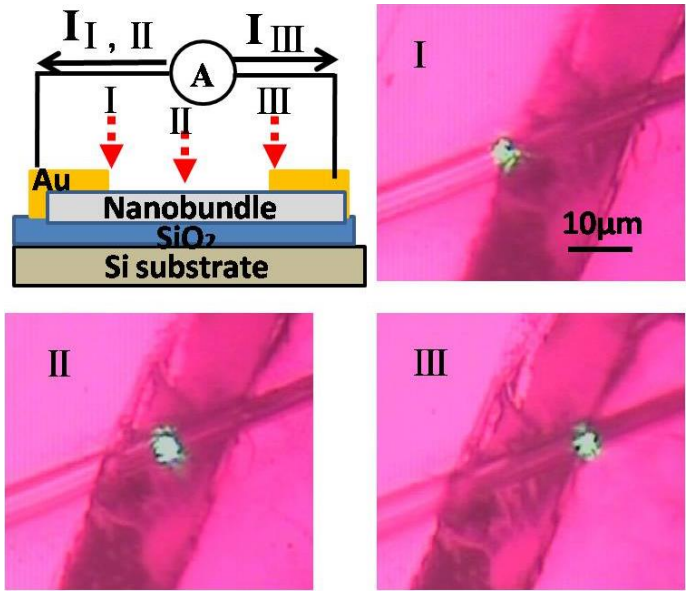

Figure 6.19 Schematic of focused laser beam locally irradiating at three different locations and three optical images showing the position of laser spot on nanobundle device.

Photon Induced Electrical Measurement

Figure 6.20 displays the measured current between electrodes when laser is directed at location Ⅰ without externally applied bias voltage. In the absence of laser beam irradiation, there is no current detected. The moment laser is present, current

increases to -9 nA within 50 ms. The current returns to 0 again when laser is blocked. It is noted that the photon induced current in the material is quite significant compared with other semiconductor nanomaterial with typical values ranging from ~10 pA to ~500 pA under similar laser power.[72, 77, 78] Since the size of laser spot (2 μm) is smaller than the gap between two electrodes (15 μm), the photon induced electrical measurement upon laser spot location could be subsequently systematically studied.

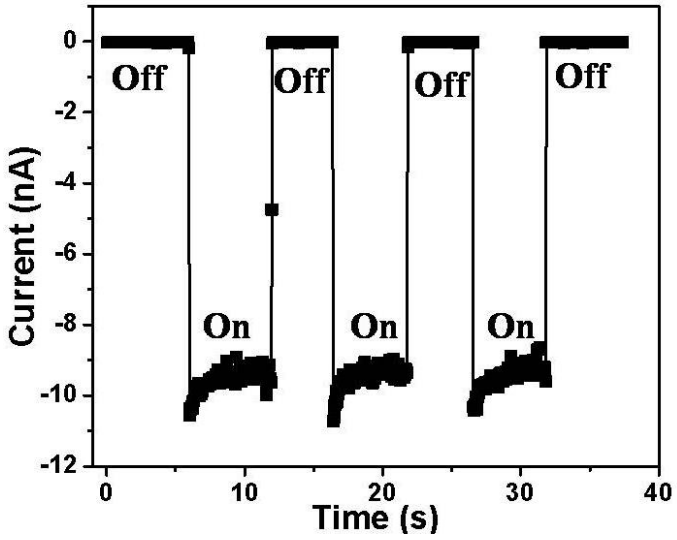

Figure 6.20 Photon induced current measured when laser spot is directed at location Ⅰ without externally applied bias voltage.

Focused laser beam is directed at different locations and the corresponding photon induced current is measured as shown in Figure 6.21. The distance indicated in the horizontal axis is measured with respect to the center of the nanobundle. The two broken lines denote the edge of electrodes and the nanobundle lies between two lines. Here we observe surprising photocurrent results at zero external bias. The photocurrent response exhibits an opposite polarity when the laser beam is focused at two different nanobundle-metal junctions. As focused laser spot moves from left junction to the center, the amplitude of photon induced current decreases gradually. When the focused laser beam is directed at the middle of the nanobundle, negligible photocurrent is observed. As the laser spot further move rightward, the polarity of photon induced current reverses and the amplitude gradually increases. The value achieves maximum

at the nanobundle-metal junction. When the laser spot moves from junction toward electrode, the amplitude of photon induced current gradually decreases.

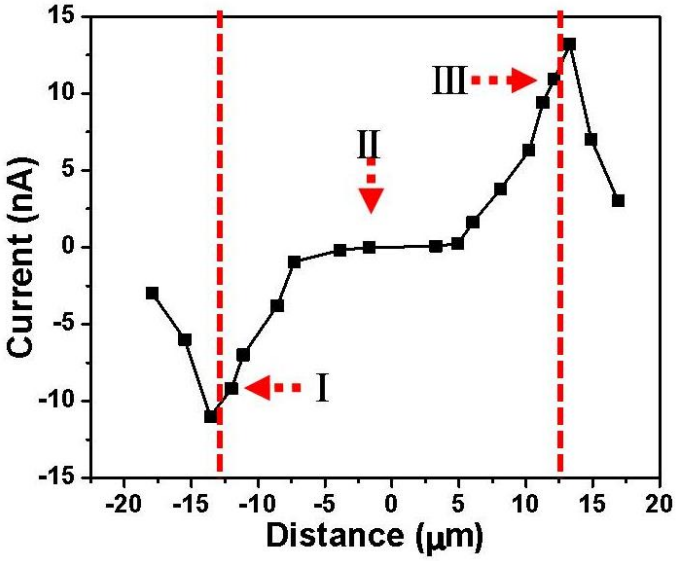

Figure 6.21 Photon induced current at different distance between center of laser spot and center of nanobundle at zero bias. Two red broken lines denote the edge of electrode and the nanobundle lies between two lines.

The observed properties of the photocurrent can be interpreted by considering the nanobundle-gold system as a back-to-back Schottky diode model. Observations made in Figure 6.21 can be attributed to the properties of the Schottky barrier formed at the nanobundle-gold contacts. Shining of laser may facilitate an increase in the photon generated electrons to travel from nanobundles to the gold contact and give rise to the photocurrent. When the laser is shone onto the other contact, similar process occurs but the polarity of the photocurrent is reversed. When the laser is shone on the middle of the nanobundle, the charge carriers do not have sufficient energy to diffuse across the nanobundle and many are lost through recombination and scattering. Thus the photocurrent with laser shining on the middle of the nanobundle is found to be negligible. Similar observation is made in the case of Nb_2O_5 nanowires. [77, 78] In addition, the localized thermal heating caused by the focused laser can give rise to thermoelectric effect at the nanobundle-gold interface. This effect can give rise to net diffusion of electrons from the nanobundle to the gold electrode at the junction.

Similarly, the thermal effect will prompt electrons diffusion in opposite directions when shining the laser on the two junctions.

Photon Enhanced Electrical Measurement

When external bias voltage is applied, under laser illumination, localized electrons are excited by photons and enhance the current. The set-up is shown in the inset image in Figure 6.22. The measured current between electrodes when laser is shone at location Ⅱ with an external applied bias voltage of 4V is displayed by the curve in Figure 6.22. When laser is blocked, current is around 1.42 μA. The moment laser is switched on, current increases to 1.82 μA in 12 s. The current drops to 1.42 μA again when laser is turned off. The current increases rapidly at the beginning (0.2μA in the first second) denoting that part of the excited electrons are originated from photon excitation, and the current further increases slowly (0.2 μA in the following 10 s) suggesting that part of excited electrons are originated from thermal effect.[78]

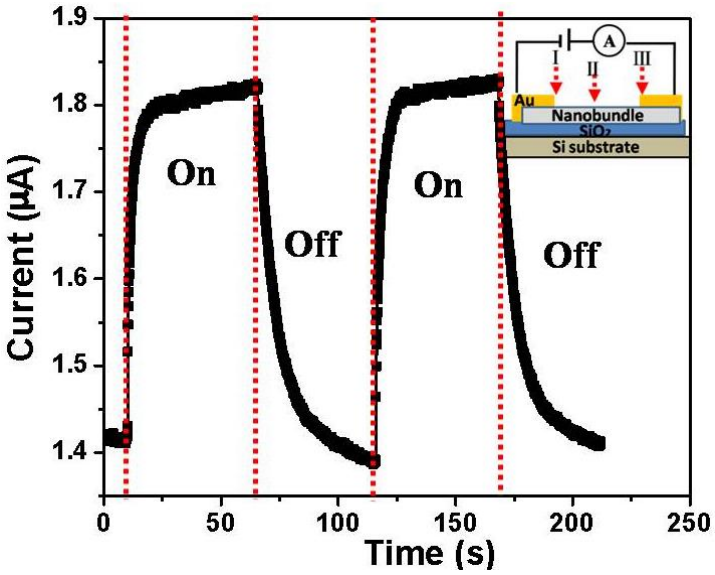

Figure 6.22 Photocurrent measured under external bias voltage of 4 V with laser spot directed at location Ⅱ on the nanobundle device. Inset shows schematic of focused laser beam locally irradiating at three different locations under external bias.

The photon enhanced electrical measurement upon laser spot location is further systematically studied. Focused laser is directed at different locations, the distance is measured with respect to the center of nanobundle, and the corresponding photon

enhanced current under external bias voltage of 4 V is detected as shown in Figure 6.23. The two red broken lines denotes the edge of two electrodes and nanobundle lies between them. In the curve, the two highest amplitudes take place when laser spot is shone on the electrode-nanobundle junction (location Ⅰ & Ⅲ). The amplitude gradually decreases a bit as laser spot moves to the center. When the laser spot lands on the middle part of nanobundle (from -10 μm to 10 μm), the values of current at every spots is almost the same. When laser spot is directed at location Ⅱ, only nanobundle contributes to the change of current. As shown in Figure 6.23, the current is enhanced by 0.4 μA. It suggests that significant amount of electrons are excited by the focused laser beam originated from nanobundle itself. In the center part of the nanobundle, the amplitude of enhanced current is almost the same. It suggests that the scattering and recombination of photon excited electrons under external bias is not significant. The enhanced amplitudes of photon current at both junctions are higher than the value in the center of nanobundle. The higher amplitude should due to the combined effects of photon excited electrons from nanobundle itself and nanobundle-electrode junction.

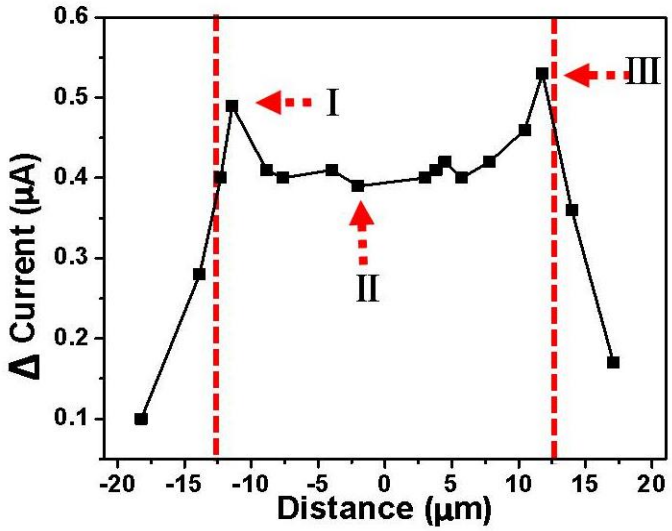

Figure 6.23 The Photon enhanced current at different distance between center of laser spot and center of nanobundle under external bias voltage of 4 V.

As discussed above, low energy is required for localized electrons to be excited to conduction band and contribute to the current. The difference between zero applied bias and non-zero applied bias is that with applied bias, the additional charge carriers can be

readily driven across the nanobundle and this gives rise to increase current. Regardless of where the laser is focused on the nanobundle, the photon generated charge carriers will be driven along the nanobundle in same direction. As a result, the polarity and amplitudes of enhanced current are similar as laser spot moves from left to right in Figure 6.23. Moreover, it should also be noted that the magnitude of the photocurrent with applied bias is much higher than the photocurrent obtained under zero bias. The external bias can readily overcome the mutual attraction between the electron-holes pair, separate and collect the charge carriers and this contributing to the higher photocurrent.

6.7 Comparison with K_xMoO_3 nanobundle

The same method is used to synthesis K_xMoO_3 and K_xWO_3 nanobundle. There are many similarities between these two materials, such as the similar amount of K ions being inserted, the preserved lattice structure, the nanobundle configuration, the high conductivity and photo-electrical response. However, there are many differences between them. Further investigation about the differences could reveal more insight about the growth mechanism and properties induced by ion insertion. Three main differences are discussed here, including the differences in growth orientation, lattice expansion and photoelectrical response.

Growth orientation: Most of K_xMoO_3 nanobundles extend out of the surface in certain degree and many nanobundles are packed together on the substrate as displayed in Figure 6.24(a). While most of K_xWO_3 nanobundles extend out vertically from the cleavage surface of mica substrate and each nanobundles separate from each other as shown in Figure 6.24(b). The different amount of nanobundles should due to the different melting points of MoO_3 and WO_3. The melting point of WO_3 (1473 ℃)[123] is greatly higher than that of MoO_3 (795 ℃)[124], the concentration of WO_3 surface vapour is thus significantly lower than MoO_3 vapour during synthesis. It results in the

low concentration of WO_3 nanobundles. However, the reason of different growth orientation of these two materials is not understood yet. Further research about the difference could provide insight about the growth mechanism of K ion intercalated nanostructure.

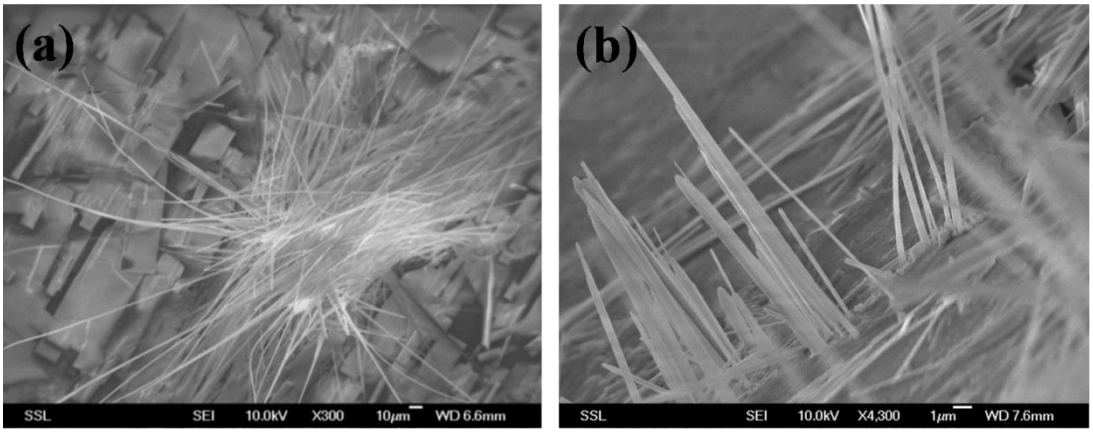

Figure 6.24 The morphology of mica substrate after the growth of (a) K_xMoO_3 nanobundle (b) K_xWO_3 nanobundle.

Lattice expansion: These two materials perform different lattice expansion as well. Upon 25% K ion intercalation, MoO_3 expands in *b* and *c* axes for ~0.3 Å, and shrinks in *a* axis ~0.3 Å . WO_3 expands in *a* axis ~0.2 Å and *c* axis ~0.02 Å, and shrinks in *b* axis ~0.4 Å. Meanwhile, the lattice variation trend in two materials are different. In K_xMoO_3, lattice constant *a* decreases linearly with the concentration of K ions as shown in Figure 6.25(a), while in K_xWO_3, lattice constant *a* changes exponentially with the concentration of K ions as shown in Figure 6.25(b). The different expansion direction and different variation trends in two materials possibly due to the different structure of MoO_3 and WO_3 and the different way K ions being intercalated in these two materials. Further theoretical simulation about it possibly reveal the atomic dynamics in lattice during ion insertion.

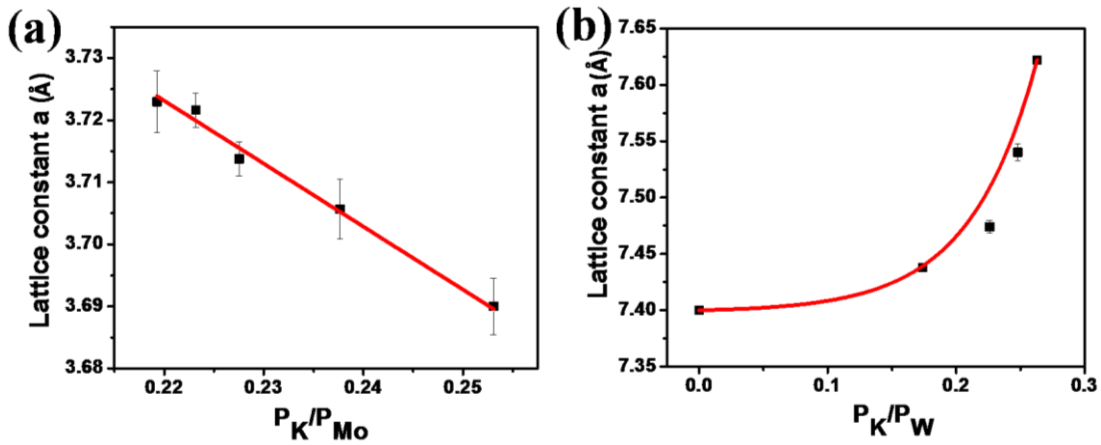

Figure 6.25 The lattice constant *a* under different atomic percentage ratio of (a) K over Mo in K_xMoO_3 nanobundle (b) K over W in K_xWO_3 nanobundle.

Photo-electrical response: Although both materials show photo-electrical response, the laser spot location dependent behaviours are different. In K_xMoO_3 nanobundle, the maximum laser induced photocurrent and laser enhanced photocurrent appears when laser spot fully lands on the nanobundle (shown in Figure 4.12, Figure 4.17). While in K_xWO_3, the maximum value appears when laser spot lands on the metal-semiconductor junction (shown in Figure 6.21, Figure 6.23). The different behaviour should due to the different working functions of two materials. In K_xWO_3, the working function of the material is possibly lower than that of contact metal, and the metal-semiconductor Schottky barrier is established. Upon laser illumination, electrons in the semiconductor could be excited to metal over the barrier, and contribute to the current. Thus, the maximum photocurrent appears when laser is directed on the junction. While the working function of K_xMoO_3 is possibly higher than that of contact metal, thus, there is no Shottky barrier established and no photocurrent contribution from the junction. Obviously, the working function of MoO_3 and WO_3 are changed upon K ion insertion, but the values are different. Further theoretical calculation could reveal the mechanism of modifying working function by ion insertion.

6.8 Summary of Results

In summary, we have successfully synthesize K intercalated WO_3 nanobundles with the pseudo-orthorhombic structure remaining essentially intact by the simple method. The nanobundles adopt a bottom-up growth model via thermal evaporation to intercalate K atoms into the WO_3 lattice. Although great amount of K atoms are inserted, the lattice constant expand or contract in small amount and the pseudo-orthorhombic single crystalline lattice structure preserves. Compared with K_xMoO_3 nanobundle, the amount of ions being inserted, the morphology (nanobundle configuration) and lattice structure after ion insertion are similar. It suggests the same ion insertion process in both materials. The success ion intercalation illustrates that the method is applicable to intercalate ions in other metal oxide nanostructures.

Using individual nanobundle electrode device, we measure the I-V curves of the K_xWO_3 nanobundle. It is found that the material displays 5 orders higher electric conductivity than pure WO_3 and the conductivity further increases by 200 times at elevated temperature. Density functional theory is used to elucidate the structure of the K_xWO_3 and to understand the origin of the high conductivity behaviour of the material. The calculated band structure of the $K_{0.25}WO_{2.875}$ indicates the K atoms are fully ionized, giving rise to the reduction of the adjacent W atoms, which is consistent with the observation from XPS measurement. As a consequence, the conduction band is populated, leading to electron delocalization and high conductivity of the nanobundle. Based on the calculated band structure, these delocalized electrons are easily excited to available states above and leave the states unoccupied and thus available to electrons in valence band at ~1 eV below. The value is consistent with the measured thermal activation energy of the nanobundle and the mechanism explains the significant enhancement of electrical conductivity upon heating (increases 200 times from 23 ℃ to 200 ℃). Under focused laser illumination, the nanobundle displays significant photon induced current (9 nA) without external bias at low laser power (2

mW), the amplitude and polarity of photocurrent can be controlled by location of laser spot. The photon electrical response is due to the combined effect of photon excited electrons from nanobundle itself and from nanobundle-electrode junction.

The high electrical conductivity, the significant photon electrical response, the reduced metal ions and the deformed band structure, all these properties of WO_3 after K ion insertion are the same as K_xMoO_3. It suggests that these properties are induced by the inserted great amount of K ion in the structure. We envisage that by the same ion insertion method, great amount of K ions could be inserted and similar properties will be introduced to other ion intercalated metal oxide nanostructure. Besides the similarities, there are some differences between K_xMoO_3 and K_xWO_3, including the difference in growth orientation, lattice deformation and photo-electrical response. Further research on these differences will provide insight about ion insertion mechanism and ion insertion induced properties.

Chapter 7 Conclusion and Future Works

MoO_3 and WO_3 are widely studied for their broad applications in many industry fields, including photochromic devices, electrochromic devices, ion batteries, gas sensors and catalysts. The properties of these two materials are significantly improved by intercalation and nano-configuration separately. To further enhance the properties of materials, intercalation and nano-configuration should be combined together. Much effort has been spent on intercalating ions into nanostructure to achieve better properties. However, the existing methods have various limitations, such as structure deformation upon ion intercalation, multi-step process and ion size limitation. In this thesis, we developed a simple one step method to intercalate K ions into MoO_3 and WO_3 single crystalline nanostructure, and the layered structures of both materials were preserved with a great amount of large size ion insertion. Further, we studied the properties of both nano-materials after ion insertion. Excitingly, we found that these materials possessed many new properties, in particular, high conductivity, photoelectrical response and electromigration behaviour.

Ion insertion method

Thermal evaporation on mica substrate was used to grow K intercalated MoO_3 nanobundles. During the synthesis process, the continuous absorption of K^+ from mica substrate and MoO_3 vapour promoted the growth of K_xMoO_3 nanobundles. Our results suggest that the K atoms in the nanobundles most likely occupy the O vacancy sites. This structural arrangement allows the K atoms to be intercalated without incurring large distortion of the MoO_3 layered structure. The same method was applied to grow K ion intercalated WO_3 nanostructure. The single crystalline nanostructure

was successfully synthesized with the same growth mechanism. Although great amount of K ions was inserted, the pseudo-orthorhombic structure remained essentially intact. The success of applying the method in synthesizing two kinds of materials suggests the possibility to adopt the method to intercalate large ions into other metal oxides nanostructures without destroying the structures.

High Electrical Conductivity

With the use of a single nanobundle fabricated device, the electrical properties of the K_xMoO_3 nanobundles were measured. It was found that the electric conductivity of MoO_3 dramatically was enhanced 7 orders upon potassium uptake, and the conductivity was further increased 25 times as the temperature increased from 23 °C to 142 °C. Consequently, the current in an individual nanobundle could rise up to 0.15 mA at bias of 5 V. It is notable that the value is greatly significant compared with the current (in nA range) in other semiconductor nanomaterials under the same bias voltage. Similar high conductivity was observed in K intercalated WO_3 nanobundle. The nanobundles displayed a five fold increase in the electrical conductivity upon potassium intercalation. The electrical conductivity also increased by ~200 times as temperature increased from 23℃ to 200℃. The substantial high electric conductivity attributed to ion intercalation has not been observed in other reports. Theoretical calculation indicates that inserted K ions are fully ionized and transfer charges to Mo/W. It forces electrons to populate in the conduction band and leads to the high electrical conductivity of both materials. The increased high electrical conductivity after intercalation in both materials suggests that intercalating great amount of ions into the structure could significantly and efficiently modify the electrical properties of nanomaterials.

Photoelectrical Response

Pure MoO_3 and WO_3 did not display photo-electrical response due to their large band gap. After intercalation with K ions, photon induced voltage/ photon induced

current in individual K enriched MoO_3/WO_3 nanobundle was observed under irradiation of localized focused laser beam. Without external bias voltage, significant photon induced voltage (36.5 mV) /photon induced current (9 nA) was produced in single nanobundle under low laser power (2.2 mW). Remarkably, the amplitude and polarity of the voltage/current could be controlled by the location of focused laser spot. Unlike the common photon response that comes from metal-semiconductor junction or PN junction in hybrid nanomaterial, the observed photon induced effect is from nanobundle itself and attributed to small band gap of the material. The significant photoelectrical response in both two materials after intercalation suggests that intercalating ions into the structure could modify the band structure of the material and induce photoelectrical response property.

Electromigration Behavior

Due to the high current density, the momentum transferred from moving electrons is large enough to drive K ions. In addition to the high concentration of K ions, the preserved layered structure and low hopping barrier of ions, intercalated K ions could rapid and reversible migrate within a layered single crystalline K_xMoO_3 nanobundle. The duration required to induce significant accumulation of K ions and relaxation time of accumulated ions were significantly shorter than the value reported in other interstitial systems. The reversible ion movement was repeated for hundred times and remarkably there were no obvious sign of structural damage in the nanobundle. It is noted that, the electromigration is always observed in the metal and induces cracks or piles in the material, while our material is semiconductor and the morphology preserves after hundred rounds. The observation in our material opens a new direction for the study of electromigration effect and provides new insight about the mechanism of electromigration behaviour.

Future Works

Besides the well studied phenomenon described above, there are still some interesting performances of K_xMoO_3 nanobundle not systematically investigated, including electro-chromic effect, self-growth behaviour and superstructure.

Electro-chromism Effect

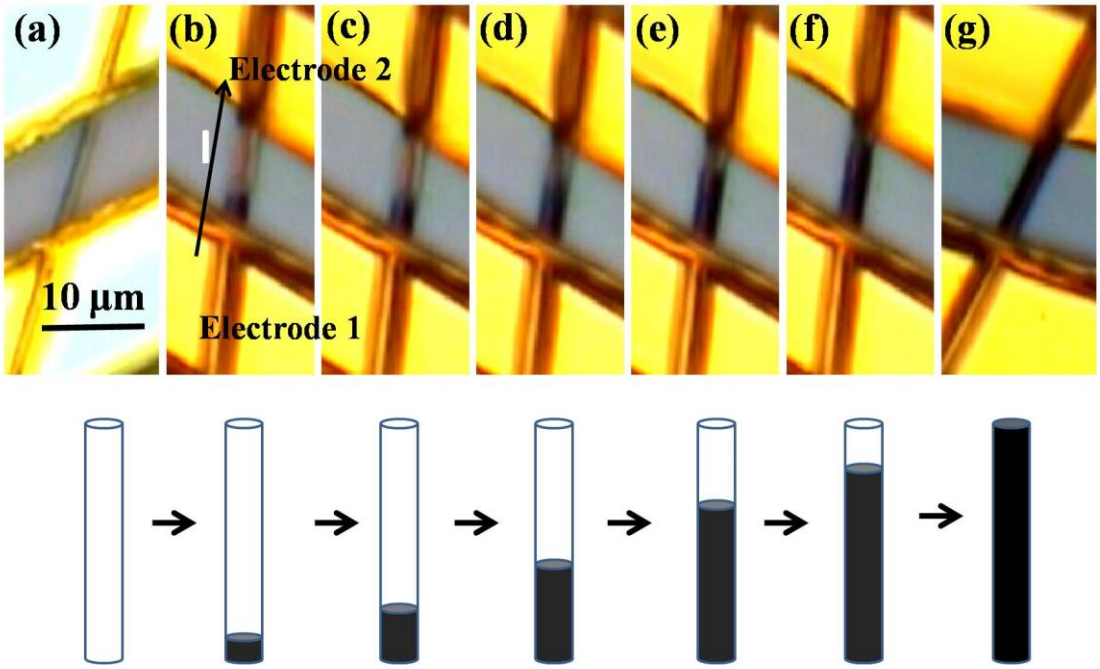

Figure 7.1 The optical image of nanobundle (a) before applied voltage (b) after applied voltage and current flow from electrode 1 to electrode 2 for ~1min (c) after applied current for ~3 min (d) ~5 min (e) ~7 min (f) ~9 min (g) ~10 min. The schematic image below each figure shows the color of K_xMoO_3 nanobundle at each step.

The K_xMoO_3 nanobundle is transparent under optical microscope. Through the nanobundle, we can observe the dark purple color of SiO_2 substrate as shown in Figure 7.1(a). As voltage of +5 V is applied between electrodes and current flows from electrode 1 to electrode 2 for ~1 min, part of nanobundle that near the electrode 1 turns to black, while the remaining part is still transparent (Figure 7.1(b)). As the time increases (Figure 7.1(c)~(f)), the black part gradually extends towards electrode 2 and finally the whole nanobundle turns into black (Figure 7.1(g)). The schematic images below each figures show the color of nanobundle at each step. It takes ~10

min for 10 μm long nanobundle to change from transparent (Figure 7.1(a)) to fully black (Figure 7.1(g)). The performance is similar to electrochromism effect, in which the color of MoO_3/WO_3 changes from transparent to blue upon ion and electron insertion. However, in our case, K ions are already inserted, and the appearance of electron flow results in the color change. The mechanism of such electrochromism effect is not understood yet.

Self-growth Behaviour

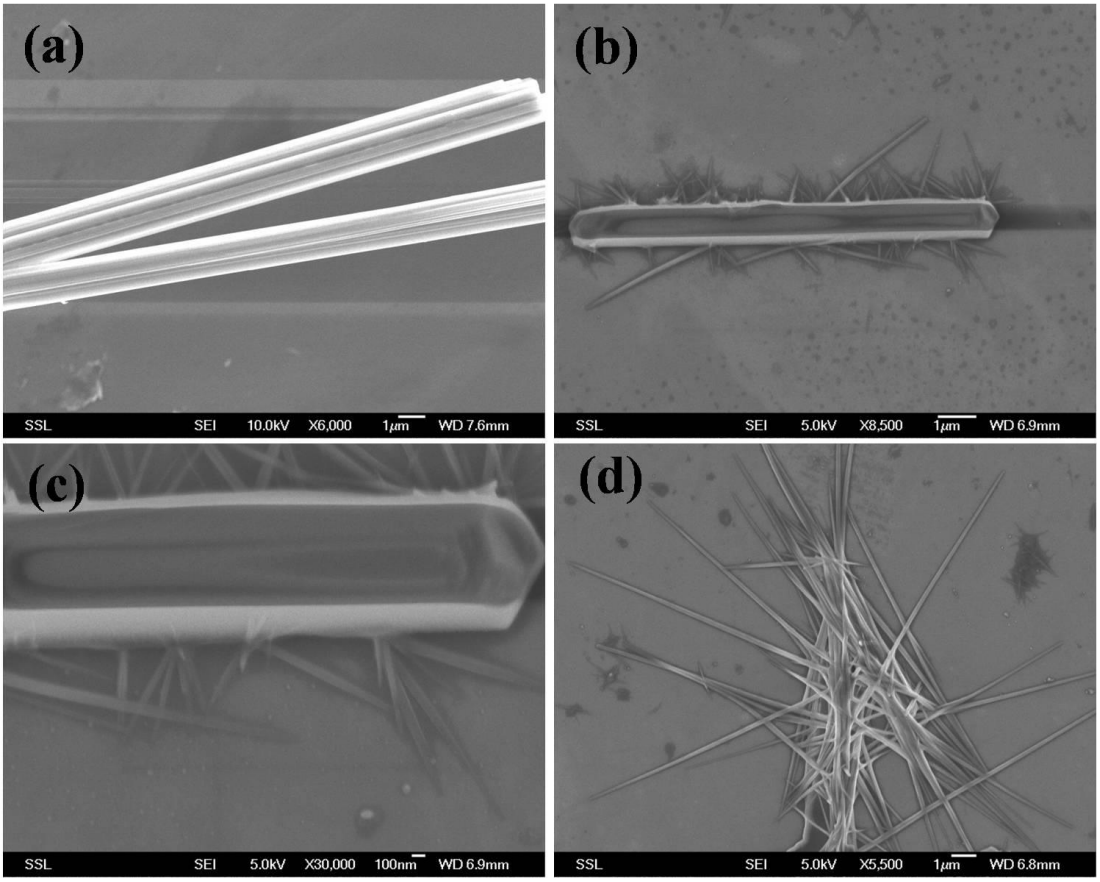

Figure 7.2 SEM image of individual K_xMoO_3 nanobundle (a) before annealing (b) after annealing at 450 ℃ for 20 min (c) zoom in image of the edge of nanobundle in (b). (d) The nanobundle fully transforms into new K_xMoO_3 nanostructures.

To investigate the thermal stability of K_xMoO_3 nanobundle, individual nanobundle is transferred to Si substrate and annealed under different temperature. When the nanobundle is annealed in ambient below 400 ℃ for 20 min, the morphology of nanobundle is preserved. When the temperature increases to 450 ℃,

the nanobundle is partly melted and new nanostructure forms around the nanobundle. When annealed at 500℃, the nanobundle is fully melted and transformed into liquid spot. The self-growth behavior is observed when nanobundle is heated at 450 ℃. Figure 7.2(a) displays the morphology of nanobundle before annealed. Clearly, the sharp edge and layered structure is observed. Figure 7.2(b) shows the nanobundle after annealing, the surface of nanobundle is partly melted, the edge becomes smooth and new nanostructure extends out from the nanobundle. These nanostructures grow from the melted surface and extend out in certain orientation. The nanostructure possess nanobelt configuration, the top of these nanostructures gradually shrink and all structures show same width as shown in Figure 7.2(c). Some K_xMoO_3 nanobundles are fully transformed into these new nanostructures as shown in Figure 7.2(d). The Raman spectrum of the self-grow nanostructures is exactly the same as K_xMoO_3 nanobundle, denoting the same lattice structure and component as K_xMoO_3 nanobundle. According to the proposed growth mechanism of K_xMoO_3 nanobundle, K_xMoO_3 nanobundle extends out due to the over saturation of K_xMoO_3 liquid. Similarly, the over saturation of K_xMoO_3 liquid on the partly melted surface of nanobundle promotes the self-growth of new K_xMoO_3 nanostructure. The details of growth mechanism are not fully understood, such as the mechanism of same width of all new nanobelts, the difference between old K_xMoO_3 nanobundle and new K_xMoO_3 nanostructure, etc.. Future works need to be carried out.

Superstructure

Although the lattice structure of MoO_3 and WO_3 is preserved, super structure is observed after K ion insertion. Figure 7.3(a) shows the diffraction pattern of individual K_xMoO_3 nanobundle on (010) surface. As described in Chapter 3, the yellow rectangle constructed by four bright spots denotes the orthorhombic lattice structure of MoO_3. Along [100] direction, there are always 5 small spots evenly distributed between two bright spots, as shown by the white arrows in Figure 7.3(a). It suggests the super structure along [100] direction in every 6 units. The super structure

is observed in all nanobundles, regardless the variation of K ion concentration (atomic percentage ratio of K over Mo ranges from 20% to 25%) in different nanobundles. Similar phenomenon is observed in K_xWO_3 nanobundle. Figure 7.3(b) shows the diffraction pattern of individual K_xWO_3 nanobundle on (010) surface. The blue rectangle constructed by bright spots denotes the pseudo-orthorhombic lattice structure of WO_3. Along [100] direction, one small spot appears in the middle of every two bright spots, as shown by the white arrows in Figure 7.3(b). It suggests the super structure along [100] direction in every 2 units. The super structure is observed in all nanobundles, regardless the variation of K ion concentration in different nanobundles. In both K_xMoO_3 nanobundle and K_xWO_3 nanobundle, the superstructure appears in the direction perpendicular to the growth direction. The mechanism of super structure is not clearly understood. It is possibly due to the periodic alignment of K ions in the structure. Further study on it will reveal brand new method to create super structures and get deeper insight about structure dynamics.

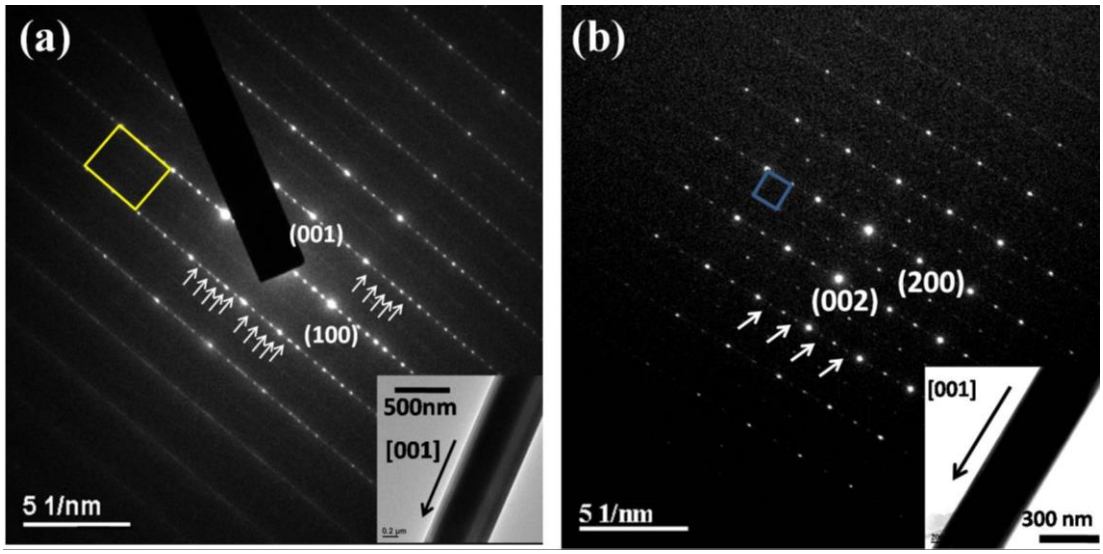

Figure 7.3 (a) Electron diffraction pattern of K_xMoO_3 nanobundle on (010) surface, the yellow rectangle constructed by large bright spots represents lattice structure of K intercalated MoO_3, inset image shows TEM image of typical K_xMoO_3 nanobundle growing in [001] direction, white arrows highlight the superstructure. (b) Electron diffraction pattern of the K_xWO_3 nanobundle on (010) surface, the blue rectangle formed by large bright spots represents the lattice structure of the K intercalated WO_3. The inset image shows a TEM image of the typical K_xWO_3 nanobundle growing in the [001] direction. White arrows highlight the superstructure.

In addition to these interesting properties of individual nanostructure, the properties in other applications, where large amount of nanobundles are required, should be systematically studied as well, such as the application in Li ion battery. However, the amount of nanobundles is not large enough by the current method and the mica substrate is not conductive. Future work should be carried out in enhancing the productivity of nanobundles and transferring them to conductive substrate. One possible way to increase productivity is creating steps on mica substrate by micro-etching method. Considering the wonderful properties of individual nanobundle, it is reasonable to expect good performance of K enriched MoO_3 or WO_3 in these applications.

In K_xMoO_3 and K_xWO_3, the x ranges from 0.2 to 0.25. As we know, the properties of material will changes as the amount of intercalated ions varies. We can assume that as x increases from 0.2 to 0.25, the properties such as conductivity, photo-electrical response should changes accordingly. However, after the nanobundle is made into device, the precise atomic percentage of K could not be detected by TEM. The silicon substrate is too thick for electron transmission in TEM. Further effort should made to systematically explore the properties of nanobundle under different K concentration.

Although the chemistry stoichiometry of K_xMoO_3 nanostructure is similar with potassium molybdenum bronze ($K_{0.3}MoO_3$), the structure of $K_{0.3}MoO_3$ is quite different with the K_xMoO_3 nanobundle (as discussed in Chapter 1). Since the different structures lead to varied properties, the extensive studies about the $K_{0.3}MoO_3$ are not discussed in the thesis. However, there are some similarities between these two materials, such as layered structure (although in different orientations), similar amount of K ions being intercalated, it should be quite useful to carry out further research about K_xMoO_3 nanobundle in the field where $K_{0.3}MoO_3$ are extensively studied by

physicists, particularly in areas focusing on charge density waves. The comparison between these two materials in those fields possibly provides further insight.

Besides the further study about the properties of K_xMoO_3 nanobundle and K_xWO_3 nanobundle, our simple, one-step synthesis method can be modified to develop various ion intercalated nanostructures. Firstly, besides the muscovite mica $KAl_2(AlSi_3O_{10})(F,OH)_2$ we use, there are many other kinds of mica with different components and ion concentration, such as Lepidolite ($KLi_2Al(Al,Si)_3O_{10}(F,OH)_2$. It possibly introduces the insertion of different ions when different kinds of mica substrate is utilized during synthesis. Secondly, we can try to intercalate K ions into other layered nanomaterials by similar method, such as MoS_2 nanostructure. The ion intercalation in these materials would modify the band structures and electric properties of the materials, and finally introduce many new applications.

Bibliography

[1] C. N. R. Rao, *Annu. Rev. Phys. Chem.* **40**, 291-326 (1989).

[2] Tao He, Jiannian Yao, *Journal of Photochemistry and Photobiology C: Photochemistry Reviews* **4**, 125–143 (2003).

[3] C. G. Granqvist, *Solar Energy Materials & Solar Cells* **60**, 201-262 (2000).

[4] J. M. Tarascon, M. Armand, *Nature* **414**, 359-367 (2001).

[5] G. Eranna, B. C. Joshi, D. P. Runthala and R. P. Gupta, *Critical Reviews in Solid State and Materials Sciences* **29**, 111-188 (2004).

[6] Gerhard Mestl, *Topics in Catalysis* **38**, 69-82 (2006).

[7] http://en.wikipedia.org/wiki/Periodic_table.

[8] Ekhard Salje, *Acta Cryst. B* **33**, 574-577 (1977).

[9] J. Scarminio, A. Lourenco, A. Gorenstein, *Thin Solid Films* **302**, 66-70 (1997).

[10] K. Ajito, L. A. Nagahara, D. A. Tryk, K. Hashimoto and A. Fujishima, *J. Phys. Chem.* **99**, 16383-16388 (1995).

[11] Se-Hee Lee, Hyeonsik M. Cheong, Ji-Guang Zhang, Angelo Mascarenhas, David K. Benson, and Satyen K. Deb, *Appl. Phys. Lett.* **74**, 242-244 (1999).

[12] David R. Rosseinsky, Roger J. Mortimer, *Adv. Mater.* **13**, 783-793 (2001).

[13] Gunnar A. Niklasson, C. G. Granqvist, *J. Mater. Chem.* **17**, 127-156 (2007).

[14] G.M. Sottile, *Materials Science and Engineering B* **119**, 240-245 (2005).

[15] Su-Lan Kuai, Georges Bader, and P. V. Ashrit, *Appl. Phys. Lett.* **86**, 221110 (2005).

[16] Norihisa Kobayashi, Mami Nishimura, Hirosada Ohtomo, *Electrochimica Acta* **50**, 3886-3890 (2005).

[17] http://electronics.howstuffworks.com/everyday-tech/lithium-ion-battery1.htm.

[18] Natasha A. Chernova, Megan Roppolo, Anne C. Dillon and M. Stanley Whittingham, *J. Mater. Chem.* **19**, 2526-2552 (2009).

[19] Maosong Tong, Guorui Dai, Yuanda Wu, Xiuli He and Dingsan Gao, *Journal of Materials Science* **36**, 2535-2538 (2001).

[20] A.K. Prasad, D.J. Kubinski, P.I. Gouma, *Sensors and Actuators B* **93**, 25-30 (2003).

[21] D. Mutschall, K. Holzner, E. Obermeier, *Sensors and Actuators B* **35-36**, 320-324 (1996).

[22] M. Chen, C. M. Friend and Efthimios Kaxiras, *J. Am. Chem. Soc.* **123**, 2224-2230 (2001).

[23] J. N. Yao, K. Hashimoto and A. Fujishima, *Nature* **355**, 624-626 (1992).

[24] Yuzhi Zhang, Sulan Kuai, Zhongchun Wang and Xingfang Hu, *Applied Surface Science* **165**, 56-59 (2000).

[25] F. Leroux, G. R. Goward, W. P. Power and L. F. Nazar, *Electrochem. Solid-State Lett.* **1**, 255-258 (1998).

[26] M. Dhanasankar, K.K. Purushothaman, G. Muralidharan, *Materials Research Bulletin* **45**, 1969-1972 (2010).

[27] Hideyuki Tagaya, Kensuke Ara, Jun-ichi Kadokawa, Masa Karasu and Koji Chiba, *J. Mater. Chem.* **4**, 551-555 (1994).
[28] M. E. Spahr, P. Novák, O. Haas, R. Nesper, *Journal of Power Sources* **54**, 346-351 (1995).
[29] Tarsame S. Sian and G. B. Reddyz, *J. Electrochem. Soc.* **152**, A2323-A2326 (2005).
[30] Yuzhi Zhang, Jiaguo Yuan, Yunzhen Cao, Lixin Song, Xingfang Hu, *Journal of Non-crystalline solids* **354**, 1276-1280 (2008).
[31] S.S. Mahajan, S.H. Mujawar, P.S. Shinde, A.I. Inamdar, P.S. Patil, *Applied Surface Science* **254**, 5895–5898 (2008).
[32] A.C. Dillon, A.H. Mahan, R. Deshpande, P.A. Parilla, K.M. Jones, S-H. Lee, *Thin Solid Films* **516**, 794-797 (2008).
[33] Se-Hee Lee, Rohit Deshpande, Phil A. Parilla, Kim M. Jones, Bobby To, A. Harv Mahan, and Anne C. Dillon, *Adv. Mater.* **18**, 763-766 (2006).
[34] J. Maier, *Nat. Mater.* **4**, 805-815 (2005).
[35] Praveen Meduri, Ezra Clark, Jeong H. Kim, Ethirajulu Dayalan, Gamini U. Sumanasekera and Mahendra K. Sunkara, *Nano Lett.* **12**, 1784-1788 (2012).
[36] Liang Zhou, Lichun Yang, Pei Yuan, Jin Zou, Yuping Wu and Chengzhong Yu, *J. Phys. Chem. C* **114**, 21868-21872 (2010).
[37] Andrew N. Shipway, Eugenii Katz, and Itamar Willner, *Chem. Phys. Chem.* **1**, 18-52 (2000).
[38] E. Comini, L. Yubao, Y. Brando, G. Sberveglieri, *Chemical Physics Letters* **407**, 368-371 (2005).
[39] W.G. Chu, L.N. Zhang, H.F. Wang,Z.H. Han,D. Han,Q.Q. Li,S.S. Fan, *J. Mater. Res.* **22**, 1609-1617 (2007).
[40] Y. L. Xie, F. C. Cheong, Y. W. Zhu, B. Varghese, Rajesh Tamang, A. A. Bettiol, and C. H. Sow, *J. Phys. Chem. C* **114**, (2010).
[41] Tarsame S. Sian, G. B. Reddyz, *J. Electrochem. Soc.* **152**, A2323-A2326 (2005).
[42] Joseph W. Bullard III, Richard L. Smith, *Solid State Ionics* **160**, 335– 349 (2003).
[43] Liqiang Mai, Bin Hu, Wen Chen, Yanyuan Qi, Changshi Lao, Rusen Yang, Ying Dai and Zhong Lin Wang, *Adv. Mater.* **19**, 3712-3716 (2007).
[44] Zhe Zheng, Bin Yan, Jixuan Zhang, Yumeng You, Chwee Teck Lim, Zexiang Shen, and Ting Yu, *Adv. Mater.* **20**, 352-356 (2008).
[45] http://en.wikipedia.org/wiki/Scanning_electron_microscope.
[46] http://en.wikipedia.org/wiki/SAED.
[47] http://en.wikipedia.org/wiki/Energy-dispersive_X-ray_spectroscopy.
[48] http://en.wikipedia.org/wiki/X-ray_photoelectron_spectroscopy.
[49] Pascale Delporte, Frédéric Meunier, Cuong Pham-Huu, Philippe Vennegues, and Marc J. Ledoux, Jean Guille, *Catalyst Today* **23**, 251-267 (1995).
[50] M. Anwar, C. A. Hogarth and R. Bulpett, *Journal of Materials Science* **24**, 3087-3090 (1989).
[51] 2002 JCPDS (Card No. 89-5108) International Centre for Diffraction Data.
[52] N.D. Chatterjee and W. Johannes, *Contrib. Mineral. Petrol.* **48**, 89-114 (1974).

[53] M. A. PY, PH. E. Schimid and J. T. Vallin, *Il Nuovo Cimento B* **38** 271-279 (1977).
[54] Rudy Coquet and David J. Willock, *Phys. Chem. Chem. Phys.* **7**, 3819-3828 (2005).
[55] C.V. S. Reddy, Z. R. Deng, Q. Y. Zhu, Y. Dai, J. Zhou, W. Chen, S.-I. Mho, *Apply Phys. A* **89**, 995-999 (2007).
[56] Israel E. Wachs, *Catalysis Today* **27**, 437-455 (1996).
[57] Hendrik Heinz, Hein J. Castelijns and Ulrich W. Suter, *J. Am. Chem. Soc.* **125**, 9500-9510 (2003).
[58] George L. Gaines Jr., *J. Phys. Chem.* **61**, 1408–1413 (1957).
[59] J. H. Chute, J. P. Quirk, *Nature* **18**, 1156-1157 (1967).
[60] T. M. Barbara, G. Gammie, J. W. Lyding, and J. Jonas, *Journal of Solid State Chemistry* **75**, 183-187 (1988).
[61] A. M. Hashem, M. H. Askar, M. Winter, J. H. Albering and J. O. Besenhard, *Ionics* **13**, 3-8 (2007).
[62] S. M. Sze, and K. K. Ng, *"Physics of Semiconductor De-vice," 3rd Edition, Wiley, New York,pp. 21-25.* (2007).
[63] Kien-Wen Sun, Ting-Yuan Fan, *Materials Sciences and Applications* **1**, 8-12 (2010).
[64] Josh Goldberger, Donald J. Sirbuly, Matt Law, and Peidong Yang, *J. Phys. Chem. B* **109**, 9-14 (2005).
[65] Xianwei Sha, Liang Chen, Alan C. Cooper, Guido P. Pez, and Hansong Cheng, *J. Phys. Chem. C* **113**, 11399–11407 (2009).
[66] Graeme Henkelman, Andri Arnaldsson, Hannes Jo´nsson, *Computational Materials Science* **36**, 354-360 (2006).
[67] Yat Li, Fang Qian, Jie Xiang, and Charles M. Lieber, *Mater. Today* **9**, 18-27 (2006).
[68] Wei Lu and Charles M. Lieber, *Nature Mater.* **6**, 841-850 (2007).
[69] Matt Law, Lorie. Greene, Justin C. Johnson, Richard Saykally and Peidong Yang, *nature materials* **4**, 455-459 (2005).
[70] Bozhi Tian, Thomas J. Kempa and Charles M. Lieber, *Chem. Soc. Rev.* **38**, 16-24 (2008).
[71] Q. H. Li, Y. X. Liang, Q. Wan, and T. H. Wang, *Appl. Phys. Lett.* **26**, 6389-6391 (2004).
[72] ZhiMin Liao, Jun Xu, JingMin Zhang, and DaPeng Yu, *Appl. Phys. Lett.* **93**, 023111 (2008).
[73] C. Colombo, M. Hei, M. Grätzel, and A. Fontcuberta i Morral, *Appl. Phys. Lett.* **94**, 173108 (2009).
[74] Bozhi Tian, Xiaolin Zheng, Thomas J. Kempa, Ying Fang, Nanfang Yu, Guihua Yu, Jinlin Huang & Charles M. Lieber, *Nature* **449**, 885-890 (2007).
[75] Michael D. Kelzenberg, Daniel B. Turner-Evans, Brendan M. Kayes, Michael A. Filler, Morgan C. Putnam, Nathan S. Lewis, and Harry A. Atwater, *Nano Lett.* **8**, 710-714 (2008).

[76] Y. Gu, E.-S. Kwak, J. L. Lensch, J. E. Allen, T. W. Odom, L. J. Lauhon, *Appl. Phys. Lett.* **87**, 043111 (2005).
[77] Binni Varghese, Rajesh Tamang, Eng Soon Tok, Subodh G. Mhaisalkar and Chorng Haur Sow *J. Phys. Chem. C* **114**, 15149-15156 (2010).
[78] Rajesh Tamang, Binni Varghese, Subodh G Mhaisalkar, Eng Soon Tok and Chorng Haur Sow, *Nanotechnology* **22**, 115202 (2011).
[79] Jiwoong Park, Y. H. Ahn, Carlos Ruiz-Yargas, *Nano Lett.* **9**, 1742-1746 (2009).
[80] Y. H. Ahn, A. W. Tsen, Bio Kim, Yung Woo Park, and Jiwoong Park, *Nano Lett.* **7**, 3320-3323 (2007).
[81] Binni Varghese, Bablu Mukherjee, K. R. G. Karthik, K. B. Jinesh, S. G. Mhaisalkar, Eng Soon Tok, and Chorng Haur Sow, *J. Appl. Phys.* **111**, 104306 (2012).
[82] Thomas J. Kempa, Bozhi Tian, Dong Rip Kim, Jinsong Hu, Xiaolin Zheng, and Charles M. Lieber, *Nano Lett.* **8**, 3456-3460 (2008).
[83] Sarah R. Cowan, R. A. Street, Shinuk Cho, and A. J. Heeger, *Phys. Rev. B* **83**, 035205 (2011).
[84] K. Wang, J. J. Chen, Z. M. Zeng, J. Tarr, W. L. Zhou, Y. Zhang, Y. F. Yan, C. S. Jiang, J. Pern, and A. Mascarenhas, *Appl. Phys. Lett.* **96**, 123105 (2010).
[85] D. G. Pierce and P. G. Brusius, *Microelectron. Reliab.* **37**, 1053-1072 (1997).
[86] Richard S. Sorbello, *Solid State Physics* **51**, 159-231 (1997).
[87] Paul S Ho and Thomas Kwok, *Rep. Prog. Phys.* **52**, 301-348 (1989).
[88] J van Ek and A Lodder, *J. Phys.: Condens. Matter* **3**, 7331-7361 (1991).
[89] J van Ek and A Lodder, *J. Phys.: Condens. Matter* **3**, 8403-8416 (1991).
[90] J. R. Lloyd, *Semicond. Sci. Technol.* **12**, 1177-1185 (1997).
[91] B. C. Regan, S. Aloni, R. O. Ritchie, U. Dahmen & A. Zettl, *Nature* **428**, 924-927 (2004).
[92] M. A. Haase, J. M. DePuydt, H. Cheng, and J. E. Potts, *Appl. Phys. Lett.* **58**, 1173-1174 (1991).
[93] J. R. Lloyd, M. R. Polcari, G. A. Mackenzie, *Appl. Phys. Lett.* **36**, 428-430 (1980).
[94] H. Ohtsuka, Y. Sakurai, *Solid State Ionics* **144**, 59–64 (2001).
[95] José-Luis Mozos, Pablo Ordejón, and Enric Canadell, *Physical Review B* **65**, 233105 (2002).
[96] L. M. S. Alves, V. I. Damasceno, C. A. M. dos Santos, A. D. Bortolozo, P. A. Suzuki, H. J. Izario Filho, A. J. S. Machado, and Z. Fisk, *Physical Review B* **81**, 174532 (2010).
[97] J. Graham, A. D. Wadsley *Acta Cryst.* **20**, 93-100 (1966).
[98] J. Garcia-Barriocanal, A. Rivera-Calzada, M. Varela, Z. Sefrioui, E. Iborra, C. Leon, S. J. Pennycook, J. Santamaria, *Science* **321**, 676-680 (2008).
[99] Tatsumi Ishihara, Hideaki Matsuda, and Yusaku Takita, *J. Am. Chem. Soc.* **116**, 3801-3803 (1994).
[100] H. Nakajima, M. Yoshioka and M. Koiwa, *Acta mtall.* **35**, 2731-2736 (1987).
[101] R. C. Brouwer and R. Griessen, *Phys. Rev. Lett.* **62**, 1760-1763 (1989).
[102] A. Priemuth, *physica status solidi (a)* **67**, 505-510 (1981).

[103] I. A. Blech and E. S. Meieran, *J. Appl. Phys.* **40**, 485-491 (1969).
[104] M. W. Lane, E. G. Liniger and J. R. Lloyd, *J. Appl. Phys.* **93**, 1417-1421 (2003).
[105] J. R. Lloyd, J. J. Clementi, *Thin Solid Films* **262**, 135-141 (1995).
[106] B. Stahlmecke, a F.-J. Meyer zu Heringdorf, L. I. Chelaru, M. Horn-von Hoegen, and G. Dumpich, *Appl. Phys. Lett.* **88**, 053122 (2006).
[107] Anders Hjelm and Claes G. Granqvist, John M. Wills, *Physical Review B* **54**, 2436-2445 (1996).
[108] Anandan Srinivasan, Masahiro Miyauchi, *J. Phys. Chem. C* **116**, 15421-15426 (2012).
[109] Fumiaki Amano, Min Tian, Guosheng Wu, Bunsho Ohtani, and Aicheng Chen, *ACS Appl. Mater. Interfaces* **3**, 4047-4052 (2011).
[110] i. karakurt, j. boneberg, p. leiderer, *Applied Physics/ A, Materials science and processing* **83**, 1-3 (2006).
[111] Cláudia Costa, Carlos Pinheiro, Inês Henriques, and César A. T. Laia, *ACS Appl. Mater. Interfaces* **4**, 1330-1340 (2012).
[112] Songhun Yoon, Changshin Jo, Soon Young Noh, Chul Wee Lee, Jun Ho Song and Jinwoo Lee, *Phys. Chem. Chem. Phys.* **13**, 11060-11066 (2011).
[113] Tao He, Ying Ma, Ya-an Cao, Wen-sheng Yang and Jian-nian Yao, *Phys. Chem. Chem. Phys.* **4**, 1637-1639 (2002).
[114] K. Aguir, C. Lemire, D.B.B. Lollman, *Sensors and Actuators B* **84**, 1-5 (2002).
[115] Zhihui Jiao, Jinmin Wang, Lin Ke, Xiao Wei Sun, and Hilmi Volkan Demir, *ACS Appl. Mater. Interfaces* **3**, 229-236 (2011).
[116] Xiaoyu Chen, Yong Zhou, Qi Liu, Zhengdao Li, Jianguo Liu, and Zhigang Zou, *ACS Appl. Mater. Interfaces* **4**, 3372-3377 (2012).
[117] Q. Zhong, J. R. Dahn and K. Colbow, *Physical Review B* **46**, 2554-2560 (1992).
[118] Maria Strømme Mattsson, *Physical Review B* **58**, 11015-11022 (1998).
[119] G. L. Frey, A. Rothschild, J. Sloan, R. Rosentsveig, R. Popovitz-Biro and R. Tenne, *Journal of Solid State Chemistry* **162**, 300-314 (2001).
[120] A Polaczek, M Pekata and Z Obuszko, *J. Phys.: condens. Matter* **6**, 7909-7919 (1994).
[121] Maja Remškar, Janez Kovac, Marko Viršek, Maja Mrak, Adolf Jesih, and Alan Seabaugh, *Adv. Funct. Mater.* **17**, 1974-1978 (2007).
[122] Fook Chiong Cheong, Binni Varghese, Yanwu Zhu, Eunice Phay Shing Tan, Ling Dai, Vincent B. C. Tan, Chwee Teck Lim, and Chorng Haur Sow, *J. Phys. Chem. C* **111**, 17193-17199 (2007).
[123] http://en.wikipedia.org/wiki/WO3.
[124] http://en.wikipedia.org/wiki/MoO3.
[125] 2002 JCPDS (Card No. 84-1304) International Centre for Diffraction Data.
[126] 2002 JCPDS (Card No. 89-4480) International Centre for Diffraction Data.
[127] Jian Chen, Dongyu Lu, Weihong Zhang, Fangyan Xie, Jun Zhou, Li Gong, Xiao Liu, Shaozhi Deng and Ningsheng Xu, *J. Phys. D: Appl. Phys.* **41**, 115305 (2008).

[128] M. Gilleta, K. Aguir, C. Lemire, E. Gillet, K. Schierbaum, *Thin Solid Films* **467**, 239-246 (2004).
[129] G. A. de Wijs, P. K. de Boer, and R. A. de Groot, *Physical Review B* **59**, 2684-2693 (1999).